Summer 8-13-2010

Quantitative Molecular MRI of Intervertebral Disc Degeneration

Chenyang Wang
University of Pennsylvania, wangch@seas.upenn.edu

Quantitative Molecular MRI of Intervertebral Disc Degeneration

Abstract
Degeneration of the intervertebral disc (IVD) is the most common cause of back-related disability among North American adults. Low-back-pain and associated disability costs the United States more than 100 billion dollars annually in health care expenditures and reduced productivity. The mechanism of IVD degeneration, especially its biomolecular aspect, is poorly understood in an in vivo setting. Thus there is increasingly a need for the non-invasive diagnosis and quantification of IVD degeneration. MRI is a non-invasive imaging modality capable of producing contrast sensitive to biomolecules. Therefore, the primary objective of this dissertation research project is to develop MRI techniques capable of non-invasive quantification of IVD biomolecular composition in vivo. We further developed three MRI techniques specifically for IVD imaging. Magnetization transfer (MT) MRI, T1ρ MRI and sodium MRI were first separately validated of their specificities for IVD biomolecular components. In doing so, we concluded that MT MRI is sensitive to IVD collagen content, T1ρ MRI is indicative of IVD osmotic pressure, and sodium MRI is sensitive to IVD proteoglycan (PG) content. Next, we applied all three techniques to human subjects in vivo. Due to the inherently low signal-to-noise ratio (SNR) efficiency of sodium MRI, we engineered a custom radio-frequency (RF) surface coil for sodium MRI of human lumbar spine on a 7 T MRI scanner. Cross-correlation of the MT MRI, T1ρ MRI and sodium MRI data with the corresponding Pfirrmann grade revealed that the relative collagen density of IVD increases with degeneration, the IVD osmotic pressure decreases with degeneration, and the IVD PG content decreases with degeneration. By establishing that in vivo MT MRI, T1ρ MRI and sodium MRI can be used to quantify multiple IVD biomolecular characteristics non-invasively, we open up the possibility to conduct longitudinal studies on human subjects as they undergo IVD degeneration. The combination of MT MRI, T1ρ MRI and sodium MRI provides scientists and clinicians with the diagnostic tool to improve our understanding of IVD degeneration, which could benefit future treatment and prognosis of IVD degeneration.

Degree Type
Dissertation

Degree Name
Doctor of Philosophy (PhD)

Graduate Group
Bioengineering

First Advisor
Ravinder Reddy

Keywords
INTERVERTEBRAL DISC, MRI, PROTEOGLYCAN, COLLAGEN, OSMOTIC PRESSURE, DEGENERATION

Subject Categories
Bioimaging and Biomedical Optics

QUANTITATIVE MOLECULAR MRI OF INTERVERTEBRAL DISC DEGENERATION

CHENYANG WANG

A DISSERTATION

IN

BIOENGINEERING

Presented to the Faculties of the University of Pennsylvania in Partial Fulfillment of the Requirements for the Degree of Doctor of Philosophy

2010

Supervisor of Dissertation	Graduate Group Chairperson
*Signature*_____	*Signature*_____
Ravinder Reddy, PhD	Susan S. Margulies, PhD
Professor of Radiology	Professor of Bioengineering

Dissertation Committee

Andrew Tsourkas, PhD, Associate Professor of Bioengineering

Beth A. Winkelstein, PhD, Associate Professor of Bioengineering

Felix W. Wehrli, PhD, Professor of Radiology

Quantitative Molecular MRI of Intervertebral

Disc Degeneration

Dedicated to my parents for their support in my pursuit for education,

and to the many others who have believed in me

ACKNOWLEDGEMENTS

I would like to thank my PhD advisor - Professor Ravinder Reddy for his unwavering intellectual support for the past five years. He genuinely believed in my potential from day one, and he has played an instrumental part in helping me to discover my interests in scientific research and in medicine. I owe a big thank you to Ari Borthakur and Mark Elliott for their mentorship at work and outside of work, but more importantly I am indebted to them for their friendship. I want to thank my then fellow graduate student - Walter Witschey for showing me the virtue of a strong work ethic. I cannot thank Susan Colleluori enough for helping me to navigate the maze of academic bureaucracy and also for introducing me to Philadelphia's unique cultural scene. I would like to offer my sincere gratitude to my dissertation committee of Professor Andrew Tsourkas, Professor Felix Wehrli and Professor Beth Winkelstein. Their invaluable guidance over the course of my dissertation project was crucial in ensuring both its quality as well as its timely completion. At last, I would like to thank my parents for giving me the opportunities to pursue my education and my career in science. I could not have gotten this far without them.

ABSTRACT

QUANTITATIVE MOLECULAR MRI OF INTERVERTEBRAL DISC DEGENERATION

CHENYANG WANG

Supervisor: Ravinder Reddy

Degeneration of the intervertebral disc (IVD) is the most common cause of back-related disability among North American adults. Low-back-pain and associated disability costs the United States more than 100 billion dollars annually in health care expenditures and reduced productivity. The mechanism of IVD degeneration, especially its biomolecular aspect, is poorly understood in an *in vivo* setting. Thus there is increasingly a need for the non-invasive diagnosis and quantification of IVD degeneration. MRI is a non-invasive imaging modality capable of producing contrast sensitive to biomolecules. Therefore, the primary objective of this dissertation research project is to develop MRI techniques capable of non-invasive quantification of IVD biomolecular composition *in vivo*. We further developed three MRI techniques specifically for IVD imaging. Magnetization transfer (MT) MRI, $T_{1\rho}$ MRI and sodium MRI were first separately validated of their specificities for IVD biomolecular components. In doing so, we concluded that MT MRI is sensitive to IVD

collagen content, $T_{1\rho}$ MRI is indicative of IVD osmotic pressure, and sodium MRI is sensitive to IVD proteoglycan (PG) content. Next, we applied all three techniques to human subjects *in vivo*. Due to the inherently low signal-to-noise ratio (SNR) efficiency of sodium MRI, we engineered a custom radio-frequency (RF) surface coil for sodium MRI of human lumbar spine on a 7 T MRI scanner. Cross-correlation of the MT MRI, $T_{1\rho}$ MRI and sodium MRI data with the corresponding Pfirrmann grade revealed that the relative collagen density of IVD increases with degeneration, the IVD osmotic pressure decreases with degeneration, and the IVD PG content decreases with degeneration. By establishing that *in vivo* MT MRI, $T_{1\rho}$ MRI and sodium MRI can be used to quantify multiple IVD biomolecular characteristics non-invasively, we open up the possibility to conduct longitudinal studies on human subjects as they undergo IVD degeneration. The combination of MT MRI, $T_{1\rho}$ MRI and sodium MRI provides scientists and clinicians with the diagnostic tool to improve our understanding of IVD degeneration, which could benefit future treatment and prognosis of IVD degeneration.

TABLE OF CONTENTS

LIST OF TABLES

LIST OF ILLUSTRATIONS

Chapter 1: Introduction to Magnetic Resonance Imaging of the Intervertebral Discs

1.1 Synopsis

The first chapter provides background information on intervertebral disc (IVD) physiology and pathophysiology as well as the basis of MT MRI, $T_{1\rho}$ MRI and sodium MRI. This chapter also reviews the current state of the above-mentioned MRI techniques pertaining to IVD imaging, with discussion on the limitations of previous studies.

1.2 Physiology of Intervertebral Disc

1.2.1 Intervertebral Disc in Spinal Column

The IVD lies between vertebral bodies in the spinal column, acting as a mechanical linkage and anchoring adjacent vertebral bodies (Figure 1-1). There are two distinct regions within a healthy IVD: a gelatinous inner region called the nucleus pulposus (NP) and a firm annulus fibrosus (AF) organized in multiple lamellae(Beadle 1931). Between the IVD and adjacent vertebral body is a layer of cartilage called the cartilage endplate. In younger individuals, the cartilage endplate is thick and takes up most of the IVD space(Coventry 1945), and it

decreases to 1~2 mm in thickness by adolescence(Roberts, Menage and Urban 1989). The IVD is secured to the cartilage endplate by collagen fibers. Some of the outermost AF lamellae fibers in the anterior and posterior directions go over the edges of the vertebral bodies and connect directly to the bony tissues, and other AF fibers merge vertically with the longitudinal ligaments parallel with the spinal column(Coventry 1945, Beadle 1931).

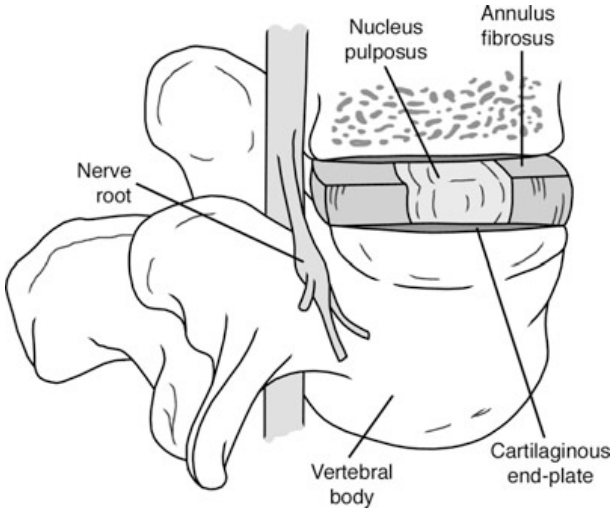

Figure 1-1. A graphical depiction of the IVD within a motion segment of the spine, showing both the NP and AF between the cartilaginous endplates of the vertebral bodies(Raj 2008).

There are 33 vertebrae in human spinal column, which includes seven cervical, 12 thoracic, five lumbar, a sacrum of five fused vertebras, and a coccyx of four fused vertebral bodies(De Palma and Rothman 1970). IVDs are located between two adjacent un-fused vertebral bodies, with the exception of the first and second cervical vertebral bodies(De Palma and Rothman 1970). IVD functions by transmitting loads through the spinal column, and by providing the spinal column with flexibility for motion. It has

been shown that cervical IVDs have wide range of motion, which includes 127 degrees for flexion and extension, 73 degrees total inclination and 142 degrees total rotation(Ferlic 1962). In contrast, the small size of thoracic IVDs along with their connections to the sternum and rib cage limit their motion(De Palma and Rothman 1970). In lumbar IVDs, flexion and extension are permitted for up to 92 degrees between the last lumbar vertebral body and the first sacral vertebral body(Clayson et al. 1962). Therefore, changes in the properties of IVD affect the mechanical functioning of the entire spinal column.

Human IVDs vary in size along the spine, with the lumbar IVDs being the largest. In total, IVDs account for approximately 25 percent of the length of the spinal column(Coventry 1945). In the cervical region, IVDs account for 22 percent of the spinal column length, which increases to 20 percent in the thoracic region, and finally 33 percent in the lumbar region(De Palma and Rothman 1970).

1.2.2 Anatomy of Intervertebral Disc

A human lumbar IVD is approximately 7~10 mm thick and has a 4 cm diameter measured along the anterior-to-posterior direction (Figure 1-2)(Roberts et al. 1989). The NP is situated in the center of the IVD, surrounded by the firm lamellar AF, as shown in Figure 1-2.

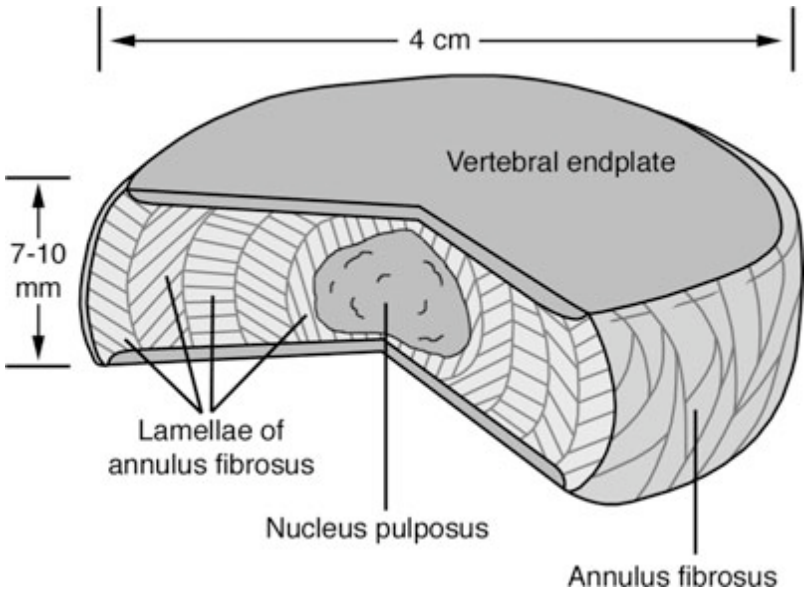

Figure 1-2. Diagram showing collagen fiber orientations within the lamellar structures of the AF. The typical dimensions of a healthy human lumbar IVD are shown in the diagram(Raj 2008).

The AF is composed of 15-25 concentric lamellae(Marchand and Ahmed 1990). Each lamellae is composed of type I collagen fibers positioned in parallel relative to the fibers in adjacent lamellae. Within the lamellae, the type I collagen fibers are oriented at a 60° angle relative to the vertical axis, and the direction of the angle alternates between adjacent lamellae, resulting in a crisscross pattern of collagen fibers between adjacent lamellae. The lamellae thickness increases significantly going from the outer AF to the inner AF in the anterior direction, and the thickness increase is much less significant in the posterior and lateral directions(Comper 1996b). As a result, the AF is thicker on the anterior side, which may contribute to the predominance of posterior protrusion of NP material(De Palma and Rothman 1970). A healthy IVD's NP contains a hydrated

proteoglycan (PG) gel enmeshed in an extracellular matrix composed of randomly oriented type II collagen fibers (Figure 1-3), and it occupies approximately 40% of the IVD's cross sectional area(De Palma and Rothman 1970).

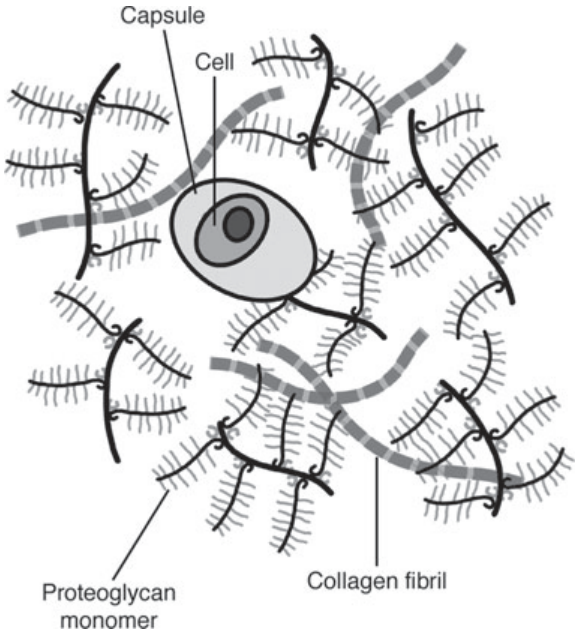

Figure 1-3. Diagram of the biochemical composition of the NP, showing aggregating PG monomers, type II collagen fibers, and encapsulated chondrocytes(Raj 2008).

Mature IVD NP has a very low cell density of ~5000 /mm^3, and the associated intracellular volume corresponds to less than 1% of the total NP volume(Maroudas et al. 1975). Therefore, the mature IVD NP is considered one of the most acellular tissues in human body.

1.2.3 Major Macromolecular Component – PG Aggrecan

In a typical IVD, water containing solutes, PG and collagen make up 90-95% of the total tissue mass(Comper 1996b). PG content is highest in the center of the NP and it decreases radially toward the AF, however even the outer AF has higher PG content than ligament or tendon(Comper 1996b). Large PGs in the NP resemble large aggregating PGs of articular cartilage known as aggrecans(Comper 1996b), which consists of up to 100 PG monomers attached to a hyaluronan (HA) chain via link protein molecules, as shown in Figure 1-4.

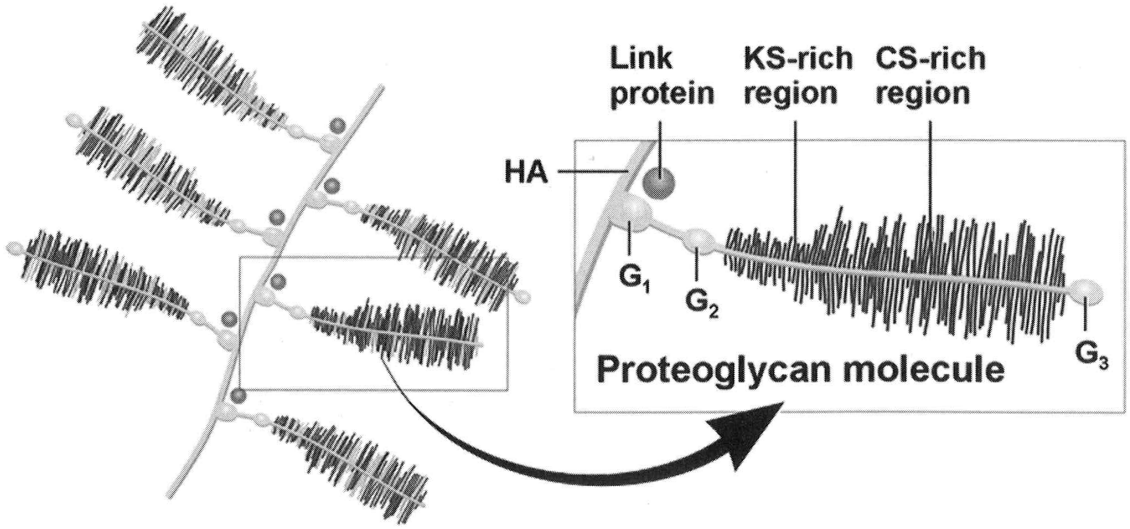

Figure 1-4. Overall structure of the PG aggrecan showing PG monomers attached to a HA chain. The detailed structure of a single PG monomer is shown on the right(Gunzburg, Szpalski and Andersson 2004).

Each PG monomer's central protein core is composed of up to 2000 amino acids. PG monomer contains regions of both globular and linear conformation. In a newly synthesized PG monomer, the G1,

G2 and G3 regions are globular, while the protein core between these regions assume a linear conformation with attached keratan sulfate (KS) and chondroitin sulfate (CS) repeating sugar chains(Gunzburg et al. 2004). These KS and CS sugar chains are extensively sulfated and carboxylated, making the whole molecule highly negatively charged at physiological pH(Urban and Winlove 2007). This negative charge attracts cations (primarily Na^+), in order to maintain electroneutrality in the interstitial water. The high sodium concentration ($[Na^+]$) induces a high osmotic pressure within the NP, allowing it to absorb water. As an IVD swells with water, it produces hydrostatic pressure, which is important to the load-resisting biomechanical property of the IVD. In human, IVDs from the lumbar region carry the highest compressive load, and their NPs have the highest PG content(Scott et al. 1994).

1.2.4 Major Macromolecular Component – Collagen

Collagen is the most abundant biomolecule present in the IVD, constituting approximately 70% of the dry weight in the AF and 6% to 25% of the dry weight in the NP(Ghosh 1988). IVD collagen fibers are responsible for anchoring the IVD to the vertebral bodies, and for making up a fibrous scaffold to trap the PG molecules within the NP(Comper 1996b). It has been documented that there are at least seven types of collagen present in the IVD(Ghosh 1988). However, 80% of the IVD collagens consist of

fibrillar collagens of type I (predominantly present in the AF) and type II (predominantly present in the NP). Type II collagen fibers have been found predominantly in tissues that support compressive loads(Eyre and Muir 1976). The NP's type II collagen fibers are loosely packed compared to those of articular cartilage, which allows these type II collagen fibers to maintain a higher intrafibrillar water content(Grynpas, Eyre and Kirschner 1980). Other types of IVD collagen exist in much smaller quantities, and they include types III, V, VI, IX, X, XII, and XIV(Gunzburg et al. 2004). Although the exact roles of these minor collagen types in IVD function are not completely understood, evidences seem to suggest that type III and X are involved in repair mechanism (Eyre, Matsui and Wu 2002a, Roberts et al. 1998), type VI is involved in cell adhesion(Roberts et al. 1991), and type IX regulates the size of type II collagen fibers(Wotton, Duance and Fryer 1988).

IVD collagen fibers are stabilized via various types of covalent cross-linking, with the greatest cross-link density in the NP(Comper 1996b). Type IX collagen can be covalently linked, in an anti-parallel fashion, to two type II collagen fibers(Maroudas 1990). It has also been demonstrated that type I and type II collagen molecules in the AF can copolymerize and form a single fibril via cross-link(Comper 1996b).

1.2.5 Minor Macromolecular Components

As mentioned previously, PG aggrecans account for the vast majority of PGs in the IVD. Another aggregating PG called versican(Sztrolovics et al. 2002) is also present in the IVD along with several smaller and non-aggrecating PG molecules such as lumican, decorin, and biglycan(Johnstone et al. 1993, Inkinen et al. 1998, Bianco et al. 1990). These minor PG molecules have shorter core protein containing few glycoaminoglycans (GAG), however they may contribute significantly to the physiological function of the IVD(Gunzburg et al. 2004).

Elastin is another minor IVD biomolecule that accounts to 1% to 2% of the IVD's dry weight(Mikawa et al. 1986). In IVD NP, the elastin fibers are radially oriented in the randomly orientated type II collagen network(Yu et al. 2002). In IVD AF, the elastin fibers lie between the lamellae and connect them in a radial pattern(Yu et al. 2002). Therefore, it is likely that elastin fibers play a role in the mechanical deformation of IVD under loading condition.

There are several types of glycoproteins present in the IVDs, such as fibronectin(Oegema et al. 2000) and tenascin(Gruber, Ingram and Hanley 2002). However, the exact functions of these glycoproteins in IVDs are not well understood. It has been speculated that they are active participants in cell signaling

and mechano-transduction in response to extracellular stimuli(Gunzburg et al. 2004).

1.2.6 Biomechanical Property of the Intervertebral Disc

In human, IVDs are constantly under load from both the body weight and spinal muscle activities. Therefore, the magnitude of the load is dependent on posture and the type of activities performed(Gunzburg et al. 2004). A relaxed individual lying in the supine position has been shown to exert 0.1 to 0.2 MPa of pressure on the lower lumbar IVDs, and this pressure increases to 0.6 to 0.7 MPa in a unsupported sitting position(Nachemson and Elfström 1970). Therefore, intradiscal pressure can increase approximately six-fold from nighttime to daytime activities. When experiencing a vertical load, the IVD has the ability to convert the vertical pressure into a horizontal force that acts on the AF, which increases the radius of the IVD and brings the adjacent vertebral endplates closer(De Palma and Rothman 1970). Horizontal deformation of the AF is likely achieved by the movement of its organized collagen lamella.

1.3 Intervertebral Disc Degeneration

1.3.1 Changes in Hydration

The biomechanical function of the IVD is heavily dependent on the water-binding property of the IVD NP, which generates the osmotic pressure necessary to resist the vertical load applied along the spinal column. IVD hydration has been shown to decrease progressively over time from up to 88% in healthy IVDs to approximately 69% in heavily degenerated IVDs(Schlesinger 1955). This loss of the IVD NP's capacity to imbibe water results in a greater fraction of the total vertical strain to be transferred to the AF, which may cause injury to the AF(De Palma and Rothman 1970).

1.3.2 Changes in PG Aggrecan

The initial phase of IVD degeneration is primarily marked by the breakdown and depletion of large PG aggrecans(Urban and McMullin 1988). As the aggrecans degrade into smaller fragments, they become more likely to diffuse out of the NP extracellular matrix and into the surrounding fluid. The loss of negatively charged GAG side chains reduces the fixed-charge density (FCD) of the NP, resulting in the loss of Na^+. The Na^+ cations function to maintain the osmotic pressure of the IVD, therefore the loss of Na^+ subsequently leads to decreases in IVD hydration and hydrostatic

pressure. Moreover, it has also been shown that the KS content of the GAG as well as the hyaluranon content increase with age.

1.3.3 Changes in Collagen

IVD collagen has previously been shown to either exhibit no content change after maturation or to increase with aging(Mallen 1962, Davidson and Woodhall 1959, Naylor 1962). The NP type II collagen fibers show increased orientation and crystallinity with aging. The total collagen content of the NP has been shown to increase from 15% in the first decade of an individual's life to 20% afterward, while the AF collagen content maintains steady at 50% throughout life(Murayama 1972). Regardless of whether the total IVD collagen content changes with aging, the relative density of collagen is likely to increase due to reduced hydration in degenerated IVDs.

1.4 Paradigms of Age-Dependent Degeneration and Degenerative Disc Disease

Aging-related IVD degenerative changes are similar to the symptoms of degenerative disc disease, thus it is difficult to differentiate between IVD degeneration due to aging and IVD degeneration due to pathological processes(Boos et al. 2002). Currently, it is not yet clear whether aging and degenerative

disc disease are unique processes or an identical process occurring over different timescales.

1.5 Socio-economic Significance of Intervertebral Disc Degeneration

Degeneration of the IVD is the most common cause of back-related disability among North American adults(Errico 2005). IVD degeneration has been shown to be a significant etiological component to the onset of low-back-pain (LBP)(Jayson 1976). LBP exacts a heavy economic toll on society in the form of rising healthcare cost and lost work productivity, which combines to amount to between $100 and $200 billion dollars annually(Katz 2006). LBP is also highly prevalent, with more than 80% of the population will experience an episode of LBP in their lifetime(Rubin 2007), and the lifetime recurrence rate is as high as 85%(van Tulder, Koes and Bombardier 2002). Between acute and chronic LBP cases, the prevalence of chronic LBP has been shown to be increasing over a 14-year interval, rising from 3.9% in 1992 to 10.2% in 2006(Freburger et al. 2009). Individuals with chronic LBP are more likely to seek out healthcare(W and Burdorf 2004) and to demand additional healthcare services(Carey et al. 1995), both of which can further drive up the cost of healthcare.

1.6 Current Diagnostic Methods for Intervertebral Disc Degeneration

1.6.1 T_1- and T_2-Weighted MRI

Previous studies have investigated T_1 and T_2 relaxation parameters in IVD degeneration(Morgan and Saifuddin 1999, Khanna et al. 2002, Boos et al. 1997, Cassar-Pullicino 1998). Both T_1 and T_2 relaxation parameters have been shown to vary with tissue disease state(Bottomley et al. 1987, Mathur-De Vre 1984), however the changes are complicated in nature and therefore cannot be attributed to single tissue parameter(Wehrli, Shaw and Kneeland 1988). T_2 relaxation time constant has been shown to be sensitive to biological changes in the articular cartilage, however the changes in T_2 relaxation time constant due to degeneration may not be solely contributed by changes in IVD macromolecule content(Menezes et al. 2004).

1.6.2 Thompson and Pfirrmann Grades

Current clinical classifications of IVD degeneration rely on grading schemes such as the Pfirrmann grade(Pfirrmann et al. 2001) based on T_2-weighted MR images, and the Thompson grade assessed from photographs of surgically removed IVD sagittal sections(Thompson et al. 1990). Both the Pfirrmann and the Thompson grades are discontinuous scores chosen based on a collective of IVD morphological features. As a result, they are

not quantitative measurements of IVD degeneration, and they are prone to observer-bias.

1.6.3 Delayed Gadolinium Enhancement MRI of Cartilage (dGEMRIC)

dGEMRIC is a technique that involves an intravenous injection of gadolinium (Gd) based contrast dye, and it has been previously used to study IVD degeneration. Gd is a paramagnetic element and a T_1 shortening agent. Its principal function as a MRI contrast dye is to increase the T_1 relaxation rate of adjacent proton nuclei. One recent study concluded a significant correlation between IVD degeneration and increase in T_1 relaxation rate(Niinimaki et al. 2006). A separate study has concluded that increases in IVD tissue T_1 relaxation rate from dGEMRIC technique is correlated with tissue GAG content(Vaga et al. 2008). However, Gd-based contrast dye has been implicated as the cause of a cutaneous and systemic fibrosis condition named nephrogenic system fibrosis (NSF) in 2000(Cowper et al. 2000). A study has shown that NSF affects approximately 3.5% of patients with glomerular filtration rate <30 mL/min/1.73m^2(Janus et al.). Therefore, the clinical applicability of dGEMRIC technique is currently being re-evaluated.

1.6.4 Discography

Discography involves the injection of a radiographic contrast into an IVD NP, in order to evaluate both its morphology and its pain response(Anderson 2004). Discography is a painful and highly invasive procedures, and it has been shown that the needle puncture injury caused by discography has both immediate and progressive mechanical and biological consequences on the IVD(Korecki, Costi and Iatridis 2008). In addition, there is preliminary evidence that discography also contributes to the formation of acute Schmorl nodes(Pilet et al. 2009).

1.7 Imaging Technique - $T_{1\rho}$ (Spin-lock) MRI

1.7.1 Spin-lock Pulse Implementation

$T_{1\rho}$ is the spin-lattice relaxation rate in the rotating frame. In a $T_{1\rho}$ RF pulse sequence for MRI, $T_{1\rho}$ contrast is achieved using a spin-lock pulse cluster shown in Figure 1-5.

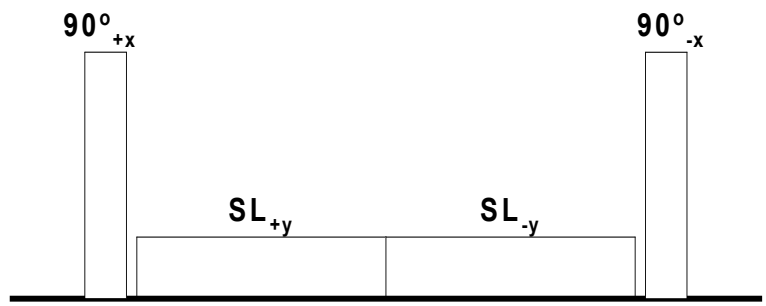

Figure 1-5. Diagram of the $T_{1\rho}$ magnetization preparation pulse cluster, which is composed of two opposite-phase spin-lock pulses enclosed by a pair of 90° pulses.

The first RF pulse in the cluster tips the longitudinal magnetization into the transverse plane. Next, two RF pulses of opposite phase are applied parallel and anti-parallel to the transverse magnetization. During the application of the spin-locking RF pulse, the transverse magnetization is spin-locked and the transverse magnetization undergoes exponential relaxation in the presence of a spin-lock field (B_{SL}) according to an exponential constant $T_{1\rho}$ instead of T_2. The phase-alternating spin-lock pulse lobes are designed to refocus the effect of an inhomogeneous B_{SL} fields(Charagundla et al. 2003). The last RF pulse in the spin-lock cluster restores the magnetization to the longitudinal axis.

1.7.2 $T_{1\rho}$ Relaxation Mechanism in IVD

Several types of spin-spin interactions may dominate the transverse magnetization decay during $T_{1\rho}$ relaxation, depending on the amplitude of the spin-lock pulse. The first one is spin

relaxation from random fluctuations of the local magnetic fields due to random motions of the proton magnetic dipoles. The hydroxyl and amine groups of aggrecans carry magnetic dipoles, and the rotational and translational motions of the aggrecans results in the fluctuations of these magnetic dipoles. The second spin relaxation mechanism is the proton exchange between chemically shifted macromolecular protons and bulk water protons, such as the proton exchange between PG's hydroxyl and amine groups with bulk water protons. The third spin relaxation mechanism is the residual dipolar interaction due to motional anisotropy of collagen-bound water protons. The motional anisotropy may be contributed by cross-linked type II collagen fibers in IVD NP.

1.7.3 $T_{1\rho}$ Contrast in Biological Tissues

Previous studies have utilized $T_{1\rho}$ MR spectroscopy and imaging to study tumors, muscle, myocardium, blood flow and cartilage(Santyr, Henkelman and Bronskill 1989, Lamminen et al. 1993, Dixon et al. 1996, Markkola et al. 1997, Charagundla et al. 1998, Mlynarik et al. 1999, Grohn et al. 2000, Poptani et al. 2001, Duvvuri et al. 2001, Borthakur et al. 2004). Previous studies have shown that $T_{1\rho}$ relaxation time constant is closely correlated to PG concentration ([PG]) in articular cartilage(Akella et al. 2001, Borthakur et al. 2000). Another study has shown a correlation between IVD $T_{1\rho}$ relaxation time

constant and the Pfirrmann grade in asymptomatic 40-60 year old subjects *in vivo*(Auerbach et al. 2006). At last, $T_{1\rho}$ relaxation time constant has demonstrated a stronger correlation with [PG] changes in bovine articular cartilage compared to T_2 relaxation time constant(Regatte et al. 2002).

1.7.4 Quantitative $T_{1\rho}$ Mapping

Typically a series of $T_{1\rho}$-weighted images with different spin-lock pulse duration times (TSL) are acquired. A map of $T_{1\rho}$ relaxation time constants can then be computed from the $T_{1\rho}$-weighted images on a pixel-by-pixel basis according to Equation 1-1:

$$S = S_o \cdot e^{-TSL/T_{1\rho}} \qquad \text{Equation 1-1}$$

Where S is the image signal intensity and S_o is the maximum signal intensity.

1.8 Imaging Technique - Sodium MRI

1.8.1 Spin Dynamics of Sodium Nuclei

Sodium is a spin 3/2 nucleus. When the nuclear spin is greater than 1/2, nuclear charge distribution is not spherical. Sodium nuclear charge contains a nuclear quadrupole moment that resembles the d orbital of a hydrogen atom. Sodium nucleus's

quadrupole moment may interact strongly with the electric field gradient generated by the surrounding electron cloud. This quadrupole interaction could be in the order of several MHz(Levitt 2008). Sodium's nuclear quadrupole interaction is dependent on the orientation, magnitude, and time scale of the electric field gradient produced by the electron cloud surrounding the nucleus. In an isotropic liquid system, the nuclear quadrupolar interaction is averaged to zero due to the rapid rotational motion of the sodium nuclei. In an anisotropic liquid system, such as in biological tissue where sodium nuclei may associate with macromolecular structures, the nuclear quadrupolar interaction has a non-zero average due to motional anisotropy. The anisotropic system most likely approximates the environment in IVD experienced by the sodium nuclei. Nuclear quadrupole interaction is the most significant internal nuclear interaction of sodium nuclei, and it is partially responsible for the rapid decay of sodium's transverse magnetization.

1.8.2 Sodium Biexponential T_2^* Relaxation

The non-zero nuclear quadrupole interaction of sodium in an anisotropic liquid system shifts its degenerate Zeeman energy states, provided that the Zeeman interaction is greater than the nuclear quadrupole interaction, as shown in Figure 1-6.

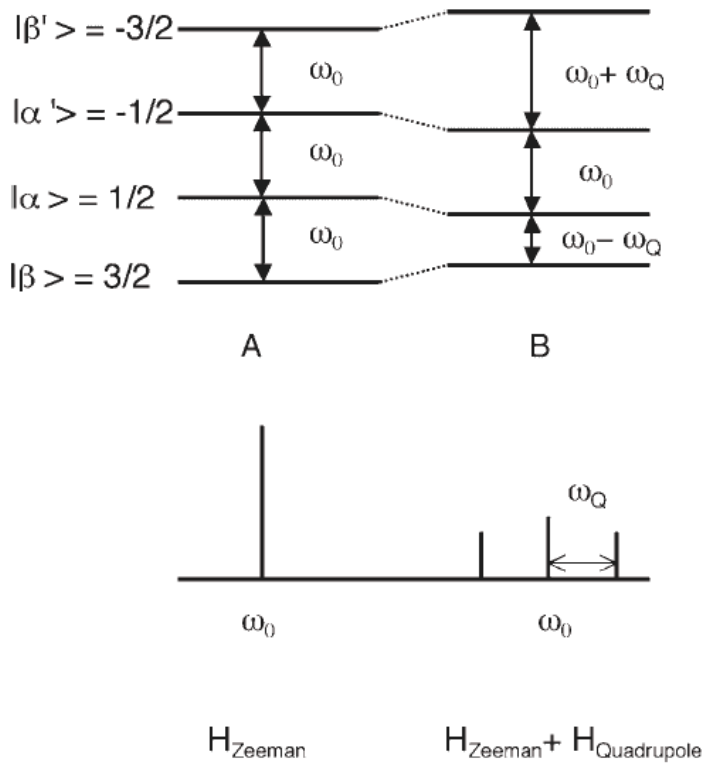

Figure 1-6. A diagram of sodium spin-3/2 nuclear energy states' Zeeman splitting pattern with nuclear quadrupole interaction averaged to zero (A) and with non-zero nuclear quadrupole interaction (B). Note that the presence of nuclear quadrupole interaction creates three distinct spectral peaks. ω_Q is the nuclear quadrupole interaction frequency(Borthakur et al. 2006).

The frequency differences between sodium spin-3/2 nucleus's four degenerate energy levels are equal when the nuclear quadrupole interaction is averaged to zero, resulting in a single spectral peak at the resonance frequency of ω_o. However, with a non-zero nuclear quadrupole interaction, the frequency differences between adjacent energy levels changed and three spectral peaks (ω_o, $\omega_o+\omega_Q$, $\omega_o-\omega_Q$) are observed in return. The presence of three spectral peaks gives rise to the biexponential T_2 relaxation characteristic of sodium spin-3/2 nucleus with non-zero nuclear quadrupole interaction. The short T_2 relaxation component

constitutes 60% of total sodium signal, and it represents the combined $\omega_o+\omega_Q$ and $\omega_o-\omega_Q$ spectral peaks. The long T_2 relaxation component constitutes 40% of the total sodium signal, and it is represented by the ω_o spectral peak(Hubbard 1970).

1.8.3 Advantages and Disadvantages of Sodium Magnetic Resonance Imaging

Sodium MRI has been applied to the imaging of heart infarction, brain, and spine(Hillenbrand et al. 2005, Stobbe and Beaulieu 2005, Insko, Clayton and Elliott 2002). Sodium MRI is highly specific to the sodium content in biological tissue, which makes it highly sensitive to pathologies that involve changes in tissue sodium concentration, such as IVD degeneration. A previous sodium MRI study of bovine articular cartilage has concluded that the FCD measurement obtained using sodium MRI correlates closely with the FCD measurement computed using standard 1,9-dimethylmethylene blue PG assay(Shapiro et al. 2002). However, the SNR of sodium MRI is significantly lower when compared to the SNR of proton MRI. This disadvantage limits sodium MRI's role in *in vivo* applications. The three primary factors contributing to sodium MRI's low SNR are listed as follows, in the order of importance. The first factor is the low natural concentration of sodium in tissue. The second factor leading to the low SNR of sodium MRI is sodium's lower gyromagnetic ratio (γ=11.26 MHz/T) compared to proton's (γ=42.57 MHz/T), which results in a smaller equilibrium

magnetization. The third factor is the short T_2 relaxation time constant of sodium nuclei, which causes rapid relaxation of sodium's measurable transverse magnetization. In order to compensate for the low SNR of sodium MRI, pulse sequences typically require short echo time (TE) along with repeated signal averaging.

1.9 Imaging Technique - Magnetization Transfer MRI

1.9.1 Two Proton Spin Pools Exchange Model

An important contrast in MRI is the enhancement of free water proton spin relaxation via dipolar cross relaxation between macromolecule-bound water protons and macromolecular protons (Figure 1-7), in a process called magnetization transfer (MT)(Wolff and Balaban 1989).

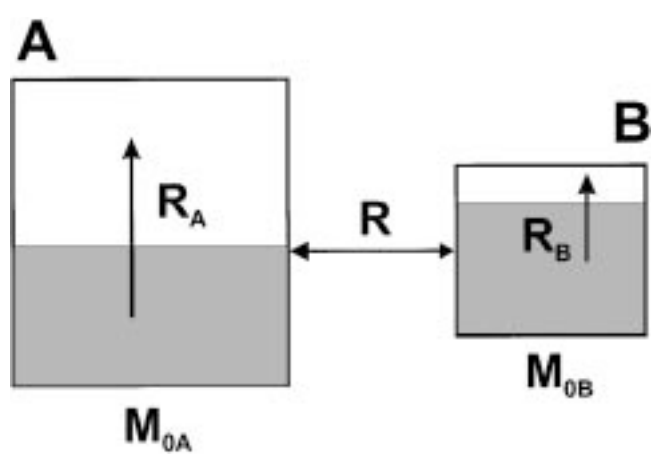

Figure 1-7. A diagram of the two-pool model of MT. The gray volume in pool A (free protons) and B (macromolecule-bound protons) represents saturated spins. R_A and R_B represent the T_1 relaxation rates of the free

pool and the macromolecule-bound proton pool, respectively. R represents the rate of MT between the two pools(Henkelman, Stanisz and Graham 2001).

Previous studies have determined that the hydroxyl, amine, and possibly carboxyl groups on the surface of macromolecules act as sites for MT(Ceckler et al. 1992). The relaxation process is facilitated by hydrogen-bonding between macromolecule protons and bulk water protons, and it requires that the correlation time of the macromolecule/bulk water proton interaction to be greater than the duration required for MT(Ceckler et al. 1992). Previous studies have concluded that a correlation time greater than 10^{-9} s is necessary for MT to occur(Wolff and Balaban 1989).

1.9.2 Quantification of Magnetization Transfer

MT effect can be observed in a saturation transfer experiment, in which an off-resonance RF pulse is applied to saturate the equilibrium magnetization of the restricted proton spins, as shown in Figure 1-8.

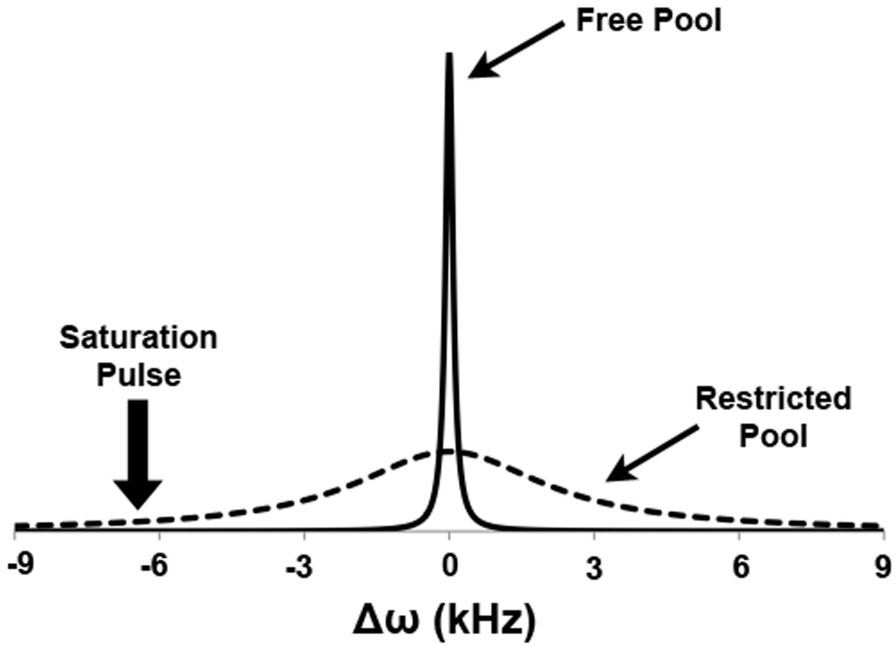

Figure 1-8. Absorption spectra of the restricted pool proton spins (dashed line) and the free water pool proton spins (solid line). The placement of the off-resonance saturation pulse is marked by the solid arrow.

The off-resonance RF pulse ideally would saturate only the 20-40 kHz broad macromolecule proton magnetization, while leaving the magnetization of the narrow (~15 Hz) bulk water proton magnetization relatively unchanged. However, since the macromolecule protons are hydrogen-bonded to some bulk water protons and undergoing dipolar cross relaxation, the detected bulk water magnetization also decreases. MT effect is typically quantified with magnetization transfer ratio (MTR), which is defined by Equation 1-2:

$$MTR = \frac{M_o - M_{SAT}}{M_o} = 1 - \left(\frac{M_{dir}}{M_o} + \frac{M_{MT}}{M_o} \right) \qquad \text{Equation 1-2}$$

In Equation 1-2, M_o is the signal measured without the off-resonance saturation pulse, and M_{SAT} is the signal measured with the off-resonance saturation pulse. However, the observed MT effect consists of two components, as shown in Figure 1-9.

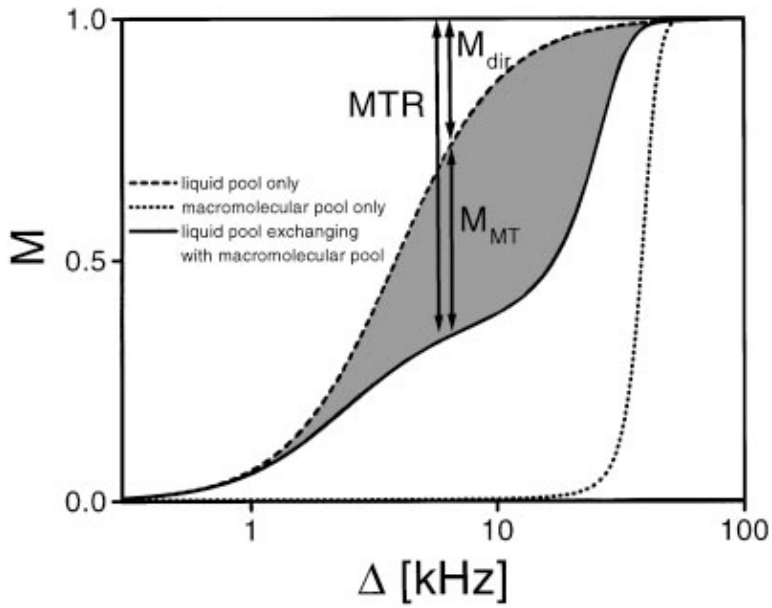

Figure 1-9. Diagram of the MT effect as a function of off-resonance frequency for a 4% agarose phantom. The graph shows both the direct saturation effect (M_{dir}) and the MT effect (M_{MT}), which is represented by the shaded region(Henkelman et al. 2001).

M_{dir} is the direct saturation effect that the off-resonance pulse has on bulk water proton magnetization as a result of RF bleed-over effect, and M_{MT} is the actual MT effect.

1.9.3 Magnetization Transfer in Articular Cartilage

Articular cartilage belongs to the same fibrocartilage family as IVDs. They are both composed of primarily collagen and PG. A previous study by Kim *et al.* has demonstrated that type II

collagen fibers are predominantly responsible for the observed MT effect in articular cartilage(Kim et al. 1993). The dominance of collagen in the observed MT effect was observed in the z-spectra of collagen and PG phantoms as shown in Figure 1-10, which depicts the observed free water proton saturation at a range of off-resonance saturation frequencies.

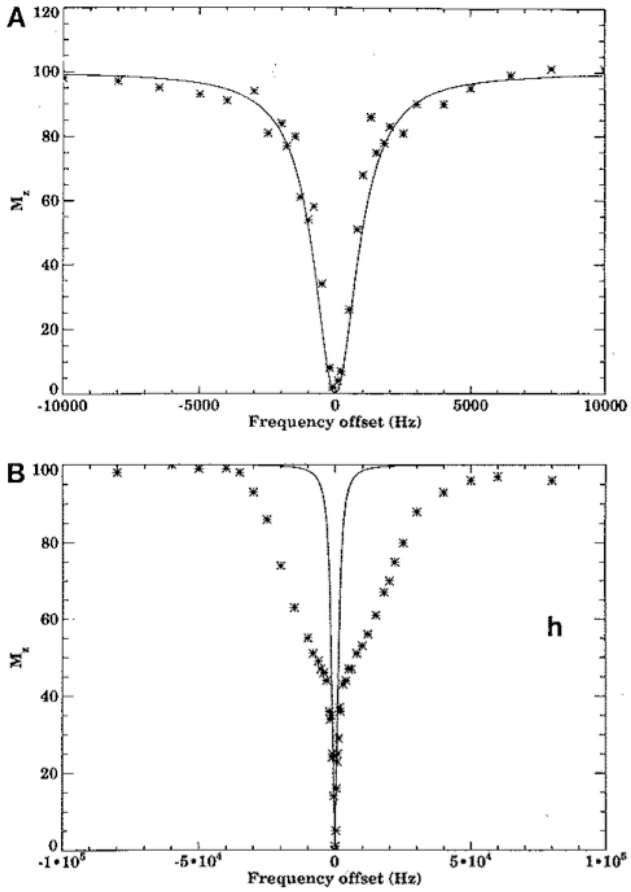

Figure 1-10. Diagram showing the direct saturation effect and MT effect of (A.) PG and (B.) collagen. The solid line shows the simulated direct saturation effect of the off-resonance pulse on the bulk water magnetization, while the crosses mark the measured bulk water magnetization of the PG and collagen phantoms with potential contribution from MT effect(Kim et al. 1993).

In Figure 1-10, the solid line shows the direct saturation effect simulated using Bloch equation and appropriate T_1 and T_2 values, assuming a Lorentzian shape for the bulk water resonance peak. The crosses mark the bulk water proton magnetization following the MT pulse. In the case of PG, the decrease in bulk water magnetization is nearly completely dominated by direct saturation effect, whereas in the case of collagen, there is a MT effect in addition to direct saturation effect. Collagen has a large number of hydrophilic hydroxyproline groups contributing to the MT effect, and these hydrophilic groups are motional-restricted with a correlation time around 10^{-8} s, which is sufficiently slow for MT effect to take place(Ceckler et al. 1992). Even though PG has hydroxyl groups, however they have been shown to be highly mobile in a previous ^{13}C NMR study on cartilage. The high mobility of the PG hydroxyl groups gives it a shorter correlation time, making them less likely to exhibit MT effect(Torchia, Hasson and Hascall 1977). A previous MT experiment of cadaveric IVDs observed deviation in MT rate between healthy and degenerated IVDs, and the MT rate was shown to be correlated with IVD collagen content(Paajanen et al. 1994).

1.10 Dissertation Overview

IVD degeneration is a possible cause of LBP, which bears tremendous socioeconomic costs. The detailed mechanism of IVD

degeneration, especially its biomolecular aspect, is currently poorly understood in an *in vivo* setting. Thus there is increasingly a need for the non-invasive diagnosis and quantification of the degenerative process. MRI is a non-invasive imaging modality capable of producing contrast sensitive to biomolecular compounds. Therefore, the primary objective of this dissertation research project is to develop MRI techniques capable of the non-invasive quantification of IVD biomolecular composition *in vivo*. Three MRI techniques - MT MRI, $T_{1\rho}$ MRI and sodium MRI were separately validated of their specificities for IVD biomolecular composition. Next, they were applied in an *in vivo* setting to demonstrate these techniques' utility in quantifying IVD degeneration in a clinically relevant setting.

This dissertation is divided into 7 chapters. After this introductory chapter focused on background information, the second chapter describes a study that validated sodium MRI as a technique capable of accurately quantifying IVD [Na^+], FCD and [PG]. This goal was achieved by statistically comparing *ex vivo* bovine IVD NP [Na^+] and FCD measurements obtained from sodium MRI with [PG] values obtained using standard 1,9-dimethylmethylene blue assay.

Sodium MRI can accurately measure NP [Na^+] values, which can subsequently be used to compute tissue osmotic pressure according to a mathematical model developed by a previous study. Chapter three improved upon this mathematical model by compensating for

collagen intrafibrillar water content. Next, a custom-engineered imaging platform was constructed for self-coregistered sodium and $T_{1\rho}$ MRI of *ex vivo* bovine IVD samples. IVD NP $T_{1\rho}$ relaxation time constant was then correlated with osmotic pressure calculated from sodium MRI. $T_{1\rho}$ MRI has significantly higher SNR efficiency compared to sodium MRI, which makes $T_{1\rho}$ MRI a potentially more clinically viable technique.

The second and third chapters of this dissertation focus mainly on PG aggrecans and the osmotic pressure they produce. Chapter four describes an *in vivo* MT MRI study that both validates MT MRI's role in the quantification of IVD collagen as well as investigates collagen content change with respect to Pfirrmann grade, which is an accepted grading scheme of IVD degeneration.

Sodium MRI has poor SNR efficiency, therefore the sodium MRI studies described in chapter two and three used *ex vivo* IVD samples with long scanning time. To make sodium MRI applicable in a clinical setting, there is a need to conduct the study on an ultra-high field strength MRI scanner to improve SNR efficiency and reduce scanning time. Chapter five describes an *ex vivo* study that investigated the biexponential T_2 relaxation of IVD sodium. The long and short T_2 relaxation time constants of sodium were calculated and used to optimize the *in vivo* sodium MRI protocol in the subsequent chapter.

Chapter six focuses on *in vivo* sodium MRI on the 7 T MRI scanner, using the optimized imaging parameters obtained from chapter five and a custom-engineered single loop surface RF coil. The sodium signal was compensated for both T_2* relaxation and B_1 inhomogeneity before [Na^+] value was computed. The IVD [Na^+] values were then correlated with corresponding Pfirrmann grades to elucidate the course of IVD NP [Na^+] change in response to IVD degeneration. At last, preliminary data on the cross comparison of *in vivo* MT MRI, $T_{1\rho}$ MRI and sodium MRI of lumbar IVDs were acquired to establish both the clinical viability of the techniques as well as their sensitivity for subtle changes in IVD biochemistry *in vivo*.

At last, the seventh chapter summarizes all previous chapters and addresses the significance of this dissertation research project.

Chapter 2: Validation of Sodium MRI's Role in Non-Invasive Measurement of Proteoglycan Content in Intervertebral Discs

2.1 Synopsis

The aim of this study is to validate sodium MRI as a technique for the non-invasive quantification of PG concentration ([PG]) in the IVDs, by determining the existence of a linear correlation between IVD sodium concentration ([Na^+]) and [PG], which was measured with standard 1,9-dimethylmethylene (DMMB) blue assay. Sodium MR images of bovine IVDs were acquired and converted into [Na^+] maps. NP punch samples were systematically removed from the discs for DMMB assay. The punch removal locations were photographically recorded and applied to the [Na^+] maps to extract the [Na^+] measurements for comparison. The linear regression fit of [Na^+] versus [PG] data yielded a significant linear correlation coefficient of 0.71 at $p<0.01$. Next, *in vivo* sodium MRI was carried out for a pair of symptomatic and asymptomatic human subjects. The *in vivo* sodium MR image of the symptomatic subject showed significant [Na^+] decrease when compared to that of the asymptomatic subject. In conclusion, sodium MRI's demonstrated sensitivity for IVD [PG] makes it a promising diagnostic tool for the initial phase of IVD degeneration.

2.2 Introduction

Conventional T_1 and T_2 imaging techniques are useful for observing morphological changes in the IVDs. However, these MRI findings are results of decreased disc hydration as well as structural changes, typical in the later stages of degenerative disc disease (DDD)(Saifuddin, Mitchell and Taylor 1999). The initial phase of disc degeneration is primarily marked by the breakdown of large PG aggrecans, the most common form of PG in the extracellular matrix of the NP, leading eventually to decreases in disc hydration and hydrostatic pressure(Antoniou et al. 1996, Urban and McMullin 1988). The initial phase of disc degeneration presents itself as subtle biochemical changes, which are difficult for conventional MRI to detect.

Instead, other MRI techniques that are more specific to the biochemistry of PG can be utilized to detect PG depletion. In healthy discs, PG molecules aggregate together and form large PG aggrecans with around 100 GAG side chains. These side chains are extensively sulfated and carboxylated, which makes the whole molecule highly negatively charged at physiological pH(Urban and Winlove 2007). This negative charge attracts cations (primarily Na^+), therefore a measurement of [Na^+] directly estimates [PG]. Previous research on sodium MRI have focused on sodium MRI based [Na^+] quantification techniques, such as sodium MRI of *ex vivo* bovine articular cartilage samples(Shapiro et al. 2000),

correlation of [Na^+] measured from sodium MRI and PG assay on bovine articular cartilage samples(Shapiro et al. 2002), *in vivo* measurement of articular cartilage [Na^+] in a porcine osteoarthritis model(Wheaton et al. 2004), in vivo sodium MRI of human wrist articular cartilage(Borthakur et al. 2002), and sodium MRI and subsequent [Na^+] quantification of IVD *in vivo*(Insko et al. 2002). Earlier biochemistry study demonstrated a positively linear correlation between GAG measurements obtained with 1, 9-dimethylmethylene blue (DMMB) assay and [Na^+] in human IVD samples (Urban and Winlove 2007). However, a direct link between disc [Na^+] measured from sodium MRI and actual [PG] remains to be determined, and this relationship is critical for the validation of sodium MRI as a non-invasive diagnostic tool for the initial stage of DDD. Early diagnosis of DDD could promote development and testing of new therapeutics aimed at modifying the disease progression as well as preventive care.

2.3 Methods

2.3.1 Sodium MRI of Bovine Intervertebral Disc

Two intact bovine lumbar spines were obtained from a local abattoir (Bierig Brothers, Vineland NJ), within a few hours of slaughter. From each spine specimen, the last two intact caudal discs from the lower lumbar region were surgically harvested. The

bones on each side of the disc were trimmed with a bone saw to include the endplate and approximately 1 cm of bony tissue, thus each disc specimen contained a single caudal disc sandwiched between vertebral endplates, preserving the integrity of the motion segment. MRI was performed on a 3 T Siemens Trio clinical MRI scanner (Erlangen, Germany) equipped with a broadband amplifier and receiver at the Hospital of the University of Pennsylvania. Tissue samples were placed inside a custom-made low-pass quadrature birdcage RF coil tuned to sodium frequency (32.6 MHz) at 3 T. The RF coil was 17 cm in diameter and 12.5 cm long, and contained 16 struts. The two receiver ports were inductively coupled to the coil and oriented 90° relative to each other. Five 10% agarose gel phantoms containing 100 mM, 150 mM, 200 mM, 250 mM, and 300 mM [Na^+] were imaged alongside each specimen for eventual [Na^+] calibration.

The vendor's 3D FLASH MRI pulse sequence was used to acquire all sodium images. Imaging parameters were as follows: TE/TR = 6/30 ms, flip angle = 90°, FOV = 15 x 15 cm, matrix size = 128 x 128, slices = 128, slice thickness = 1.2 mm, BW = 60 Hz/Pixel, signal average = 75. These parameters were chosen to obtain a minimum SNR of 15:1 for an isotropic voxel size of 1.2 mm^3. The isotropic voxel size allowed us to reconstruct images in any orientation from a single 3D data set.

2.3.2 Mapping [Na^+]

The pixel-wise [Na^+] calculation based on sodium phantom signals was carried out according to the method described by Shapiro *et al*(Shapiro et al. 2002). The sodium signals from disc and phantoms were corrected separately for T_1 and T_2^* decays according to the following equation:

$$S_{corrected} = \frac{\sin(FA)\cdot\left(1-e^{-TR/T_1}\right)\cdot e^{-TE/T_2^*}}{1-\cos(FA)\cdot e^{-TR/T_1}}\cdot S_o \qquad \text{Equation 2-1}$$

where FA is the flip angle, and S_o is the original sodium signal intensity. Sodium T_1 and T_2^* of the disc and phantoms were computed from the results of progressive saturation experiments, yielding T_1 relaxation time constants of 22 ms and 23 ms for the disc and phantom, respectively. The T_2^* relaxation time constants of the disc and phantom were computed as 16 ms and 8 ms, respectively. After compensating for T_1 and T_2^* relaxation, the average sodium signal from each phantom of known [Na^+] was plotted on a calibration curve of [Na^+] versus sodium signal. The slope and y-intercept of the linear fit of the calibration curve was then used to compute a 3D [Na^+] map of the disc.

2.3.3 Mapping FCD

FCD is directly calculated from [Na^+] measurements by solving the electroneutrality equations of tissue and fluid while assuming ideal Donnan equilibrium condition(Lesperance, Gray and Burstein

1992). The electroneutrality condition dictates that the expressions in Equation 2-2 have to be true.

$$\begin{aligned} &\text{In tissue: } \left[Na^{+}\right]_{t} - \left[Cl^{-}\right]_{t} + FCD = 0 \\ &\text{In fluid: } \left[Na^{+}\right]_{f} - \left[Cl^{-}\right]_{f} = 0 \end{aligned} \qquad \text{Equation 2-2}$$

Subscript *t* implies tissue, and subscript *f* implies surrounding fluid. The lack of $[Cl^{-}]$ knowledge prevents the direct calculation of the FCD from the electroneutrality condition. Instead, the Donnan equilibrium condition is assumed across the tissue/fluid system, resulting in Equation 2-3.

$$\psi_{t}^{2}[Na^{+}]_{t}[Cl^{-}]_{t} = \psi_{f}^{2}[Na^{+}]_{f}[Cl^{-}]_{f} \qquad \text{Equation 2-3}$$

ψ is the mean ionic activity coefficient. Assuming ideal Donnan equilibrium condition, the mean ionic activity coefficients in tissue and surrounding fluid are equal. Therefore, Equation 2-3 can be simplified to Equation 2-4.

$$\left[Na^{+}\right]_{t}\left[Cl^{-}\right]_{t} = \left[Na^{+}\right]_{f}\left[Cl^{-}\right]_{f} \qquad \text{Equation 2-4}$$

Substituting Equation 2-4 back to the electroneutrality condition produces an expression that calculates FCD based on tissue and surrounding fluid $[Na^{+}]$, as shown in Equation 2-5.

$$FCD = \frac{\left[Na^{+}\right]_{f}^{2}}{\left[Na^{+}\right]_{t}} - \left[Na^{+}\right]_{t} \qquad \text{Equation 2-5}$$

In Equation 2-5, subscript *t* implies tissue and subscript *f* implies surrounding fluid. In the context of this study, $[Na^{+}]_{f}$

was assumed to be the serum sodium concentration of 150 mM, and $[Na^+]_t$ was the previously computed $[Na^+]$ map. Application of Equation 2-5 pixel-wise to the $[Na^+]$ map yielded a 3D FCD map of the spine.

2.3.4 Proteoglycan Assay

After sodium MRI, the IVDs were isolated via sharp dissection, leaving the AF and the NP intact as shown in Figure 1. A series of ordered 4 mm diameter punches were harvested from the NP as indicated in the overlay on Figure 2-1 for DMMB assay.

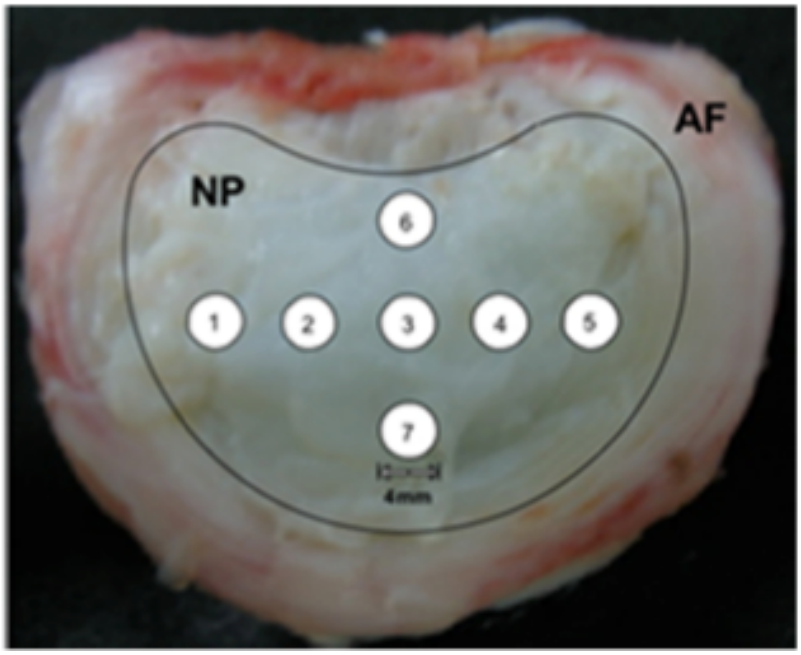

Figure 2-1. A photo of a dissected disc, with an overlay showing the numbered locations of the hole punches removed for the PG assay. The boundary between the AF and the NP compartments are marked.

After punches were removed, the discs were photographed against a dark background using a digital camera. These photographs were

used later to generate image masks for reporting [Na^+] values from the exact region where the hole punches were removed. The wet weight of the punch sample was determined, followed by sample digestion in 1 mL of 150 µg/mL papain (Sigma Chemicals, St. Louis, MO) for 16-24 hours at 60°C. Solutions were diluted and determination of sulfated-GAG content was performed using DMMB in a microplate reader assay. In a 96-well plate, 50 µL of each sample was added in duplicates and 200 µL of DMMB solution was added to each well. The plate was read immediately after addition of the DMMB solution. Each sample's absorbance at 525 nm was measured using a SpectraMax M5 microplate reader (Molecular Devices, Sunnyvale, CA). Concentration was calculated from a standard curve of shark chondroitin sulfate C (Sigma Chemicals, St. Louis, MO), which ranged from 0-100 µg/mL.

2.3.5 Image Processing and Data Analyses

All sodium MR images and photographs were transferred to a Mac Mini computer (Apple, Cupertino, CA). Subsequent data processing and analysis were carried out using algorithms developed with MATLAB software (Mathworks, Natick, MA). Photographs of each dissected disc were interpolated to the same spatial resolution as the sodium MR images (1.2 mm^2). Intensity thresholding of the photographs resulted in binary masks showing the region of interest (ROI) where punches were removed. The location of each ROI was used to report average [Na^+] from the maps. An automatic

co-registration routine applied step-wise in-plane rotation and translation while optimizing the linear regression fit of [Na^+] map ROIs and the PG assay results. The standard deviation of [Na^+] for each ROI was recorded as the error. Linear regression analysis by least-square-fit was carried out on the 28 pairs of [PG] and [Na^+] measurements, with the [PG] measurement assigned as the independent variable. The correlation coefficient as well as the y-intercept of the fit was computed.

2.3.6 Mapping [Na^+] *in vivo*

All experiments involving human subjects were carried out with approval of the Institutional Review Board at our institution. Two young male subjects were recruited for this study (mean age = 24.5 years). One subject was asymptomatic while the second subject has a history of LBP. Subjects were instructed to read and sign the pertinent consent forms prior to scan. The subjects were imaged on the same Siemens Trio 3 T clinical scanner with a custom-built 20 cm diameter transmit/receive surface coil tuned to sodium's resonance frequency. Each subject lay supine on top of the coil, and was positioned such that his lower lumbar region was directly above the coil. The same sodium MRI protocol was followed as that of the specimen imaging with the following changes: FOV = 40 cm x 40 cm, matrix size = 128 x 64, slices = 32, slice thickness = 12 mm, average = 22, orientation = sagittal, for a total imaging time of under 30 minutes. Image

analysis was carried out as described earlier. The 128 x 64 image matrix was interpolated bilinearly to 128 x 128. Images were corrected for surface coil B_1 inhomogeneity. This task was accomplished by acquiring the image of a large sodium agarose phantom using the same surface coil and imaging parameters. Sodium MRI of the subjects were normalized at each pixel location using the phantom image after the two data sets had been manually co-registered. $[Na^+]$ maps were computed from the corrected sodium MR image by referencing cerebral spinal fluid (CSF) $[Na^+]$ as 150 mM.

2.4 Results

A 3D rendered representation of a typical disc is shown in Figure 2-2, along with an anterior cutaway section depicting both coronal and sagittal planes of the $[Na^+]$ color map. The dashed lines show where the cutaway section was extracted from the whole disc.

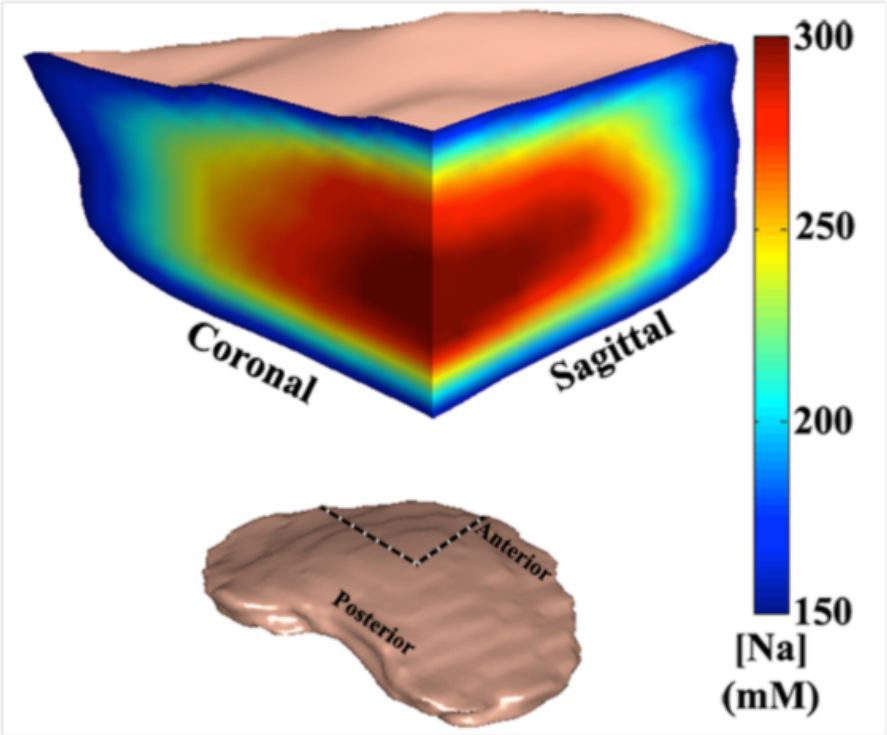

Figure 2-2. A 3D rendered volumetric representation of a disc, followed by an anterior cutaway section depicting both coronal and sagittal [Na^+] variation of the disc. The dashed lines show where the cutaway section was extracted from the whole disc.

A series of axial plane [Na^+] color maps are shown in Figure 2-3. From the [Na^+] maps of the coronal, sagittal and axial planes, the center of the disc NP has an average [Na^+] of approximately 300 mM, while the average [Na^+] falls to approximately 150 mM near the AF.

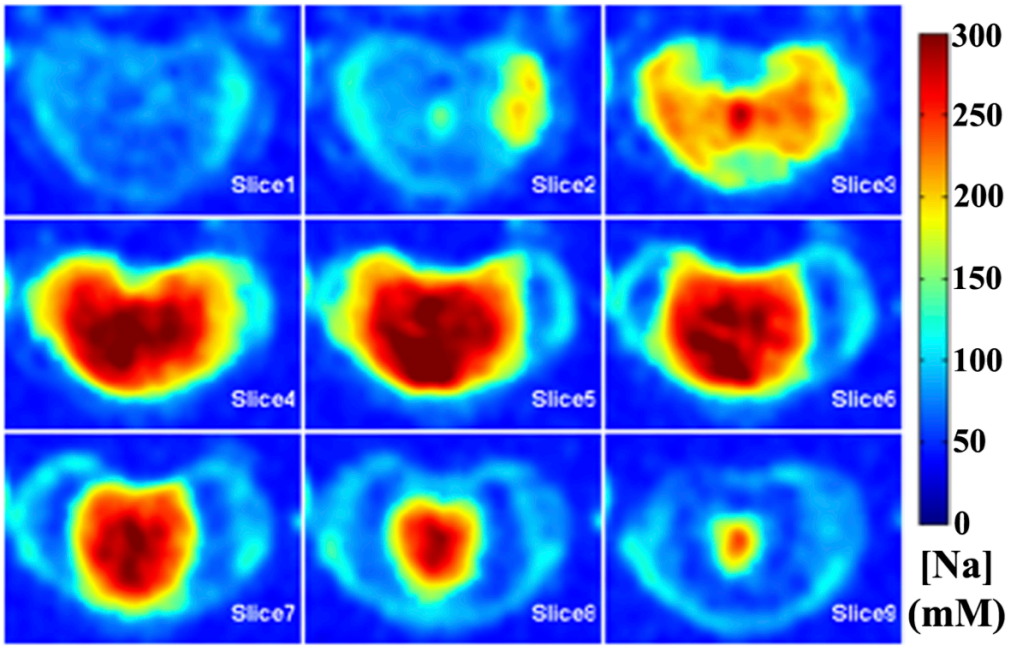

Figure 2-3. A series of consecutive axial [Na^+] maps of a disc. Note the variation of [Na^+] from high values (>300mM) in the NP to <100mM in the AF and this is observed in all three planes.

The axial FCD maps are shown in Figure 2-4, and the FCD maps follow the same trend as the [Na^+] maps, with the center of the NP having the most negative FCD. In the process of FCD calculation according to Equation 2-5, we assumed a serum [Na^+] of 150 mM. Therefore, any tissue with [Na^+] below 150 mM would yield a positive FCD measurement. The apparent voxel dimension in the frequency encoding direction is five time larger than the nominal dimension, as a result of T_2^* decay during signal acquisition. This blurring introduces partial voluming effects to the voxels near the edge of the disc, resulting in [Na^+] measurement of less than 150 mM and corresponding positive FCD values. These voxels were ignored in the FCD map using a simple threshold.

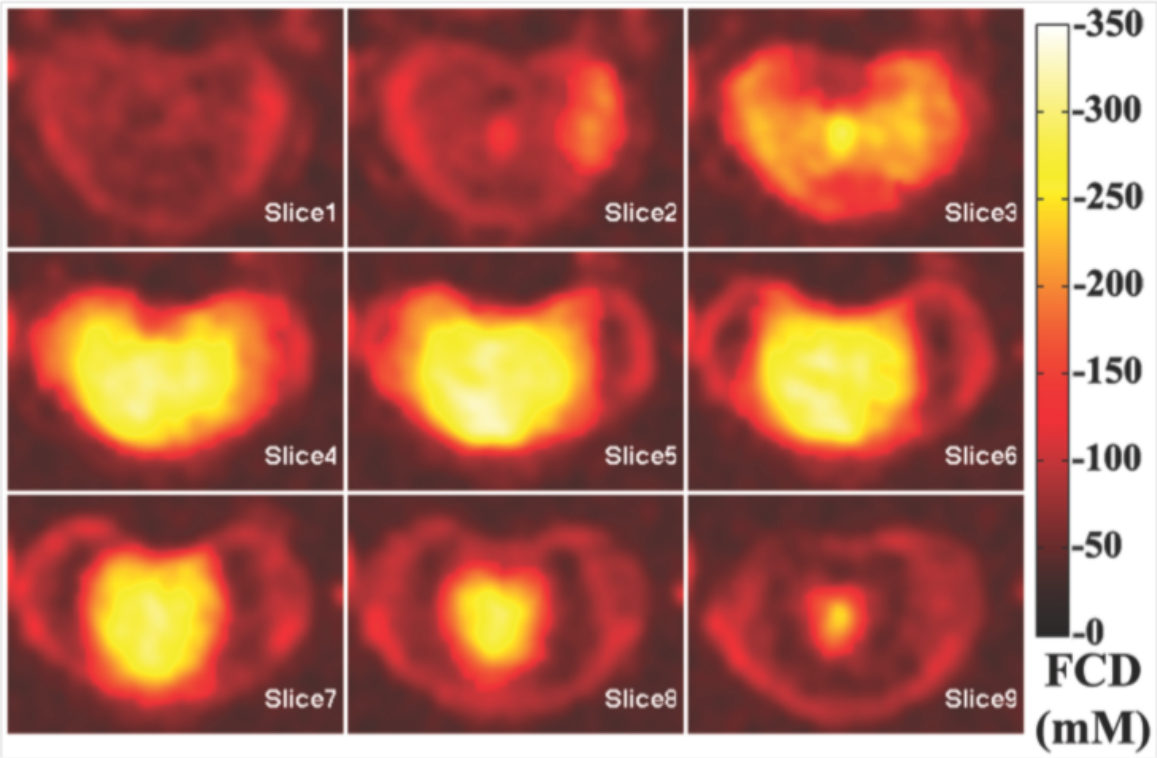

Figure 2-4. A series of consecutive axial FCD maps of the same disc from the previous figure. Note that higher FCD (more negative) is correlated with higher [Na^+], as shown in the previous figure.

A plot (Figure 2-5) of [Na^+] measured by sodium MRI vs. [PG] measured by DMMB assay produced a positive linear trend with a significant correlation coefficient of 0.71. The linear regression analysis was carried out using the [Na^+] and [PG] measurements of 28 NP punch samples, at a significance level of $p<0.05$. Given the sample size and corresponding significance level, the computed correlation coefficient demonstrated a strong linear relationship between IVD NP [Na^+] and [PG] measurements. The linear regression fit's y-intercept of 111.54 mM represents the [Na^+] value at a [PG] value of 0, which corroborates the

result obtained by an earlier biochemical experiment on human cadaveric discs(Urban and Winlove 2007).

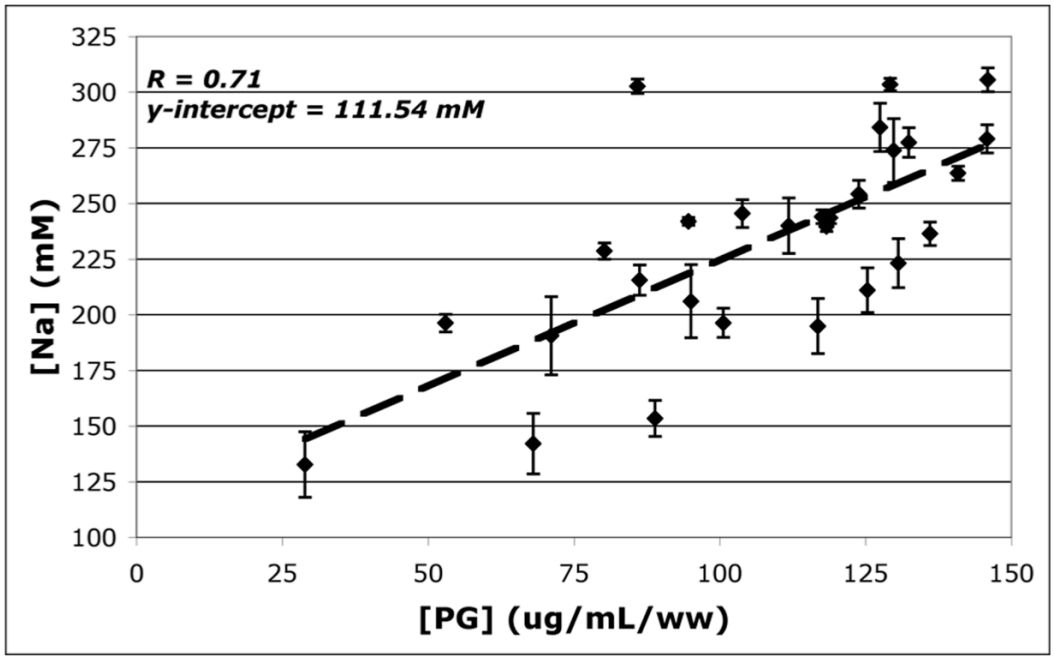

Figure 2-5. Plot of [Na^+] vs. [PG], the standard deviation of each ROI measurement is graphed as the error bar and the unit of [PG] is µg/mL/ww, this concentration was normalized against sample wet weight (ww). The dashed line represents the linear regression fit. The linear regression fit yielded a significant correlation ($r=0.71$ and $p<0.05$).

The average [PG] and [Na^+] profiles in the left-to-right (Figure 2-6A) and anterior-to-posterior (Figure 2-6B) directions are summarized in Figure 2-6. The left-to-right and anterior-to-posterior [PG] profiles exhibit the same trend, with the center of the NP having the highest [PG] and tapering off approaching toward the AF. The [Na^+] profiles in both directions follow closely with the [PG] profiles.

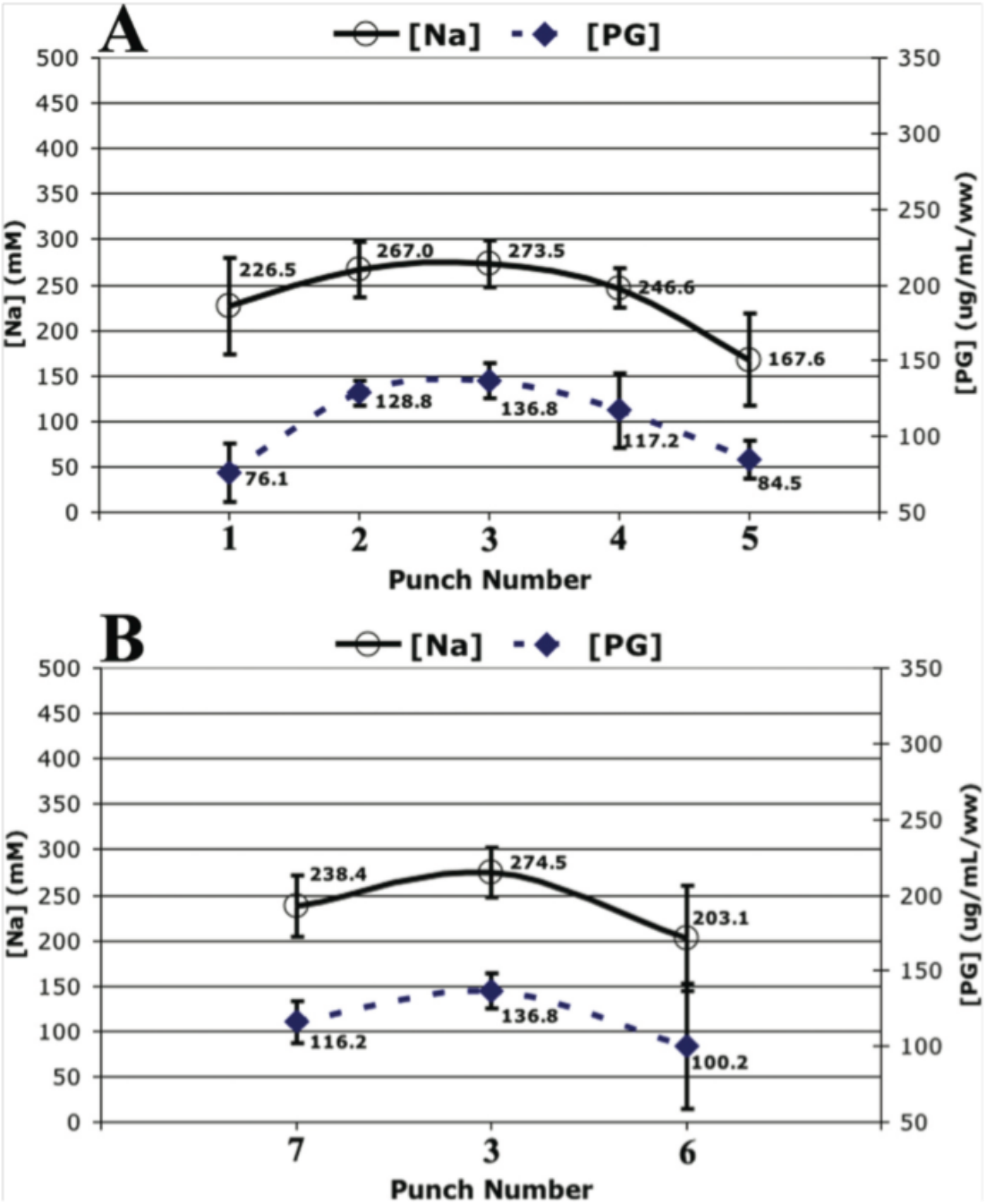

Figure 2-6. The averaged disc zonal profile (averaged across all four discs) of the [Na^+] measured from PG assay and the [Na^+] computed from sodium MRI in A.) the left-to-right direction and B.) the anterior-to-posterior direction. The inter-disc standard deviations are graphed as the error.

The feasibility of using sodium MRI to quantify [Na^+] in a clinical setting is demonstrated in Figure 7. A conventional

clinical T_2-weighted proton MRI of a symptomatic young subject (subject A) exhibits decreased signal in the L5/L4 and L4/L3 discs. In the corresponding $[Na^+]$ maps, the same discs show significantly lower $[Na^+]$ when compared to the normal-appearing discs within the same subject as well as the discs of the asymptomatic subject (subject B).

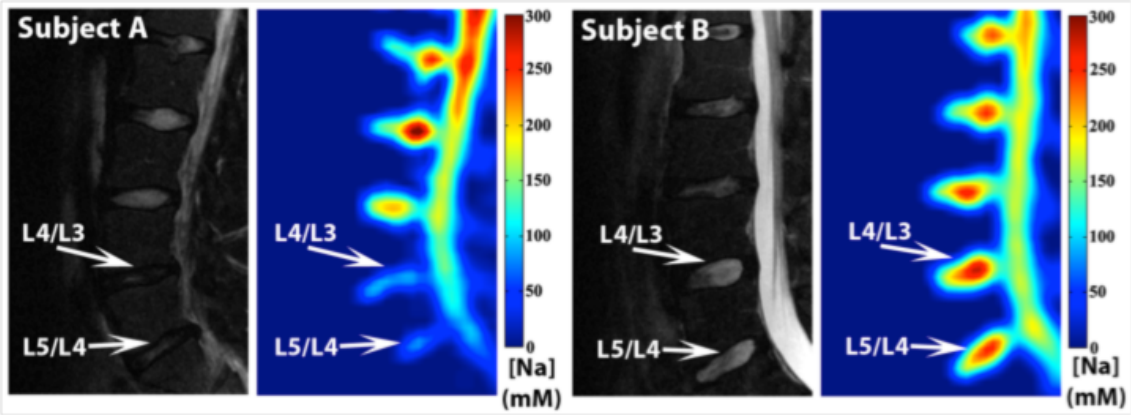

Figure 2-7. Subject A is a 22-year-old subject with a history of lower back trauma. Subject B is a 26-year-old asymptomatic subject. For each subject, the gray-scale T_2-weighted MR image is shown on the left and the colored $[Na^+]$ map is shown on the right.

2.5 Discussion

Variability in disc $[Na^+]$ values was important in determining the relationship between $[Na^+]$ measured from sodium MRI and [PG] measurement from standard DMMB assay in this study. The intrinsic inhomogeneity of $[Na^+]$ distribution within a disc is best demonstrated by the colored $[Na^+]$ maps of Figure 2-2. By removing punches for PG assay and locating the same punches from the $[Na^+]$ maps computed from the sodium MR images, we demonstrated the

feasibility of using sodium MRI to non-invasively assess [PG], as shown by the linear regression fit of [Na^+] vs. [PG] scatter plot in Figure 2-5.

The higher [PG] in the center of NP compared to the periphery NP and the AF was well known, but this trend has never been characterized as shown in Figure 2-6. The averaged disc zonal profile (averaged across all four discs) of the [Na^+] measured from PG assay and the [Na^+] computed from sodium MRI in A.) the left-to-right direction and B.) the anterior-to-posterior direction. The inter-disc standard deviations are graphed as the error. The similar shapes of [PG] and [Na^+] profiles also suggested that sodium MRI can measure [Na^+] and hence [PG], making it possible to extend this sodium MRI based [PG] measurement technique to *in vivo* applications when IVD tissue cannot be extracted for PG assay.

In the *in vivo* experiment, the symptomatic subject (subject A) had two lumbar IVDs with significantly lower [Na^+] (Figure 2-7), which suggests that the PG content of the subject's discs was reduced. While proton T_2 MRI reflects disc tissue hydration, sodium MRI is highly specific to PG content of the tissue. A loss of both water and PG suggests a more advanced stage of disc degeneration and could be the cause of LBP in this individual. The *in vivo* sodium MR images were primarily meant to demonstrate the feasibility of conducting sodium MRI in a clinical setting. Due to the limited sample size as well as the lack of clinical

confirmation, we did not extract any statistically relevant information from the *in vivo* images.

The subjects' FCD maps were not shown in the figure since they mostly demonstrated the same information as the [Na^+] maps. In a simulated experiment, the linear regression fit of FCD versus [Na^+], calculated over a physiological range of [Na^+] from 150 mM to 350 mM, yielded a linear correlation coefficient of 0.998. As a result, FCD can be seen as a linearly scaled version of [Na^+].

Sodium MRI offers specificity in quantifying disc PG content, which is not available in standard proton MRI. Our results suggest that sodium MRI can be used to study disc degeneration and other disc pathologies that are relate to changes in [PG]. However, there are some technical challenges to routine clinical use of sodium MRI such as the inherent low SNR of sodium MRI. Therefore, we had to either sacrifice spatial resolution or increase total MRI scan time in order to boost SNR. In the clinical setting, scan times are often limited to <45 minutes, therefore the spatial resolution of sodium MRI has to be lower than that of conventional proton MRI. Moreover, sodium MRI requires the MRI scanner to be equipped with broadband RF transmitter and receiver, which are not standard to all clinical scanners. Recent advances in parallel imaging techniques and the proliferation of high field MRI (>3T) should alleviate some of the issue with low SNR and may allow greater application of sodium MRI techniques for routine diagnostic imaging.

2.6 Summary

The results of this study demonstrated the feasibility of quantifying disc [Na^+] and thus [PG] using sodium MRI. We found a strong linear correlation between [Na^+] measured by sodium MRI and [PG] determined using DMMB assay. In the *in vivo* section of our experiment, we demonstrated that sodium MRI was able to detect abnormally low disc [Na^+] in a young symptomatic subject. Although we could not verify the clinical significance of the abnormality, however given the subject's age and history of LBP, the low disc [Na^+] may reflect an underlying disc pathology. To the best of our knowledge, this is the first validation of sodium MRI as a method for assessing disc [PG] non-invasively, and thus we demonstrated that sodium MRI has the potential to be used in a clinical setting for diagnosing the depletion of PG typical of the initial stage of disc degeneration.

Chapter 3: Correlation of Intervertebral Disc FCD and $T_{1\rho}$ Relaxation Time Constants

3.1 Synopsis

After validating sodium MRI's role in the quantification of IVD [Na^+] and [PG] in Chapter 2, the aim of this study was to compare $T_{1\rho}$ MRI to sodium MRI, and to demonstrate $T_{1\rho}$ MRI's capability for measuring IVD osmotic pressure. Self-coregistered sodium and $T_{1\rho}$-weighted MR images were acquired on *ex vivo* bovine IVDs (N = 12) on a 3 T clinical MRI scanner. The sodium MR images were used to calculate effective NP FCD (mean = 138.2±27.6 mM) and subsequently osmotic pressure (mean = 0.53±0.18 atm), while the $T_{1\rho}$-weighted images were used to compute $T_{1\rho}$ relaxation maps. A significant linear correlation ($R=0.56$, $p<0.01$) between NP FCD and $T_{1\rho}$ relaxation time constant was observed. More importantly, a significant power correlation ($R=0.72$, $p<0.01$) between NP osmotic pressure as predicted by sodium MRI and $T_{1\rho}$ relaxation time constant was also observed. The current clinical method for assessing disc pressure is discography, which is an invasive procedure that has been shown to have negative effects on disc biomechanical and biochemical properties. In contrast, $T_{1\rho}$ MRI is non-invasive and can be easily implemented in a clinical setting due to its superior SNR compared to sodium MRI. Therefore, $T_{1\rho}$ MRI may serve as a non-invasive clinical tool for the longitudinal evaluation of IVD osmotic pressure.

3.2 Introduction

In a recent study, sodium MRI was validated as a method for [PG] quantification in bovine IVDs(Wang et al. 2010). While sodium is specific to [PG], it has certain disadvantages compared to conventional proton MRI. The SNR of sodium MRI is significantly lower than proton MRI. This disadvantage limits sodium MRI's role in *in vivo* applications. In order to compensate for the low SNR of sodium MRI, sodium MRI often requires significantly increased scan time for signal averaging. Recent studies on $T_{1\rho}$ MRI have demonstrated its great potential for non-invasive evaluation of [PG] in articular cartilage and in IVD(Wheaton et al. 2005, Akella et al. 2001, Auerbach et al. 2006). $T_{1\rho}$ MRI can be implemented as a spin-locking RF pulse cluster on most MRI scanners without hardware modification. The spin-lock preparation pulse cluster refocuses relaxation of the transverse magnetization resulting from slow molecular interaction(Wheaton et al. 2005), which imparts the MR image with a contrast that is sensitive to the breakdown and depletion of PG. Since $T_{1\rho}$ MRI targets proton nuclei as conventional MRI, it has significantly higher SNR efficiency than sodium MRI, which makes $T_{1\rho}$ MRI a more clinically viable technique.

In order to validate $T_{1\rho}$ MRI as a SNR efficient and accurate method of measuring IVD [PG], we need to compare $T_{1\rho}$ MRI of IVD with sodium MRI of IVD. The correlation between $T_{1\rho}$ MRI and sodium

MRI can be computed from coregistered IVD $T_{1\rho}$ and sodium MR images, where the $T_{1\rho}$ and [Na^+] values can be compared on a pixel-by-pixel basis. Due to its SNR and clinically applicability advantages over sodium MRI, $T_{1\rho}$-MRI can be applied in a clinical setting to detect early stage IVD degeneration and monitor its progression. Moreover, it has been demonstrated that osmotic pressure can be calculated using FCD measurement in articular cartilage(Urban et al. 1979). Since FCD measurement can be calculated from sodium MRI(Shapiro et al. 2002), sodium MRI can be used to non-invasively measure tissue osmotic pressure. In this study, we also correlated $T_{1\rho}$ with osmotic pressure measurements calculated using sodium MRI. In doing so, we determined the relationship between $T_{1\rho}$ value and IVD osmotic pressure. The current clinical procedure for assessing IVD pressure is discography, which is a costly and painful procedure. In addition, discography has potential negative side effects that may warrant additional scrutiny. Previous studies have shown that the needle puncture injury caused by discography has both immediate and progressive mechanical and biological consequences on the IVD (Korecki et al. 2008). In comparison, $T_{1\rho}$ MRI is completely non-invasive by nature and has been shown to correlate well with [PG], therefore a positive correlation between $T_{1\rho}$ value and osmotic pressure will make $T_{1\rho}$ MRI a potential clinical alternative to discography. In this study, we demonstrated $T_{1\rho}$ MRI's clinical significance as a potential non-invasive diagnostic tool for IVD osmotic pressure by establishing a

correlation between $T_{1\rho}$ relaxation time constant and osmotic pressure measured via sodium MRI.

3.3 Methods

3.3.1 Bovine Specimen

Four fresh whole bovine lumbar spines were obtained from a local abattoir (Bierig Brothers, Vineland NJ), within a few hours of slaughter. The last three caudal IVDs of each spine sample were surgically removed. The vertebral body on each side of the IVD specimen was trimmed with a bone saw to include the endplate and approximately 1 cm of bony tissue, thus each processed IVD specimen contained a single IVD sandwiched between vertebral endplates, preserving the integrity of the motion segment. Next, the specimens were secured to a custom-made platform attached to the scanner bed, as shown in Figure 3-1.

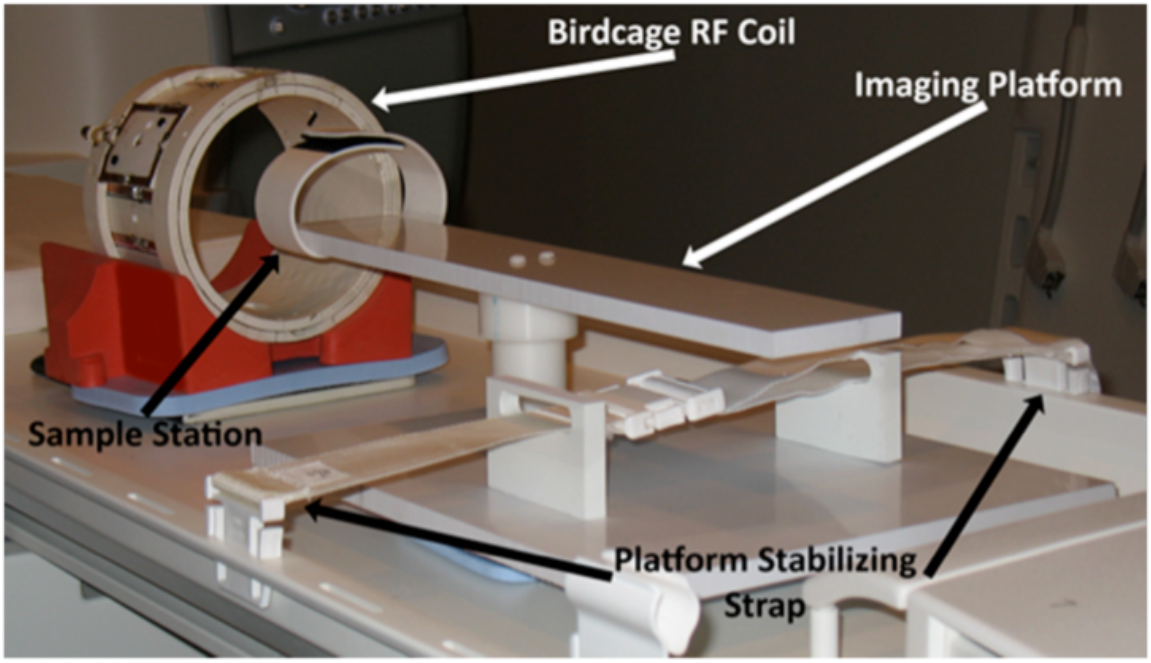

Figure 3-1. Diagram of the imaging platform used for the self-coregistered sodium and $T_{1\rho}$ MRI. The body of the platform is secured onto the MRI scanner bed using a strap. The IVDs samples are placed at the sample station at the end of imaging platform, where a Velcro strap firmly secures the IVD sample to the imaging platform. The sodium and proton birdcage RF coils can then be slipped over the IVD sample in succession, without disturbing the sample itself. Additional sandbags are placed at the base of the imaging platform to further dampen vibrations contributed by gradient activity during the imaging sessions.

This platform allowed for the interchange of a pair of sodium and proton radiofrequency (RF) coils while the sample remained stationary inside the scanner bore. As a result, the same FOV was preserved between the proton and sodium MR scans, which allowed for the pixel-to-pixel quantitative comparison of sodium and proton MR images.

3.3.2 Sodium Magnetic Resonance Imaging Protocol

Both sodium and $T_{1\rho}$-weighted MRI were performed on a 3 T Siemens Trio MRI scanner (Siemens Medical Solutions, Erlangen, Germany) equipped with a broadband transmitter and receiver at the Hospital of the University of Pennsylvania. All experimental procedures were in accordance with IACUC regulations at our institution. First the custom-made sodium low-pass quadrature birdcage RF coil (ω_o = 32.6 MHz) was slipped over the previously mentioned imaging platform. The sodium RF coil was 17 cm in diameter and 12.5 cm long, containing 16 struts. Its two receiver ports were inductively coupled to the coil and spatially oriented 90° relative to each other. Five 10% agarose gel phantoms containing 300 mM, 250 mM, 200 mM, 150 mM, and 100 mM Na^+ were imaged alongside each specimen for eventual [Na^+] calibration (Figure 3-2).

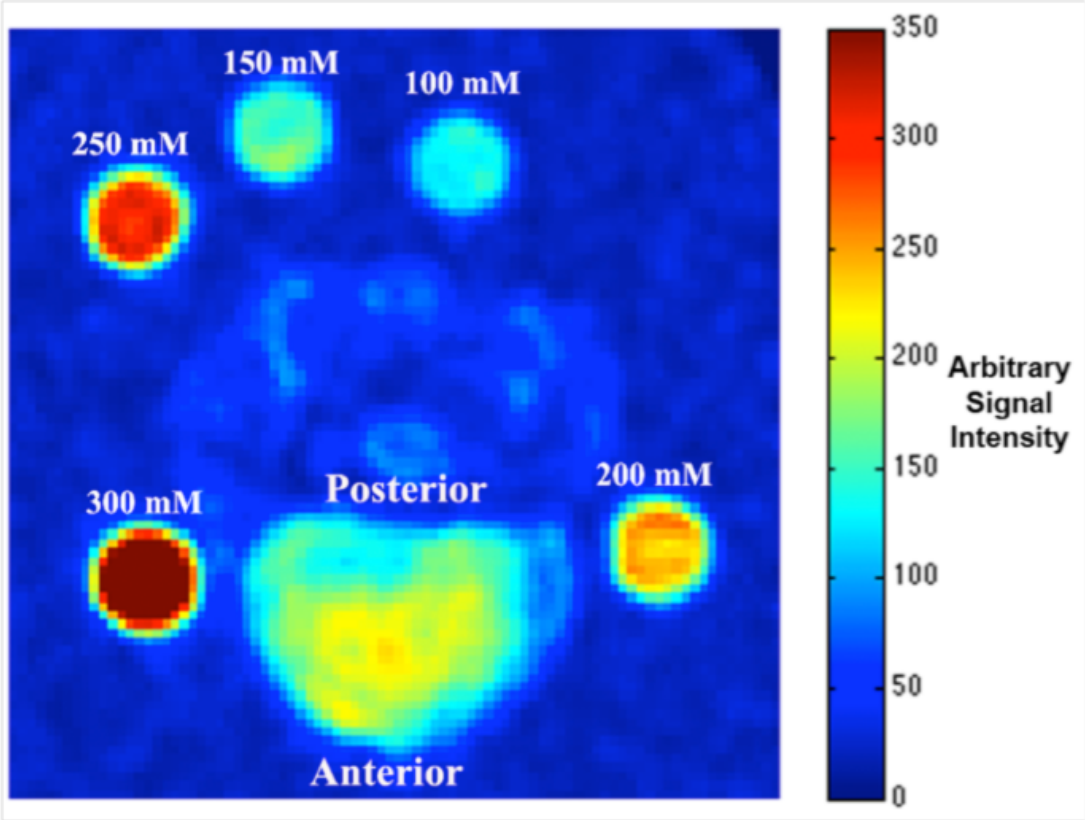

Figure 3-2. An axial plane sodium image of a representative IVD, surrounded by five sodium phantoms containing different concentration of sodium.

A standard gradient-echo pulse sequence was used to acquire all sodium images. A low-resolution sodium image was acquired prior to the actual 3D sodium MR image acquisition in order to localize the desired FOV. The 3D imaging parameters were as follows: TE/TR = 6/30 ms, Ernst angle = 75.2°, FOV = 15 x 15 cm, matrix size = 128 x 128, slices = 128, slice thickness = 1.2 mm, BW = 60 Hz/Pixel, signal average = 75, imaging time = 10 hours and 14 minutes. Sodium nuclei exhibit biexponential T_2* decay, with both a short and a long T_2* component. However, the relatively long TE in this protocol minimized signal contribution from sodium's

short T_2* component. Thus the sodium signal measured in this study can be approximately modeled as a single exponential. In addition, the broadening of the point-spread-function is minimized by not acquiring sodium signal undergoing the short T_2* relaxation. The small acquisition BW was chosen to maximize the image SNR. The above parameters were chosen to obtain a minimum SNR of 15:1 for an isotropic voxel size of 1.2 mm^3. $T_{1\rho}$ MRI was carried out immediately after sodium MRI during the same imaging session.

3.3.3 Mapping [Na^+] in Bovine Intervertebral Disc

The sodium MR images were first smoothed using a 3x3x3 pixel boxcar filter. Next, the pixel-wise [Na^+] computation based on sodium phantom signals was carried out according to the method described by Shapiro *et al.*(Shapiro et al. 2002). The sodium signals from the sample and the phantoms were corrected separately for T_1 and T_2^* decays according to Equation 3-1.

$$S_{corrected} = \frac{\sin(FA)\cdot\left(1-e^{-TR/T_1}\right)\cdot e^{-TE/T_2^*}}{1-\cos(FA)\cdot e^{-TR/T_1}}\cdot S_o \qquad \text{Equation 3-1}$$

In Equation 3-1, θ is the flip angle and S_o is the thermal equilibrium magnetization. Sodium T_1 and T_2^* of the IVD and phantoms were computed using progressive saturation experiments, yielding T_1 relaxation time constants of 22 ms and 23 ms for the IVD and phantoms, respectively. The T_2^* of the IVD and phantoms

were determined by varying the TE parameter, yielding T_2* relaxation time constants of 16 ms and 8 ms for IVD and phantoms, respectively. After compensating for T_1 and T_2^* relaxation, the average sodium signal from each phantom of known $[Na^+]$ was plotted on a calibration curve of $[Na^+]$ versus sodium signal. The slope and y-intercept of the linear fit of the calibration curve was then used to compute a 3D $[Na^+]$ map of the IVD.

3.3.4 Calculating Bovine Intervertebral Disc FCD and Osmotic Pressure

FCD can be directly calculated form tissue $[Na^+]$ measurement ($[Na^+]_t$) and surrounding fluid $[Na^+]$ measurement ($[Na^+]_f$) using a method developed by Lesperance *et al.*(Lesperance et al. 1992). The expression that relates FCD to $[Na^+]_t$ and $[Na^+]_f$ is shown in Equation 3-2.

$$FCD = \frac{\left[Na^+\right]_f^2}{\left[Na^+\right]_t} - \left[Na^+\right]_t \qquad \text{Equation 3-2}$$

In the context of this study, the FCD is computed using a $[Na^+]_f$ value of 150 mM, which is the normal $[Na^+]$ level in serum fluid. Osmotic pressure was subsequently calculated from an expression empirically derived by Urban *et al.*(Urban et al. 1979). However, the FCD value computed according to Equation 3-2 is an average FCD measurement based on the total NP extracellular sodium. The NP extracellular sodium is in fact composed of both

intrafibrillar (relative to the NP type II collagen fibers) and extrafibrillar water compartments. Intrafibrillar water resides in the space within the collagen fibrils, thus the PGs are excluded from the intrafibrillar volume due to their large size(Maroudas 1990). Instead, the PGs are confined within the extrafibrillar water, where they attract the positively charged Na^+ ions to generate the osmotic pressure necessary to resist loads. Therefore, the effective calculation of FCD should reflect the compartmentalization of Na^+ ions to the smaller volume of the extrafibrillar water. In fact, the effective FCD ($FCD_{effective}$) is always higher than the FCD value calculated from Equation 3-2, assuming that the extrafibrillar water is always less than the total water content of the IVD NP tissue. With the knowledge of $FCD_{effective}$, the actual osmotic pressure of the IVD can be accurately calculated according to Equation 3-3(Maroudas 1990).

$$P = B \cdot \left(FCD_{effective}\right)^2 \qquad \text{Equation 3-3}$$

In Equation 3-3, P is the osmotic pressure in unit of atm, B is a constant of 26.6 atm/M^2, and $FCD_{effective}$ is the FCD specific to NP extrafibrillar water. In order to compute $FCD_{effective}$ from FCD calculated directly from sodium MRI, the relative fractions of intrafibrillar and extrafibrillar water compartments in the NP need to be determined first. The relationship between FCD and $FCD_{effective}$ is defined in Equation 3-4(Maroudas 1990).

$$FCD_{effective} = FCD \cdot \frac{W_{total}}{W_{water} - W_{\text{intrafibrillar}}} \qquad \text{Equation 3-4}$$

In Equation 3-4, the FCD value calculated using Equation 3-2 is compensated by the ratio of the tissue's total wet weight (W_{total}) and the weight of the extrafibrillar water, which is defined as the subtraction of the total water weight (W_{water}) by the intrafibrillar water weight ($W_{intrafibrillar}$). Since $W_{intrafibrillar}$ is not easily measured directly, it is expanded from Equation 3-4 to form Equation 3-5(Maroudas 1990).

$$FCD_{effective} = FCD \times \frac{W_{total}}{W_{water} - W_{total} \times \overline{W}_{\text{collagen}} \times \overline{W}_{\text{intrafibrillar}}} \qquad \text{Equation 3-5}$$

In Equation 3-5, the $W_{intrafibrillar}$ term from Equation 3-4 is expanded as the product of W_{total}, $\overline{W}_{collagen}$ (dry weight of collagen normalized against W_{total}) and $\overline{W}_{\text{intrafibrillar}}$ (weight of intrafibrillar water normalized per dry weight of collagen). A previous study has concluded that water content constitutes 80% of a healthy adult's IVD NP(Antoniou et al. 1996). Therefore, W_{water} equals to 0.8 after normalizing it against W_{total}. NP collagen amounts to 20% of the dry weight of the NP tissue(Eyre and Muir 1977), which yields 0.04 for $\overline{W}_{collagen}$. At last, $\overline{W}_{\text{intrafibrillar}}$ for a healthy adult has been shown to be 0.98 g water/g collagen(Sivan et al. 2006). Substituting these values back in Equation 3-5 and Equation 3-3 results in the final expression that relates osmotic pressure

measurement to the FCD values measured from sodium MRI directly, as shown in Equation 3-6.

$$P = B \cdot (1.314 \cdot FCD)^2 \qquad \text{Equation 3-6}$$

Equation 3-6 takes into account the contribution of intrafibrillar water to the total water volume in IVD NP.

3.3.5 Mapping $T_{1\rho}$ Relaxation Rate in Bovine Intervertebral Discs

Following the sodium MR scan, the sodium coil was removed and a Siemens 8-channel proton birdcage RF coil was slipped over the imaging platform. $T_{1\rho}$ MRI was carried out using a custom spin-lock prepared 3D SPGR pulse sequence. The FOV and resolution parameters were identical to those of the sodium MRI. The imaging parameters were as follows: TE/TR = 4.5/120 ms, FOV = 15x15 cm, matrix size = 128x128, slices = 64, slice thickness = 1.2 mm. Spin-lock preparation was applied once for every 16 phase-encodes, and the phase-encoding was centrically ordered to preserve $T_{1\rho}$ weighting in the center of the k-space. $T_{1\rho}$-weighted images at four spin-locking times (TSL = 10, 20, 30, 40 ms) were collected, with the spin-lock amplitude set at 500 Hz, for a total imaging time of 1 hour and 20 minutes. The highest TSL of 40 ms was limited by the RF specific absorption rate (SAR) restriction on the clinical MRI scanner used. The FOV center and spatial resolution of the $T_{1\rho}$ scans were copied directly from the previous sodium MRI scans, thus the pixel-to-pixel coregistration

between the sodium and $T_{1\rho}$ MR scans was maintained. A $T_{1\rho}$ map was computed on a pixel-by-pixel basis from the four $T_{1\rho}$-weighted images according to Equation 3-7.

$$S = S_o \cdot e^{-TSL/T_{1\rho}} \qquad \text{Equation 3-7}$$

In Equation 3-7, S is the image signal intensity and S_o is the intensity of the thermal equilibrium magnetization.

3.3.6 Image Processing and Data Analysis for Bovine IVD

All sodium $T_{1\rho}$-weighted MR images were transferred to a Macbook Pro computer (Apple, Cupertino, CA) for processing and ROI analysis, which were carried out using custom algorithms developed with MATLAB software (Mathworks, Natick, MA). For each IVD, a single user (CW) chose a 4 mm diameter circular ROI on three mid-axial slices in a $T_{1\rho}$-weighted image. The ROIs were then used to extract average $[Na^+]$ and $T_{1\rho}$ relaxation time constant values from the self-coregistered $[Na^+]$ and $T_{1\rho}$ maps. The average ROI $FCD_{effective}$ and osmotic pressure measurements were computed from $[Na^+]$ using Equation 3-5 and Equation 3-6 accordingly.

3.3.7 Statistical Analysis

Linear regression analysis was applied to the $T_{1\rho}$ relaxation time constant versus $FCD_{effective}$ data. Bivariate correlation of the same data pairs was also carried out, and Pearson correlation

coefficient and Spearman's rank correlation coefficient were computed to determine if there was a direct linear relationship between $T_{1\rho}$ relaxation time constant and $FCD_{effective}$ in the NP regions of the IVDs. Regression analysis was applied to the $T_{1\rho}$ relaxation time constant versus osmotic pressure data. However, due to the non-linear relationship between $FCD_{effective}$ and osmotic pressure as shown in Equation 3-6, a power regression analysis was applied to the $T_{1\rho}$ relaxation time constant versus osmotic pressure data instead of a linear regression analysis. Both the bivariate correlation analysis between $T_{1\rho}$ relaxation time constant and $FCD_{effective}$ measurements, and the power regression analysis between $T_{1\rho}$ relaxation time constant and osmotic pressure data were carried out at a significance level of $p<0.01$.

3.4 Results

Figure 3-3 illustrates a series of four consecutive axial slices of an IVD [Na^+] color map overlaid on top of the corresponding grayscale anatomical images.

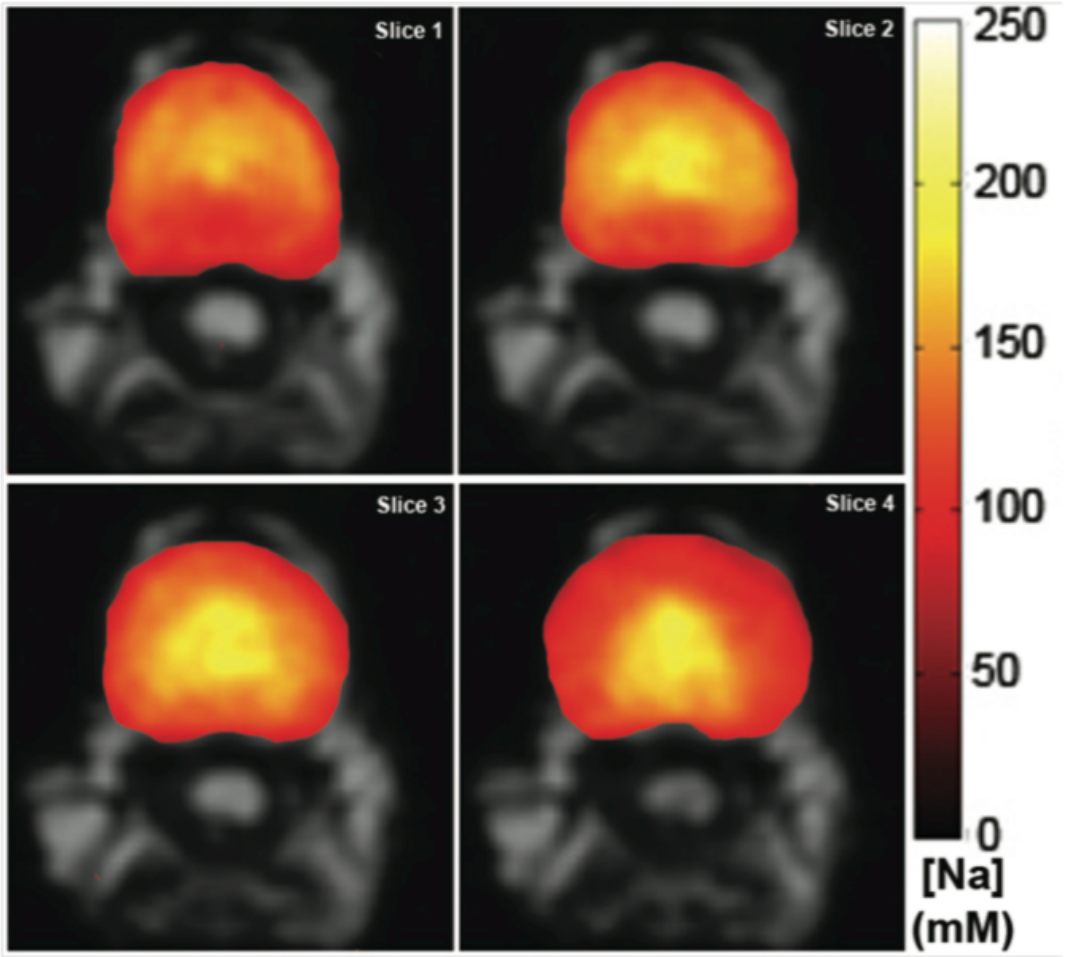

Figure 3-3. Four consecutive axial slices of an IVD's [Na^+] map. Note the decrease in [Na^+] going from the center of the NP toward the AF. Ventral side of the IVD faces up.

The center of the IVD typically has the highest [Na^+] value at around roughly 250 mM. Since the NP contains the majority of the PGs in the IVD, the regions of high [Na^+] represent the NP region. In contrast, the peripheries of the IVD [Na^+] maps in Figure 3-3 indicate a much lower [Na^+] at around 150 mM, which is close to the theoretical serum fluid level [Na^+]. The peripheries of the IVD [Na^+] maps represent the AF region with lower [Na^+], due to the lack of PGs.

Figure 3-4 illustrates four consecutive axial slice $T_{1\rho}$ maps of the same IVD for which its $[Na^+]$ maps are shown in Figure 3-3.

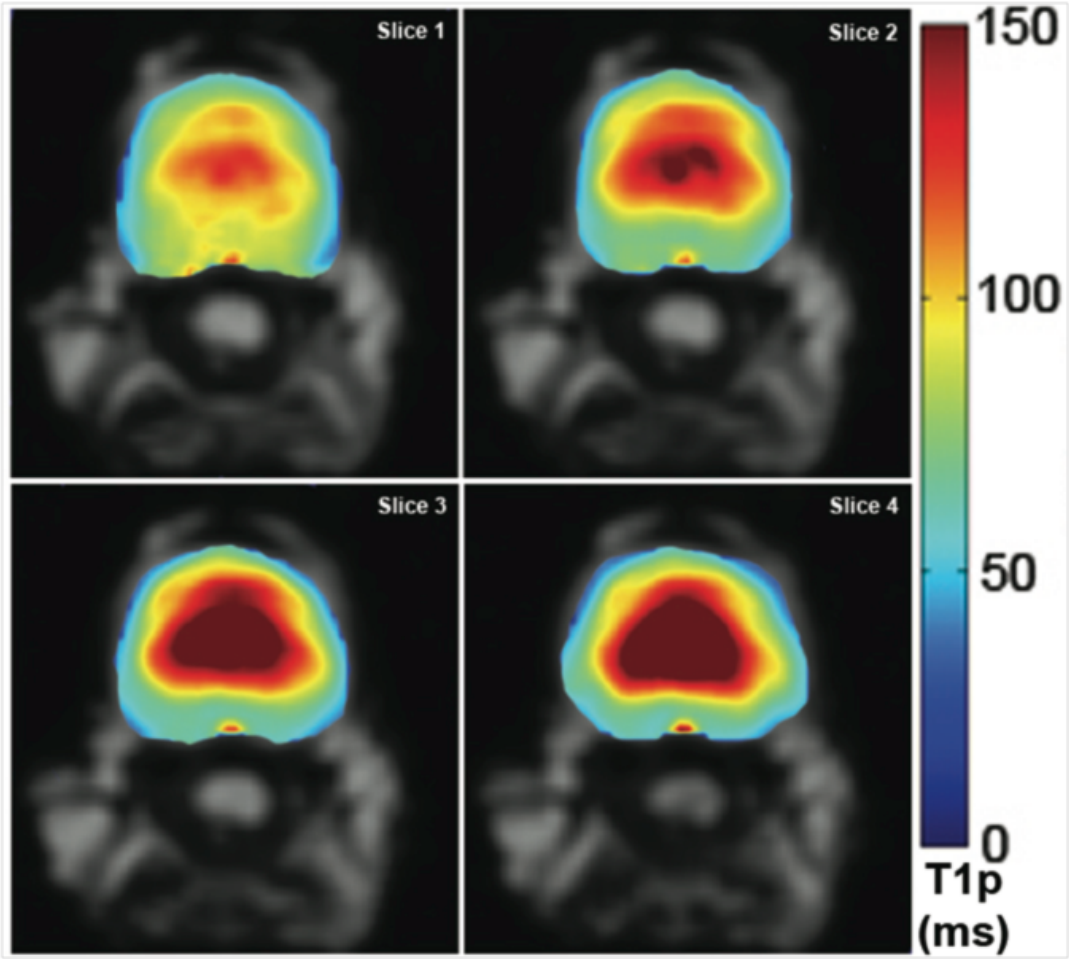

Figure 3-4. Four consecutive axial slices of an IVD's $T_{1\rho}$ map. Note the decrease in $T_{1\rho}$ going from the center of the NP toward the AF. Ventral side of the IVD faces up.

As in the case of the $[Na^+]$ maps, $T_{1\rho}$ appear to be the highest in the center of the IVD, where the PG-rich NP is located. In the IVD peripheries composed of the AF, $T_{1\rho}$ decreased to approximately 30% of the maximum value observed in the center of the NP. In addition, the $T_{1\rho}$ map in Figure 3-4 exhibits superior spatial

resolution when compared to the corresponding [Na^+] map in Figure 3-3, which has a blurry appearance.

ROI analysis of the NP [Na^+] maps and the NP $T_{1\rho}$ maps yielded average $FCD_{effective}$ (from Equation 3-5), osmotic pressure (from Equation 3-6), and $T_{1\rho}$ relaxation time constant. $T_{1\rho}$ relaxation time constants were separately compared to first the $FCD_{effective}$ values and then to the osmotic pressure values. Figure 3-5(A) contains the scatter plot of average NP $FCD_{effective}$ versus $T_{1\rho}$ relaxation time constant.

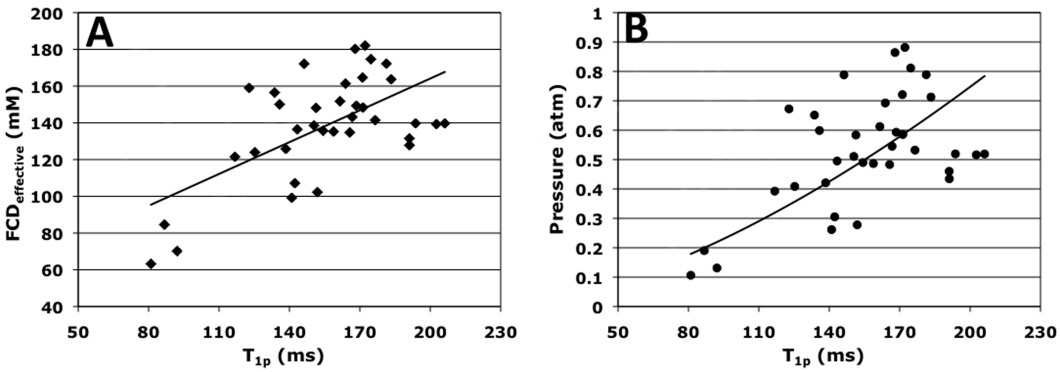

Figure 3-5. (A) A plot of IVD NP $FCD_{effective}$ measurement vs. the corresponding $T_{1\rho}$ relaxation time constant. The solid line represents the linear regression line of the scatter plot, with a correlation coefficient of 0.56 at $p<0.01$. (B) A plot of IVD NP osmotic pressure measurement vs. the $T_{1\rho}$ relaxation time constant. A power regression fit was applied to the scatter plot, yielding a correlation coefficient of 0.72 at $p<0.01$.

The solid line marks the linear regression fit of the data points, and it shows a positive relationship between NP $FCD_{effective}$ and $T_{1\rho}$ relaxation time constant. A one-tailed bivariate correlation analysis of the $FCD_{effective}$ versus $T_{1\rho}$ data yielded a significant Pearson correlation coefficient of 0.56 with $p<0.01$,

as well as a significant Spearman's rank correlation coefficient of 0.44 with $p<0.01$. Due to the squared relationship between $FCD_{effective}$ and osmotic pressure as shown in Equation 3-6, a power regression analysis was applied to the osmotic pressure versus $T_{1\rho}$ relaxation time constant scatter plot in Figure 3-5(B), resulting in the expression relating NP $T_{1\rho}$ relaxation time constant in unit of ms to IVD osmotic pressure in unit of atm, as shown in Equation 3-8.

$$\text{Pressure} = \left(\frac{T_{1\rho}}{1000}\right)^{1.6} \qquad \text{Equation 3-8}$$

Equation 3-8 was obtained with a significant correlation coefficient of 0.72 at $p<0.01$. Note that $T_{1\rho}$ was raised to the power of 1.6 in Equation 3-8, in contrast to the power of 2 for the $FCD_{effective}$ variable in Equation 3-6.

3.5 Discussion

The high $[Na^+]$ in IVD NP compared to the lower $[Na^+]$ in IVD AF observed from the colored $[Na^+]$ maps in Figure 3-3 is consistent with a previous study that measured IVD $[Na^+]$ directly and demonstrated significantly lower sodium content in the AF compared to the NP(Urban and Winlove 2007). In a similar fashion, the observation of elevated $T_{1\rho}$ relaxation time constant in the IVD NP and a much lower $T_{1\rho}$ in the IVD AF supports previous

studies that concluded a positive relationship between IVD [PG] and $T_{1\rho}$ relaxation time constant(Wang et al. 2007, Auerbach et al. 2006). In contrast to IVDs, articular cartilage have been shown to exhibit a negative relationship between [PG] and $T_{1\rho}$ relaxation time constant(Regatte et al. 2002, Wheaton et al. 2005, Li et al. 2007). This opposite trend of $T_{1\rho}$ in articular cartilage and IVD degenerations may be due to their different possible mechanisms of degeneration. In articular cartilage degeneration, PGs leave the type II collagen matrix, and the vacated space may be infiltrated by synovial fluid, resulting in elevated $T_{1\rho}$ relaxation time constant. In contrast, depleted IVD NP PG may be replaced by collagen instead of fluid, which could account for the decreased $T_{1\rho}$ relaxation time constant typically observed in degenerated IVDs.

The quadrupolar nature of sodium results in a biexponential T_2* relaxation when the rotational correlation time of sodium is long enough to not satisfy the extreme narrowing condition(Pekar and Leigh 1986). The IVD NP sodium reside in a motion-restricted macromolecular environment composed of cross-linked type II collagen fibers, which results in an increase in sodium's rotational correlation time. Therefore, the same IVD NP sodium undergoes both short and long T_2* relaxations simultaneously. Thus the sodium signal undergoing long T_2* relaxation can be used to quantify total sodium content, by comparing it to sodium signal from sodium phantoms of known concentrations. This

technique has been previously demonstrated by a sodium MRI study of articular cartilage, which confirmed that the FCD value computed from sodium images acquired at long TE correlated strongly with FCD value obtained from DMMB PG assay(Shapiro et al. 2002).

Moreover, FCD has been previously used to calculate the osmotic pressure of IVD and articular cartilage(Urban et al. 1979). However, the FCD value obtained from [Na^+] measured using sodium MRI is in fact a spatially averaged value taking into account both the extrafibrillar and intrafibrillar compartments of the IVD NP. Since the PGs responsible for generating IVD osmotic pressure are restricted to the extrafibrillar space due to their large size, the FCD calculated according to the expression (Equation 3-2) developed by Lesperance *et al.* in theory would result in an underestimation of the effective FCD ($FCD_{effective}$) and subsequently an underestimation of the IVD osmotic pressure. In order to address this issue, we determined the relationship between $FCD_{effective}$ and the FCD value calculated from sodium MRI using literature values of IVD NP intrafibrillar water content and collagen content. The expression of this relationship (Equation 3-6) was then utilized in the calculation of IVD osmotic pressure. As a result, we demonstrated that the FCD measurement computed using sodium MRI also offers a potentially useful tool for the non-invasive quantification of IVD osmotic pressure.

Despite sodium MRI's promising capability in monitoring IVD NP $FCD_{effective}$ and IVD osmotic pressure, it has inherently low SNR. Thus, the spatial resolution of the sodium MR scan is often lowered in combination with increased scanning time in order to compensate for its low SNR. Together both the long scanning time and low spatial resolution limit the clinical applicability of sodium MRI.

In comparison to sodium MRI, $T_{1\rho}$ MRI yields significantly higher SNR because it targets proton nuclear spin. Moreover, $T_{1\rho}$ contrast is sensitive to the interactions between protons on PG and free water protons, due to its ability to refocus spin dephasing caused by the residual dipolar interaction between collagen protons and free water protons. A previous *ex vivo* IVD study has demonstrated a strong correlation between IVD PG content and $T_{1\rho}$ relaxation(Auerbach et al. 2006). However, to the best of our knowledge, there has been no previous attempt to use non-invasive MRI techniques such as sodium MRI and $T_{1\rho}$ MRI to compute IVD osmotic pressure in intact IVD specimens.

From the results of our regression and bivariate correlation analyses between $T_{1\rho}$ relaxation time constant value, $FCD_{effective}$, and osmotic pressure, we concluded that $T_{1\rho}$ not only linearly correlated with $FCD_{effective}$, but also correlated with osmotic pressure measurements, which has been shown to be linearly correlated with the hydrostatic pressure produced by IVDs under normal loading conditions(Jayson 1976). The power regression

analysis of $T_{1\rho}$ relaxation time constant and osmotic pressure yielded Equation 3-8, which showed that the osmotic pressure measurement was related to $T_{1\rho}$ raised to the power of approximately 1.6. Note in Equation 3-6, the $FCD_{effective}$ variable was raised to the power of 2 for the calculation of osmotic pressure. Assuming a linear relationship between $T_{1\rho}$ relaxation time constant and $FCD_{effective}$, as demonstrated by the significant Pearson and Spearman's correlation coefficients of the bivariate analysis, the discrepancy between Equation 3-8 and Equation 3-6 might be attributed by the fact that Equation 3-6 was derived from an experiment conducted at 4 °C(Urban et al. 1979), which is significantly lower than both the body temperature as well as the room temperature at our imaging facility.

3.6 Summary

In this study, we refined a mathematical model that enables the calculation of IVD osmotic pressure from FCD value computed from sodium MRI. Then we demonstrated that $T_{1\rho}$ MRI of IVD correlates well with $FCD_{effective}$ and osmotic pressure measurements obtained from sodium MRI. Due to its non-invasive nature and high SNR efficiency, $T_{1\rho}$ MRI can potentially be readily applied in clinical setting. Therefore, we have shown that $T_{1\rho}$ MRI has significant potential as a non-invasive clinical tool for the evaluation of IVD osmotic pressure.

Chapter 4: Magnetization Transfer Ratio Mapping of Intervertebral Disc *in vivo*

4.1 Synopsis

Both Chapter 2 and Chapter 3 have been concerned with the fate of PG in IVD degeneration, the aim of this study is to investigate the role of collagen in IVD degeneration using MTR mapping. The MTR of the lumbar IVDs was spatially quantified from age-matched subjects and correlated with Pfirrmann grades determined from T_2-weighted images. A moderate and significant linear correlation between MTR and Pfirrmann grade was observed, suggesting that NP collagen relative density increases with degeneration. High-resolution axial MTR maps revealed elevated MTR in the NP of injured and heavily degenerated IVDs. In the injured IVDs, significant elevation in NP MTR was not always accompanied by significant decrease in disc height. This observation may suggest a possible increase in absolute collagen content, in addition to increased collagen relative density. Therefore, MT MRI of the IVD may serve as a non-invasive diagnostic tool for disc degeneration, in addition to other MRI techniques specific for PG content.

4.2 Introduction

Previous studies have utilized non-invasive PG-sensitive techniques such as sodium MRI and $T_{1\rho}$ MRI to study PG depletion in the NP of degenerated IVDs(Auerbach et al. 2006, Insko et al. 2002). However, these studies did not investigate the degenerative changes in IVD collagen, which is the main macromolecular component of the IVD(Comper 1996a), constituting 70% of the AF's dry weight and 20% of the NP's dry weight(Eyre and Muir 1977).

Both collagen type I and type II fibers contain significant amount of collagen-bound water protons with restricted motion. However, the signal from these protons are difficult to detect due to their rapid spin-spin relaxation mediated by their averaged static dipolar interaction and rotationally modulated dipolar interaction. Thus, conventional MRI techniques such as T_1 and T_2-weighted imaging with conventional TE times are insensitive to proton signals from the AF, which makes the visualization and signal quantification of the AF difficult.

Although collagen-bound water protons' spin magnetization is difficult to be detected directly, their spin magnetization is coupled to that of the free water protons due to magnetization transfer (MT), which allows for the exchange of collagen-bound and free water proton magnetizations according to a pseudo first-order rate equation(Edzes and Samulski 1977, Ceckler et al. 1992,

Eng, Ceckler and Balaban 1991, Kim et al. 1993, Wolff and Balaban 1989). As shown in Figure 4-1, the collagen's restricted protons interact with collagen-bound water protons via cross dipolar relaxation and chemical exchange, resulting in collagen-bound water protons' short T_2 relaxation time constant and broad spectral width.

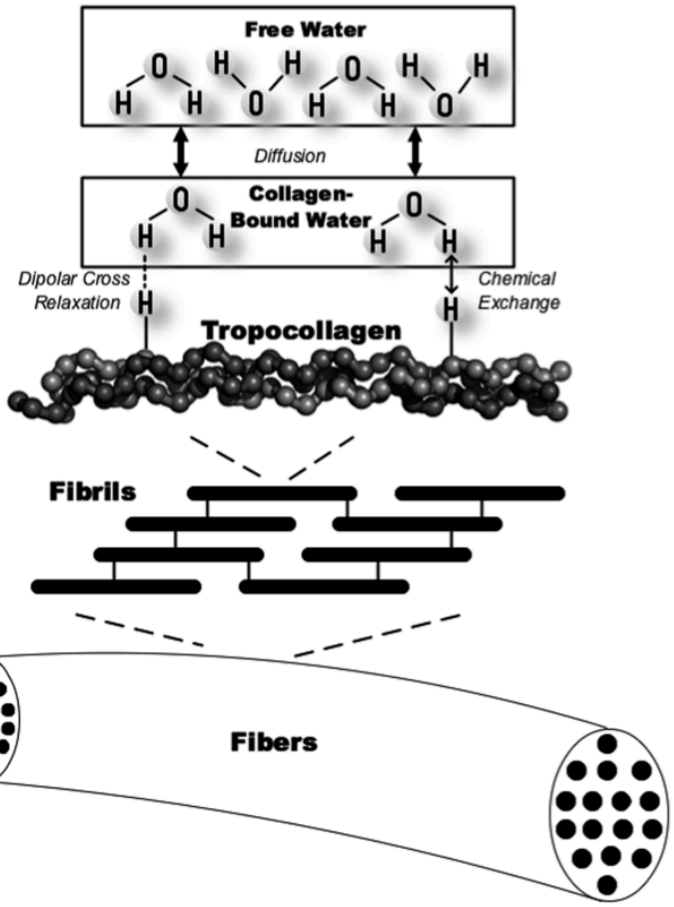

Figure 4-1. Diagram depiction of the complete proton magnetization transfer mechanism incorporating cross dipolar relaxation, chemical exchange, and proton diffusion. The restricted protons in collagen interact with collagen-bound water protons via dipolar cross relaxation and chemical exchange, which contribute to the broad spectral width of the collagen-bound water protons. The collagen-bound water protons are at the same time in an exchange equilibrium with the free water protons via simple diffusion.

Subsequently the collagen-bound water protons exchange with free water protons through simple diffusion(Eng et al. 1991). These steps result in the overall coupling of the collagen-bound water protons' spin-lattice relaxation with the detectable free water protons' spin-lattice relaxation. This coupling mechanism provides an indirect method to detect signal from the collagen-bound water protons, which is difficult to detect by conventional means.

MT phenomenon is observed and quantified with the help of an off-resonance saturation pulse, which selectively saturates the broad spectral width of the collagen-bound water protons and leaves the narrow spectral width of the free water proton relatively unsaturated, as shown in Figure 4-2.

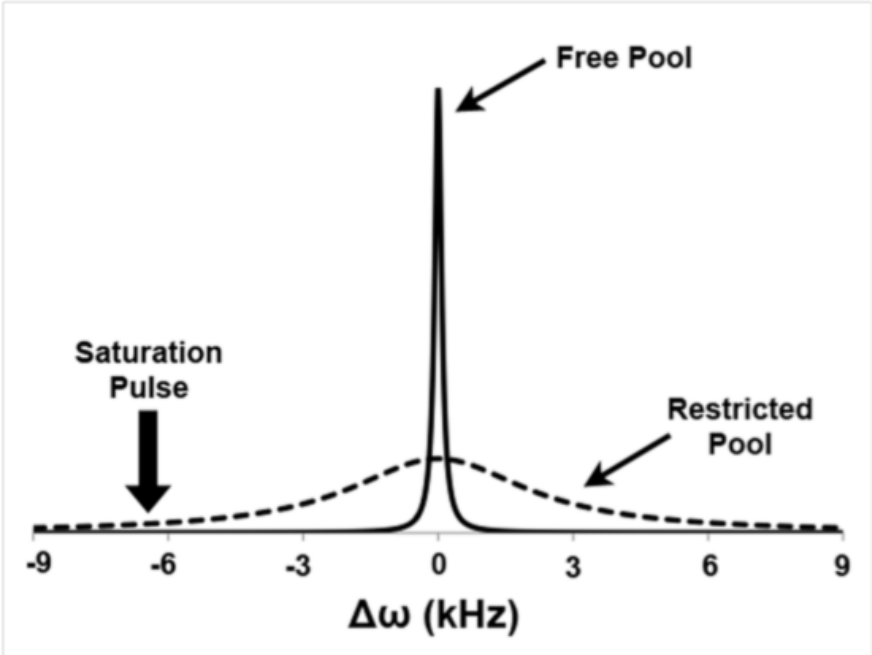

Figure 4-2. Frequency spectra of the collagen-bound protons with restricted motion (dashed line) and the free water protons (solid

line). The placement of the off-resonance saturation pulse is also shown.

Since the collagen-bound water protons' frequency spectrum is homogeneously broadened by cross dipolar interaction, the off-resonance saturation results in a decrease of the overall magnetization of the collagen-bound water protons. The MT mechanism dictates that the saturated collagen-bound water protons are in a state of constant exchange with the unsaturated free water protons, which results in the decrease of the detectable free water proton magnetization measured on-resonance.

It has been suggested that the hydroxyl, amine, and possibly carboxyl groups on the surfaces of macromolecules act as the sites for MT(Ceckler et al. 1992). Furthermore, it has been suggested that in cartilage the MT effect is mostly contributed by collagen rather than PG(Kim et al. 1993, Laurent et al. 2001). The probability of MT has been shown to be proportional to τ_c/r^6, where τ_c is the motional correlation time of the complex involving the restricted protons in macromolecules and the macromolecule-bound water protons, while r is the distance between them(Noggle and Schirmer 1971). In order for MT to occur efficiently, τ_c needs to be significantly longer than 10^{-9} s(Ceckler et al. 1991). Both chemical exchange and dipolar cross relaxation often require long τ_c sometimes in the microseconds range(Ceckler et al. 1992). Collagen fibers in biological tissues are often cross-linked, which makes their τ_c long enough for MT

to take place. It has been demonstrated that the side chain groups on collagen fibers from rat tendon are sufficiently restricted with a correlation time at around 10^{-8} s, which is long enough to allow for MT(Ceckler et al. 1992). In contrast, PG's hydroxyl side chains have been shown to be highly mobile by a previous ^{13}C NMR cartilage study(Torchia et al. 1977). The high mobility of PG's hydroxyl side chains likely results in too short of a τ_c for MT to occur. Due to the selectivity of the MT effect for collagen, the quantification of the MT phenomenon may lead to the specific quantification of collagen content in biological tissue containing both PG and collagen.

Earlier MT studies of the spine focused on cervical level IVDs, and these experiments were carried out at a low B_o of 0.3 T(Yoshioka et al. 1994, Yoshioka et al. 1997). Additional cervical IVD studies focused on MT's clinical utility as a contrast rather than its quantification and correlation with collagen content(Melhem et al. 1996, Melhem, Bert and Faddoul 2000, Melhem, Caruthers and Jara 1998). A previous MT study on cadaveric IVDs confirmed a positive correlation between MT and NP collagen(Paajanen et al. 1994). In this study, our primary objective is to validate MT MRI as a non-invasive method for spatial quantification of IVD collagen content *in vivo*, and to use MT MRI to investigate changes in NP collagen content due to IVD degeneration.

4.3 Methods

4.3.1 Experimental Protocol

Four human volunteers (mean age = 47 years) were recruited for this study in accordance with the regulations of the Institutional Review Board (IRB) at our institution. Each subject provided a written consent prior to the experiment. After consent was obtained, the subjects were instructed to lay supine on a 1.5 T Siemens Sonata clinical MRI scanner (Erlangen, Germany). Siemens supplied spine-array RF coil was used to acquire all images of the lumbar spine. A custom RF pulse sequence was programmed under SequenceTree pulse sequence programming environment (Philadelphia, USA). The sequence was based on a 2D turbo-spin-echo (TSE) acquisition scheme, with an off-resonance saturation RF pulse applied before each TR. The echo train of each TR is centrically encoded to maximize the MT contrast.

4.3.2 Effects of Off-Resonance Saturation Pulse Duration and B_1 on Free Water Spin

In order to determine the optimal parameters for the off-resonance saturation pulse, the free water proton magnetization saturation ratio (M_{sf}/M_{0f}) was simulated using equations previously derived by Eng *et al.*(Eng et al. 1991).

$$\frac{M_{sf}}{M_{0f}} = \left(\frac{\tau_{1f}}{T_{1f}}\right) \cdot \frac{1+\Delta\omega^2 T_{2f}^2}{1+\Delta\omega^2 T_{2f}^2 + \gamma^2 B_1^2 T_{1f} T_{2f}} + \left(1 - \frac{\tau_{1f}}{T_{1f}}\right) \cdot \frac{1+\Delta\omega^2 T_{2r}^2}{1+\Delta\omega^2 T_{2r}^2 + \gamma^2 B_1^2 T_{1r} T_{2r}} \quad \text{Equation 4-1}$$

$$\tau_{1f} = \frac{1}{k_{for} + 1/T_{1f}} \quad \text{Equation 4-2}$$

$$\frac{M_{sf}}{M_{0f}} = \frac{\tau_{1f}}{T_{1f}} + k_{for}\tau_{1f} e^{\left(-t/\tau_{1f}\right)} \quad \text{Equation 4-3}$$

Equation 4-1 was used to simulate the effect of the off-resonance saturation pulse's B_1 on the saturation ratio, which was by definition the ratio between longitudinal magnetization of the free water protons after the off-resonance saturation pulse (M_{sf}) and without saturation (M_{0f}). For all parameters, the subscript "f" indicates that the parameter is specific to the free water proton magnetization, while the subscript of "r" is specific for restricted proton magnetization. T_1 and T_2 were the spin-lattice and spin-spin relaxation time constants accordingly. The off-resonance frequency of the saturation transfer pulse is denoted by $\Delta\omega$, and it was set to 6.4 kHz for the following simulations. The proton gyromagnetic ratio is denoted by γ (42.576 MHz/T). τ_{1f} correpsonds to the free proton longitudinal relaxation with consideration of the magnetization exchange between free and restricted protons(Eng et al. 1991), as defined by Equation 4-2. In this equation, k_{for} was the pseudo first-order rate constant of MT from free water protons to restricted protons. Assuming the proton relaxation parameters T_{1f} = 1.5 s, T_{2f} = 60 ms, T_{1r} = 1 s, T_{2r} = 0.2 ms, k_{for} = 1 s^{-1}(Wolff and Balaban 1989), the saturation ratio was computed and plotted with B_1 as the independent variable for various $\Delta\omega$ values as shown in Figure 4-3(A).

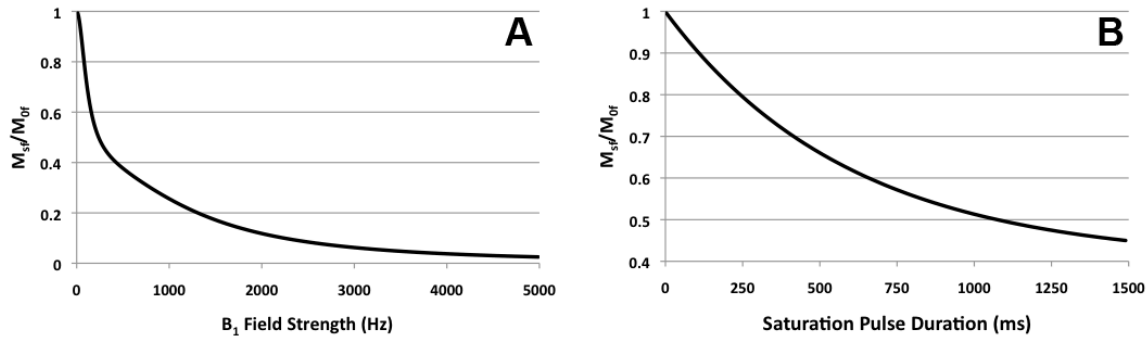

Figure 4-3.The dependency of free proton saturation ratio on B_1 field strength is illustrated in the simulated plot in (A). The change in saturation ratio with respect to duration of the off-resonance saturation pulse is demonstrated in the simulated plot in (B).

This plot demonstrates that the free water proton magnetization saturation increases with B_1 field strength at all $\Delta\omega$ values. The free proton magnetization saturation increases more rapidly with B_1 strength at lower $\Delta\omega$, likely due to the presence of significant direct saturation effect. Equation 4-3 was used to simulate the effect of the off-resonance saturation pulse duration on the saturation ratio, where t is the saturation pulse duration. Assuming an instantaneous saturation of the macromolecule-bound water proton spins, the free water proton magnetization exponentially decays to a steady-state with a time constant of $1/\tau_{1f}$(Eng et al. 1991). The simulated saturation ratio versus off-resonance saturation pulse duration data is plotted in Figure 3(B). This plot demonstrates that the saturation ratio decreases as a function of exponential decay of the off-resonance saturation pulse duration until it reaches a steady-state value. Therefore, both the amplitude and duration of the off-resonance saturation pulse should be maximized in order to observe maximum

MT effect. However, *in vivo* MT MRI protocol is limited by SAR, which also increases with both the B_1 and the duration of the off-resonance saturation pulse. As a result, the B_1 and duration used in the following *in vivo* imaging protocol were maximized so that the SAR limit was not exceeded for an average-sized adult subject.

4.3.3 Imaging Protocol

A series of gradient-echo (GRE) images were first acquired to localize the mid-sagittal slice of each subject's lumbar and thoracic spine. After localization, MR images were acquired using the previously mentioned MT TSE pulse sequence with the following parameters: TE/TR = 13/2000 ms, FOV = 25 x 25 cm, matrix size = 512 x 512, slice thickness = 5 mm, bandwidth (BW) = 296 Hz/Pixel, echo train length = 3, signal average = 3. Two images were collected for each subject, one with the MT preparation (M_s) and the other one without it (M_o). The off-resonance saturation pulse was applied at 6.4 kHz down field of the free water proton resonance frequency, at a B_1 of 200 Hz. The off-resonance saturation pulse was applied in a pulsed fashion, with a duration of 150 ms for a TR of 2000 ms. In addition to the sagittal spine images, axial view M_s and M_o images of the L4/L5 and L5/S1 IVDs of two subjects were also acquired.

4.3.4 *in vivo* Z-Spectra of the AF and the NP

A single subject underwent MR imaging using the previously described MT TSE pulse sequence, with the off-resonance saturation pulse applied at 17 frequency steps ranging from ±20kHz. A M_o image of the same subject was also acquired in order to calculate the saturation ratio (M_s/M_o) at each off-resonance frequency. A single observer (CW) manually chose a 4 mm diameter circular ROI in the NP region of the subject's L4/L5 IVD, along with a 2 mm diameter circular ROI in the AF region. The same ROIs were applied to the M_s images acquired at all 17 frequency steps as well as the M_o image. Afterward the saturation ratio for the NP and the AF compartments at each frequency step was computed. The saturation ratios were plotted against their corresponding off-resonance frequencies, yielding a pair of z-spectra for the NP and the AF compartments of the IVD.

4.3.5 IVD Pfirrmann Grading

Sagittal T_2-weigthed MR images of the subjects were acquired on the same MRI scanner, using the same Siemens spine-array RF coil and standard Turbo-Spin-Echo (TSE) pulse sequence. The pulse sequence parameters were as follows: TE/TR = 109/4000 ms, FOV = 28 x 28 cm, matrix size = 256 x 256, slice thickness = 4 mm, BW = 190 Hz/Pixel, echo train length = 25, signal average = 2. Individual lumbar IVDs (N=20) were segmented from the images,

indexed and randomized. A board-certified radiologist provided clinical assessments and Pfirrmann grades on the segmented IVD images according to the 5-point scale described by Pfirrmann *et al.*(Pfirrmann et al. 2001).

4.3.6 Image Processing and Data Analysis

Subsequent data processing and analysis were carried out using algorithms developed with MATLAB software (MathWorks, Natick, MA). MTR was computed according to Equation 4-4.

$$MTR = \frac{M_o - M_s}{M_o} \qquad \text{Equation 4-4}$$

This process was repeated on a pixel-by-pixel basis for each pair of sagittal spine M_s and M_o images to yield the MTR maps. A color scale was applied to the MTR maps in order to enhance their visualization. The IVD regions of the color MTR maps were manually segmented and overlaid on the corresponding grayscale M_o images. From the sagittal MTR map of each IVD, a single user chose a 4 mm diameter circular ROI in the center of the NP. The mean MTR of each ROI was then plotted against the Pfirrmann grade of the IVD. Linear regression analysis was applied to the MTR versus Pfirrmann grade data. Bivariate correlation of the MTR and Pfirrmann data pairs was carried out, and Pearson correlation coefficient and Spearman's rank correlation coefficient were computed to determine if there was a direct linear relationship

between MTR and Pfirrmann grade in IVD NP. The saturation in the observed saturation image (M_s) is actually consisted of both direct saturation (M_{dir}) and MT effect (M_{MT}), thus Equation 4-4 is expanded to account for these variables, as shown in Equation 4-5:

$$MTR = 1 - \left(\frac{M_{dir} + M_{MT}}{M_o} \right) \qquad \text{Equation 4-5}$$

In the previously described *in vivo* MT imaging protocol, M_{dir} was minimized by the large off-resonance frequency of 6.4 kHz chosen for the application of the saturation pulse.

4.4 Results

Greater signal saturation in the AF was observed after the application of the 6.4 kHz off-resonance saturation pulse, as shown in Figure 4-4.

Figure 4-4. This figure shows the sagittal M_o and M_s images of the L3/L4 IVD of a representative subject. The difference image (M_o-M_s) of the same L3/L4 IVD is shown on the right. Note the larger signal saturation in the AF compared to the NP.

The significant signal saturation of the AF compartment is best visualized in the subtraction (difference) image shown in the same figure, in which the anterior and posterior AF both demonstrates higher signal reduction compared to the NP.

The saturation pulse was applied at a large off-resonance frequency of 6.4 kHz, in order to minimize direct saturation and to ensure the observed signal saturation was mainly due to the MT effect. Figure 4-5 shows the *in vivo* AF and NP z-spectra from -20 kHz to 20 kHz.

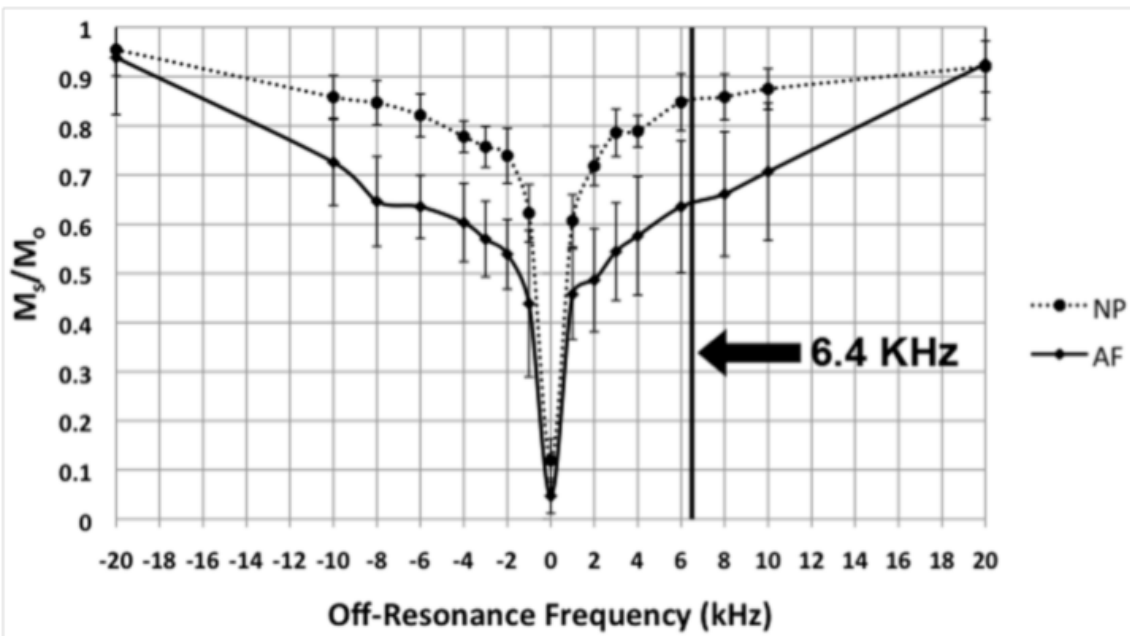

Figure 4-5. The z-spectra of a subject's L4/L5 IVD's AF and NP compartments. The y-axis is the saturation ratio, and the x-axis represents the off-resonance frequency of the saturation transfer pulse. The standard deviations of the MTR ROI measurements were graphed as the errors. The vertical line indicates the off-resonance frequency (6.4 kHz) used for all subsequent *in vivo* MTR map acquisition.

At an off-resonance frequency of 6.4 kHz, the z-spectra has shown 36% saturation for the AF and only 14% saturation for the NP. The

large difference between the AF and the NP's saturation ratios not only minimized the direct saturation effect, but also resulted in the largest contrast-to-noise ratio (CNR) between the AF and NP according to the z-spectra in Figure 4-5.

The overlaid MTR maps in Figure 4-6 offer clear visualization of the IVD's AF compartment, along with excellent demarcation between the AF and NP compartments.

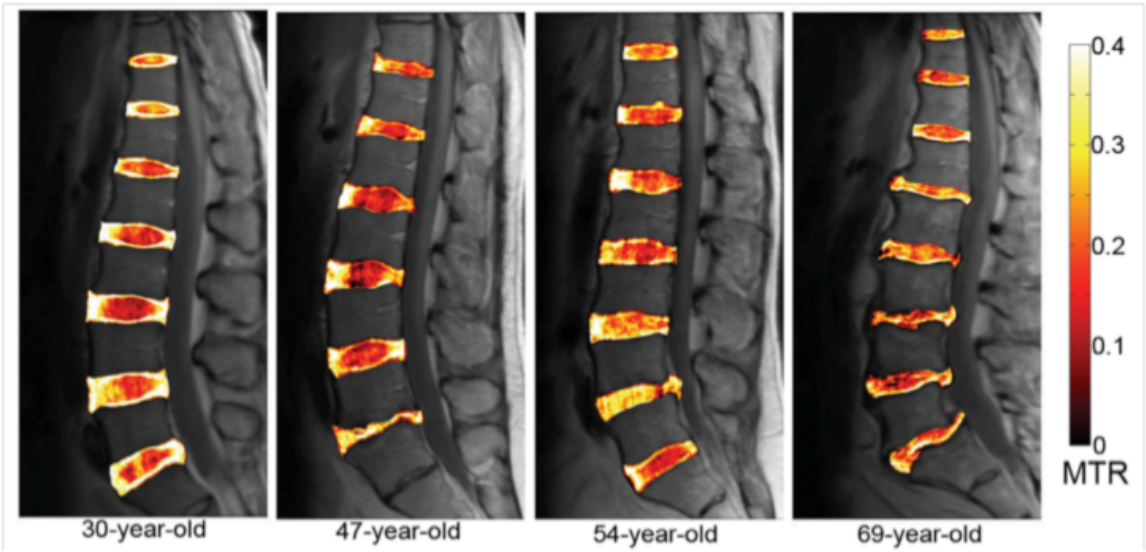

Figure 4-6. Sagittal MTR color maps overlaid on the grayscale M_0 images of four subjects. Note the overall clarity in demarcation between the AF and the NP compartments in the IVDs of the 30-year-old subject when compared to those of the 69-year-old subject. Also note the elevated NP MTR measurements in the L5/S1 IVD of the 47-year-old subject and in the L4/L5 IVD of the 54-year-old subject.

This observation is the most apparent in the IVDs of the youngest subject (age = 30 yrs.), which are presumably to be mostly healthy with the exception of a posterior herniation in the subject's L5/S1 IVD. This subject's healthy IVDs have clear distinction between the AF with high MTR and the NP with low MTR.

In contrast, the IVDs of the oldest subject (age = 69 yrs.) no longer exhibit a clear demarcation between the NP and the AF compartments. In addition, the oldest subject's IVDs show numerous morphological features typical of age-related degeneration, such as significant disc bulges, decreased disc height, and small annular tear. It is also observed that the younger subject's thoracic level IVD NP have higher MTR values compared to his lumbar IVD NP.

In Figure 4-7A, the older subject's L2/L3 IVD NP contains punctuate spots of high MTR values when compared to that of the younger subject.

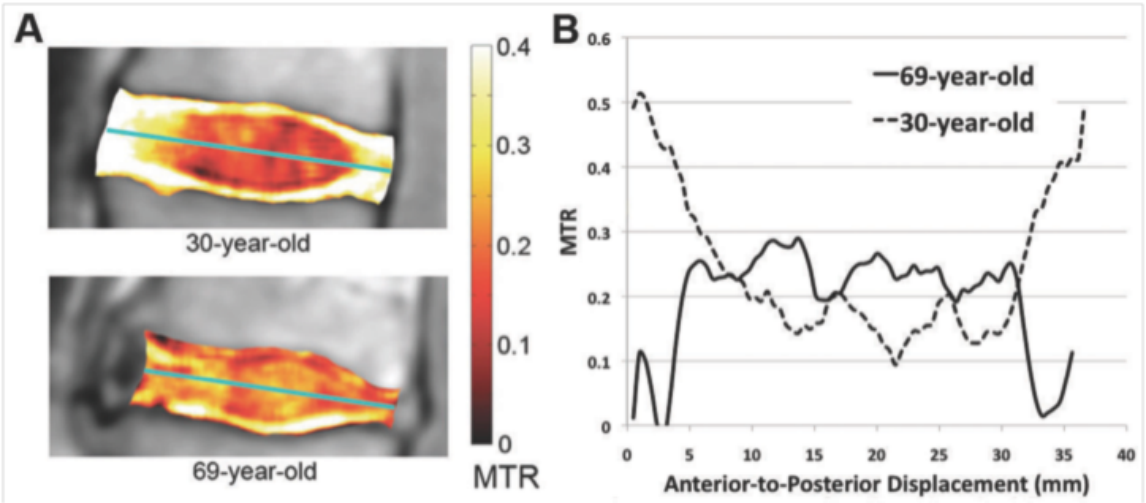

Figure 4-7(A). The MTR maps of the L2/L3 IVDs overlaid on top of the grayscale M_0 images for a pair of young and old subjects. (B) The anterior-to-posterior MTR profiles of the same IVDs shown in (A), the profiles were computed along the axes denoted by the green lines in (A).

The anterior-to-posterior MTR value profiles of these two subjects' IVDs (Figure 4-7B) also demonstrate the older subject's

IVD's increased NP MTR heterogeneity, as well as the lack of a clear MTR value difference between the AF and NP compartments.

Figure 4-8 contains the scatter plot of the NP MTR versus Pfirrmann grade data.

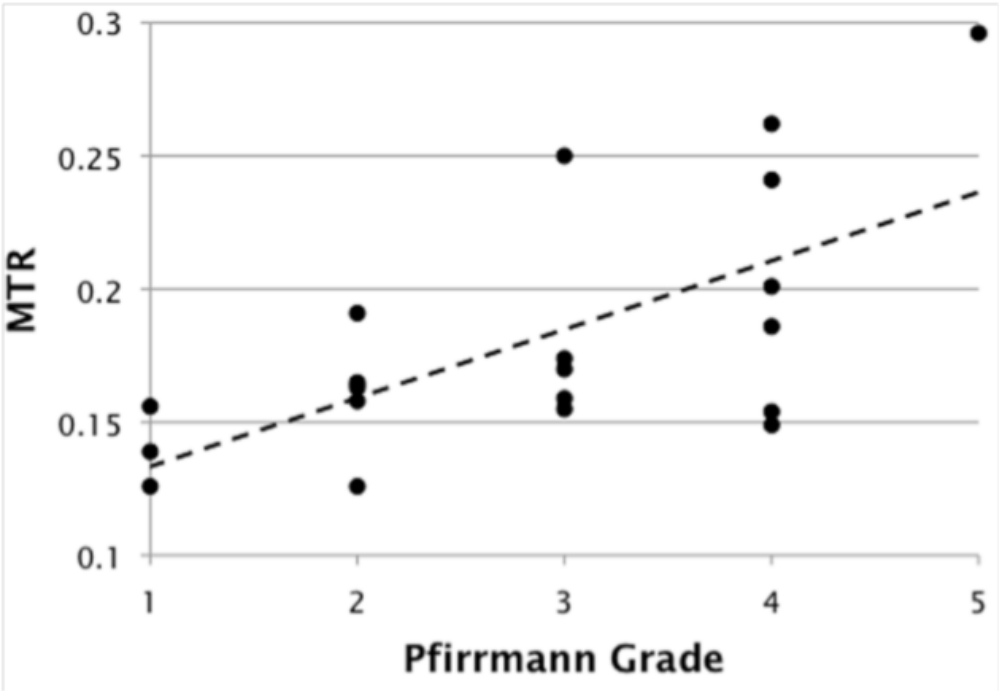

Figure 4-8. A plot of lumbar IVD NP MTR measurements vs. Pfirrmann grades assigned by a board-certified radiologist. Linear regression fit of the data is graphed as the dashed line.

The dashed line marks the linear regression fit of the data points. A one-tailed bivariate correlation analysis of the NP MTR versus Pfirrmann grade data yields a moderate but significant Pearson correlation coefficient of 0.652 at a significance level of $p<0.01$, as well as a moderate but significant Spearman's rank correlation coefficient of 0.568 at a significance level of $p<0.01$.

The L5/S1 IVD of the 47-year-old subject and the L4/L5 IVD of the 54-year-old subject both exhibit significantly elevated MTR values in the NP regions. Since the MTR values of these IVDs were not consistent with those of other IVDs in the same subjects, axial MTR maps of these IVDs were obtained. The corresponding axial MTR maps were computed, segmented and overlaid on the grayscale M_o images. In Figure 4-9, the 47-year-old subject's healthy L4/L5 MTR color map is shown on the left while the L5/S1 MTR color map is shown on the right.

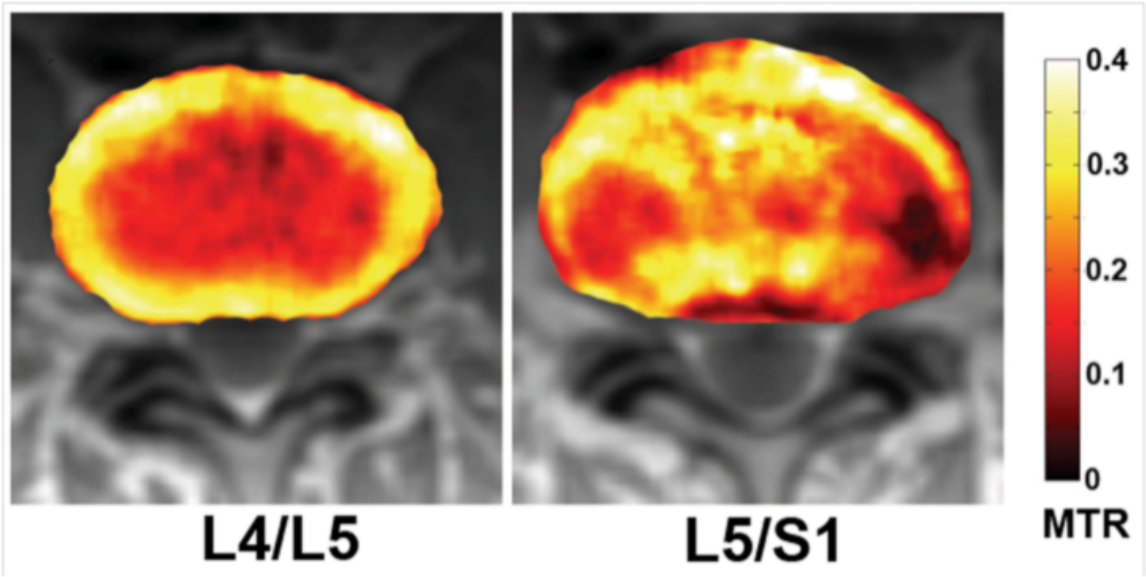

Figure 4-9. Axial color IVD MTR maps overlaid on top of the M_o IVD images of the 47-year-old subject. The L4/L5 IVD appears to be the healthier IVD.

In these MTR maps, the L4/L5 IVD has clear boundary between the AF and NP compartments, with significantly elevated MTR value in the AF. In contrast, the MTR map of the L5/S1 IVD shows significantly elevated MTR value in the central NP region. This

L5/S1 IVD received a grade of five on the Pfirrmann scale. In addition, the radiologist reported from the corresponding T_2-weighted image that this IVD's adjacent endplates underwent remodeling, showing signs of inflammation and fat deposits. These symptoms are typical to late stage IVD degeneration. In Figure 4-10, the 54-year-old subject's degenerated L4/L5 and healthy L5/S1 MTR color maps are shown.

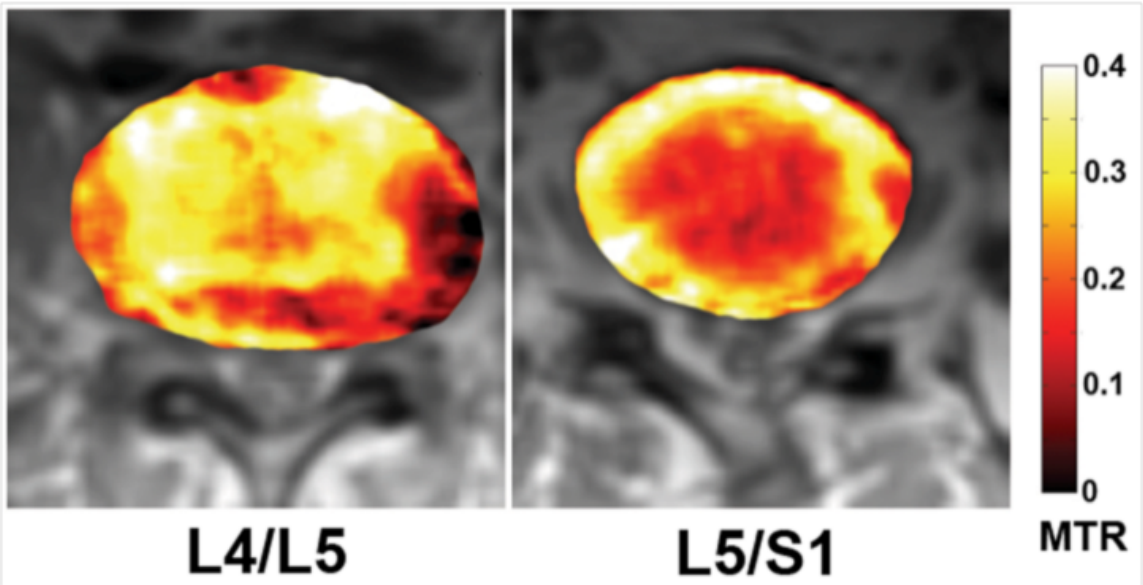

Figure 4-10. Axial color IVD MTR maps overlaid on top of the M_o IVD images of the 54-year-old subject. The L5/S1 IVD appears to be the healthier IVD.

Radiological report from the T_2-weighted image of this subject revealed significant IVD bulge from the L4/L5 IVD. In accordance with the radiological report, the MTR map of this IVD shows elevated MTR value in the center NP region, which displaces tissues with low MTR value toward the posterior side of the IVD.

4.5 Discussion

An earlier *in vivo* MT MRI study of human cadaveric lumbar IVD concluded a positive correlation between MT and collagen content(Paajanen et al. 1994). However, this study was conducted at a B_o field of 0.1 T. At such low B_o, the inherent low image SNR hinders the quantitative analysis of the images. More importantly, by conducting the MT experiment at a higher B_o field of 1.5 T, the comparatively shorter T_2 relaxation time constant of the collagen-bound protons cause additional broadening of their frequency spectra. This broadening of the collagen-bound protons' frequency spectrum has allowed us to apply the saturation transfer pulse at a large off-resonance frequency (6.4 kHz), which minimized the saturation pulse's direct saturation effect on the free water proton spin magnetization. Higher B_o field of 3 T would cause further broadening of the collagen-bound proton's frequency spectrum. However, the higher B_o field of 3 T also increases the off-resonance saturation pulse's power requirement, which would force reduction in both the saturation pulse amplitude and duration due to SAR restriction. Therefore, this study was carried out on a 1.5 T MRI scanner to achieve adequate MT effect with acceptable SAR.

The AF's higher saturation (36%) at 6.4 kHz observed from its z-spectrum in Figure 4-5 was most likely due to the AF's significantly higher collagen content compared to the NP. This

observation corroborates the result of a previous study showing that collagen constitutes 70% of the dry weight of the AF and only 20% of the dry weight of the NP(Eyre and Muir 1977). The other NP biomolecules such as elastin, fibronectin, and amyloid may also contribute to the observed MT effect. However, since these biomolecules are present only in small quantities compared to PG, collagen, and water, which together make up the overwhelming majority of the NP content, it is likely that the MT effect in IVD is primarily contributed by the presence of collagen. It is important to note that the MTR value in degenerated IVDs may be decreased by collagen denaturation. Previous studies have concluded a positive relationship between IVD collagen denaturation and degeneration(Antoniou et al. 1996, Hollander et al. 1996). Moreover, denaturation of collagen has been shown to slightly decrease the MT effect(Harel et al. 2008). Therefore, collagen denaturation in degenerated IVD could potentially contribute a small reduction in the elevated MTR value associated with increased NP relative collagen density.

Because there is a significant difference in absolute collagen content in the AF and the NP compartments (70% and 20% dry wt., respectively), the observed NP saturation (14%) appears to be unproportionally high when compared to the AF saturation (36%). The NP collagen content consists of mostly fine type II collagen fibers(Comper 1996b), which are randomly oriented(Inoue 1981). A previous study has shown that the type II collagen fibers form

cross-links in fibrocartilage(Eyre et al. 2002b), and the formation of type II collagen cross-links has been shown to increase MT effect(Fishbein et al. 2007), Recall that the likelihood of MT is proportional to τ_c/r^6, where τ_c is the molecular correlation time of the complex composed of the restricted protons in macromolecules and macromolecule-bound protons(Noggle and Schirmer 1971). In cross-linked type II collagen fibers, τ_c is likely to increase since the cross-links slow the molecular motion of the type II collagen fibers. Therefore, the likelihood of MT is increased in cross-linked type II collagen fibers of the NP, which contributed to a fraction of the observed 14% NP signal saturation after the application of the 6.4 kHz off-resonance saturation pulse.

Another factor that may have contributed to the elevated NP signal saturation is the direct saturation effect of the off-resonance saturation pulse. Since the relatively small amount of type II collagen fibers in the NP are loosely packed, they contain significant intrafibrillar water content(Grynpas et al. 1980). The motionally restricted characteristic of intrafibrillar water protons results in a broader frequency spectrum when compared to that of the free water protons. The broad spectral width makes the intrafibrillar water proton magnetization prone to direct saturation from the saturation pulse applied at a given off-resonance frequency. Therefore, the observed 14% NP saturation ratio may contain a direct saturation component.

The difference in NP MTR value between the thoracic and the lumbar IVDs of the youngest subject observed from Figure 6 was likely due to the difference in thoracic and lumbar IVD NP type II collagen contents. The higher NP MTR in thoracic IVDs indicates the presence of higher collagen content. This observation corroborates a previous study that concluded higher collagen content in the thoracic IVD NP compared to that of the lumbar IVD NP(Eyre and Muir 1977).

The observed punctuate spots of high MTR values in the NP of the older subject in Figure 4-7 suggests possible increased collagen in the older subject's IVD NPs. However, this increase in NP MTR in combination with the decreased disc height suggests that while the absolute collagen content in these IVD NPs may not have changed significantly, the relative density of collagen has increased due to the depletion of water and PGs. A previous *ex vivo* study on the macroscopic changes of IVD NP from aging has shown definite progression of the NP from a highly hydrated gel-like tissue to a fibrous material indistinguishable from the AF(Haefeli et al. 2006). However, this NP fibrosis progression pattern due to IVD degeneration has yet to be demonstrated in a quantitative fashion *in vivo*. Since the current standard assessment for IVD degeneration is based on T_2-weighted MR images and the Pfirrmann grade, we correlated the IVD NP MTR measurements with Pfirrmann grade. The moderate but significant correlation between MTR and Pfirrmann grade suggests that the MTR

indeed increases with IVD degeneration. The correlation is only moderate because the Pfirrmann grade is not a quantitative measurement of any particular macromolecular component of the IVD, instead it depends on qualitative observations such as disc height, hydration and other morphological features. These grading criteria of the Pfirrmann grade do not necessarily result in numerical grades that fall along a linear timescale of IVD degeneration. Moreover, Pfirrmann grade can be prone to intra- and inter-personal biases. In contrast to the Pfirrmann grade, the *in vivo* MT MRI protocol described in this study is based on quantitative measurement with specificity for IVD macromolecular composition. However, since Pfirrmann grade is an accepted measure of IVD degeneration, a positive relationship between NP MTR and Pfirrmann grade, as demonstrated here, indicates that NP collagen content indeed increases with degeneration.

In the axial MTR maps shown in Figure 4-9, the L5/S1 IVD shows significantly elevated MTR value in the central NP region. This observation along with the decreased disc height observed from Figure 4-6, suggests an increase in the relative density of NP collagen. In Figure 4-10, the L4/L5 IVD also shows elevated MTR value in the center NP region. However, the relatively normal disc height combined with the elevated MTR value in the NP region of this IVD suggests a possible increase in the absolute collagen content of the NP. However, without additional information, it is difficult to determine whether this increase in NP collagen is a

transient phase of aging-related IVD degeneration, or a specific trauma-induced fibrosis mechanism that is intended to stabilize an injured IVD, and to temporarily maintain its load-resisting property. This question can only be addressed with a long-term study using a large subject population. Regardless of whether the absolute collagen content increases in IVD degeneration, the increase in collagen relative density may reconcile the paradox in fibro-cartilage degeneration. Both articular cartilage and IVD belong to the same family of fibrocartilage composed of collagen and PG. Yet in articular cartilage, degenerated tissue exhibits increased T_2 and $T_{1\rho}$ relaxation time constants(Regatte et al. 2002, Wheaton et al. 2005, Li et al. 2007). While in IVD NP, degeneration leads to decreased T_2 and $T_{1\rho}$ relaxation time constants(Wang et al. 2007, Auerbach et al. 2006, Watanabe et al. 2007). When articular cartilage degrades, PGs leave the type II collagen extracellular matrix, and the vacated space is thus infiltrated with fluid, resulting in elevated T_2 and $T_{1\rho}$ relaxation time constants. In contrast, the loosely packed type II collagen extracellular matrix in IVD NP is not as readily infiltrated with fluid during degeneration, since both PG depletion and decreased IVD volume hinder the infiltration of fluid. Even when annular tears and fissures offer access to the degenerated NP, the lack of water-attracting PGs and collapsed disc space still prevent significant fluid infiltration. This process leads to the overall dehydration of degenerated IVDs(Kelsey et al. 1984). The results from this study confirms

that typical IVD degeneration causes an increase in NP relative collagen density, which could account for the lower T_2 and $T_{1\rho}$ relaxation time constants typically observed in degenerated IVDs(Auerbach et al. 2006, Watanabe et al. 2007).

4.6 Summary

This study demonstrated that the MT effect in IVD is mostly dominated by its collagen content. In a healthy IVD, the MTR is the highest in the collagen-rich AF. However, because of aging-related degeneration, we observed elevated MTR in the NP region of the IVD. In order to determine the relationship between MTR and IVD degeneration, we statistically determined a moderate but significant linear relationship between IVD NP MTR values and Pfirrmann grades. Thus, it was concluded that the relative density of NP collagen increases with IVD degeneration. In addition, IVD MTR map's significant CNR between AF and NP compartments makes it ideal for accurate segmentation of the NP and AF compartments. To the best of our knowledge, this study represents the first attempt of validating MTR mapping as a tool for quantifying collagen content in lumbar IVDs *in vivo*, and also the first attempt to determine lumbar IVD NP relative collagen density change due to degeneration *in vivo*. By establishing that MT MRI can be used to evaluate IVD collagen content *in vivo*, it can then be used in conjunction with PG-sensitive MRI techniques

to study IVD degeneration *in vivo*, and to shed additional light on the exact mechanism of IVD degeneration. In return, a more thorough understanding of IVD degeneration will promote the development of treatments and therapeutics aimed at halting or even reversing the degenerative process.

Chapter 5: Mapping of Intervertebral Disc Sodium Biexponential T_2* Relaxation at 7 T

5.1 Synopsis

Sodium MRI's role in [PG] quantification has been investigated in Chapter 1 and Chapter 2 using *ex vivo* bovine IVDs. The inherent low SNR of sodium MRI necessitates higher B_o field strength (7 T) for *in vivo* applications. The aim of this study is to quantify IVD sodium's T_2* relaxation, and to use the T_2* relaxation parameters to optimize the *in vivo* sodium MRI protocol in the following chapter. The biexponential T_2 relaxation characteristic of bovine IVD sodium was confirmed using an ultrashort TE (UTE) pulse sequence on a 7 T MRI scanner. The existence of a biexponential T_2 relaxation was confirmed, and spatial maps of the short T_2 (T_{2s}) and long T_2 (T_{21}) relaxation time constants were computed. The average NP T_{21} and T_{2s} relaxation constants were computed as 9.89 and 1.17 ms, respectively. The T_{2s} and T_{21} relaxations' broadening effects on the point-spread-function (PSF) were simulated along with that of the biexponential relaxation. The result shows that the PSF-broadening due to biexponential relaxation is close to that due to T_{21} relaxation. Additional PSF simulations were carried out at a range of acquisition BW values in order to determine the optimal BW that will yield the highest SNR with acceptable blurring. The result

shows that the BW can be as low as 50 Hz/Pixel while the PSF-broadening is still below a pixel.

5.2 Introduction

Sodium nuclear spins have been shown to exhibit a biexponential T_2 relaxation as a result of their quadrupolar interaction with the local electric field gradient(Hubbard 1970). Sodium NMR studies on *ex vivo* biological tissues such as red blood cells(Perman et al. 1986), muscle(Cope 1970, Shporer and Civan 1974, Berendsen and Edzes 1973), brain(Cope 1970), and kidney(Cope 1970) have also confirmed the existence of a sodium biexponential T_2 relaxation, with the short T_2 relaxation time constant ranging from 0.7 to 4.8 ms and the long T_2 relaxation time constant ranging from 7.0 to 26.0 ms. Moreover, the contribution of the short T_2 component to the total sodium signal has been shown to be between 62 and 68% in these studies. A separate study on excised rat cardiac tissue confirmed the existence of a sodium biexponential T_2 relaxation, however the short T_2 signal contributed to less than 50% of the total sodium signal(Burstein and Fossel 1987). A previous sodium MRI study on articular cartilage, another member of the same fibrocartilage family that IVD belongs to, have also confirmed the existence of a biexponential sodium T_2 relaxation(Borthakur et al. 1999). Sodium in biological tissue can diffuse across regions of

different electric field gradients, with some having non-zero averaged quadrupolar interaction as a result of Na^+ associating with the surface of macromolecules. Therefore, the difference in short and long T_2 signal fractions could be due to the particular molecular environment (bound vs. free) that the sodium nuclei encounter. Past sodium MRI studies of the IVDs were limited by sodium's low SNR and the minimal TE achievable due to hardware limitations(Granot 1988, Ra et al. 1988, Insko et al. 2002). Also hindered was the investigation of the unique biexponential T_2 relaxation mechanism of sodium in intact IVDs.

In this study, we carried out sodium MRI of *ex vivo* bovine IVDs on a 7 T whole-body MRI scanner. At high magnetic field strength, the SNR gain for sodium roughly increases linearly with the magnetic field strength(Haacke 1999). The IVDs were imaged with a radial acquisition UTE pulse sequence that was able to achieve a minimal TE of 220 µs(Nielles-Vallespin et al. 2007).

5.3 Methods

5.3.1 Bovine Specimen

Three bovine IVD samples were obtained from a local abattoir (Bierig Brothers, Vineland NJ), within a few hours of slaughter. Each caudal IVD specimen was surgically removed from the spine column and trimmed with a bone saw to include approximately 1 cm

of the vertebral body on each side, thus each processed IVD specimen contained a single IVD sandwiched between vertebral endplates, preserving the integrity of the motion segment.

5.3.2 Sodium MR Imaging Protocol for Bovine IVDs

Sodium MRI was carried out on a 7 T whole-body MRI scanner (Siemens Medical Solutions, Erlangen, Germany), using a custom-made sodium birdcage RF coil tuned to sodium resonance frequency at 7 T ($\omega_o = 78.6\ MHz$). An UTE sequence with 3D radial k-space sampling was used to acquire the sodium MR images(Nielles-Vallespin et al. 2007). The pulse sequence diagram of the radial UTE sequence is shown in Figure 5-1.

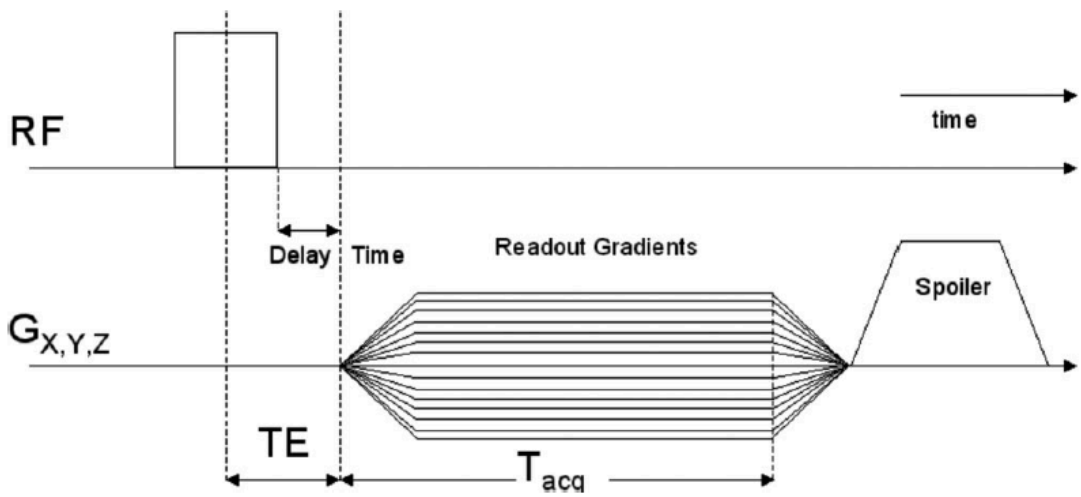

Figure 5-1. A pulse sequence diagram of the 3D radial UTE sequence used for sodium MRI at the 7 T MRI scanner. Signal sampling is carried out during the readout gradient ramp-up time(Nielles-Vallespin et al. 2007).

Sequence parameters were as follows: TR = 26 ms, flip angle = 40°, FOV = 25 x 25 cm, matrix size = 128 x 128, slices = 128, slice thickness = 1.95 mm, BW = 250 Hz/Pixel, radial spokes = 3000, TE = 0.22, 0.4, 0.6, 0.8, 1, 3, 4, 5, 7, and 9 ms. Images acquired with TE > 1 ms were signal averaged three times to improve SNR.

5.3.3 Calculating Sodium Biexponential T_2* Relaxation

All calculations were carried out using custom algorithms developed using MATLAB software (Mathworks, Natick, MA). The sodium biexponential T_2 relaxation was modeled as a simple summation of two single exponentials, as shown in Equation 5-1.

$$S = S_o \times \left(N_s \times e^{-TE/T_{2s}} + N_l \times e^{-TE/T_{2l}} \right) \qquad \text{Equation 5-1}$$

In Equation 5-1, S is the image signal intensity; S_o is the thermal equilibrium magnetization; T_{2s} and T_{2l} are the short and the long T_2 relaxation time constants measured in ms, respectively; N_s and N_l are the normalized spin densities of sodium nuclei undergoing T_{2s} and T_{21} relaxations, respectively; For sodium images acquired at long TEs (TE = 3, 4, 5, 7 and 9 ms), signal from the rapid T_{2s} relaxation would have already decreased to a negligible value prior to signal acquisition. Thus the image signal at these long TEs was assumed to be composed of only the T_{21} signal, and Equation 5-1 was simplified to yield

Equation 5-2, which consists of a single exponential. From Equation 5-2, parameters such as $S_o \times N_l$ and T_{2l} were computed using the five sodium images acquired at TE = 3, 4, 5, 7 and 9 ms.

$$S = S_o \times N_l \times e^{-TE/T_{2l}} \qquad \text{Equation 5-2}$$

For sodium images acquired at TE = 0.22, 0.4, 0.6, 0.8 and 1 ms, there was potentially significant contribution from sodium nuclei undergoing both T_{2s} and T_{21} relaxations. Therefore, the biexponential model in Equation 5-1 could not be solved directly. A single exponential mapping of the short TE sodium images would lead to a combined relaxation time constant (T_{2c}) that is an intermediate between T_{2s} and T_{21}. In order to isolate the signal of sodium nuclei undergoing T_{2s} relaxation from the short TE images, the sodium signal undergoing T_{21} relaxation calculated from Equation 5-2 was subtracted from the signal intensity of the short TE sodium images, yielding a signal value ($S_{compensated}$) that is composed mostly of sodium signal undergoing T_{2s} relaxation, as shown in Equation 5-3. In Equation 5-3, the T_{2s} and $S_o \times N_s$ parameters can be mapped according to a simple single-exponential model.

$$S_{compensated} = S - S_o \times N_l \times e^{-TE/T_{2l}} = S_o \times N_s \times e^{-TE/T_{2s}} \qquad \text{Equation 5-3}$$

Next, N_l and N_s parameters were computed from $S_o \times N_s$ and $S_o \times N_l$. Pixel-by-pixel application of Equation 5-1, Equation 5-2, and Equation 5-3 to the 3D sodium images acquired at the ten TEs yielded a set of 3D T_{2s}, T_{2l}, N_s and N_l maps.

5.3.4 Data Processing and ROI Analysis

All sodium images were transferred to a Macbook Pro computer (Apple, Cupertino, CA) for processing and ROI analysis. All image post-processing and data analysis were carried out using algorithms developed with MATLAB software (Mathworks, Natick, MA). For each IVD, a single observer (CW) chose a 6 mm diameter circular ROI in the center of the IVD NP on the mid-axial slice of the sodium image acquired at TE = 0.22 ms. The average ROI T_{2s}, T_{2l}, N_s and N_l values were subsequently obtained from the corresponding T_{2s}, T_{2l}, N_s and N_l maps.

5.3.5 PSF Analysis of UTE Sodium Images

T_2 relaxation during signal acquisition results in PSF-broadening in the readout direction. The PSF-broadening due to T_{2s}, T_{21}, and biexponential relaxations were simulated using T_{2s}, T_{2l}, N_s and N_l values averaged across the NP of all bovine IVD samples. This simulation was carried out with an acquisition BW value of 250 Hz/Pixel, which was the BW setting used in this study's sodium UTE imaging protocol. Additional PSF simulations were carried out

with BW = 25, 50, 100, 250, and 400 Hz/Pixel. Broadening of the PSF was quantified by measuring its full-width-at-half-maximum (FWHM).

5.4 Results

Each IVD sample that underwent sodium MRI in this study was imaged with ten different TEs. Figure 5-2 illustrates the mid-axial slice sodium image of a representative IVD sample at each TE. The short TE images in the ascending order of TE (TE = 0.22, 0.4, 0.6, 0.8 and 1 ms) are in the first row, while the long TE images in ascending order (TE = 3, 4, 5, 7 and 9 ms) are in the second row.

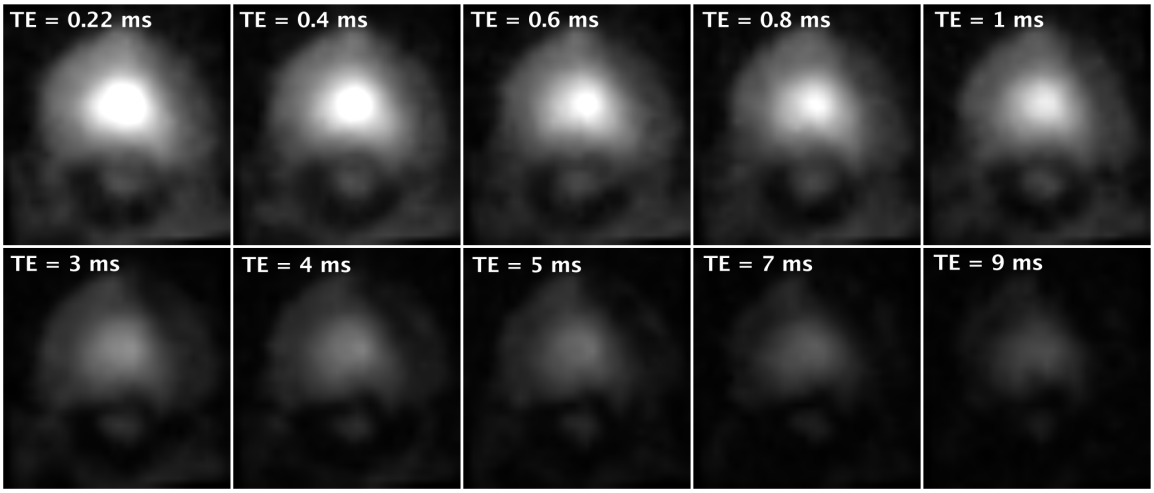

Figure 5-2. A collage of axial bovine IVD sodium images acquired at increasing TE. The anterior side of IVD face up in all images. Note the higher signal coming from the PG-rich center of NP.

In these images, the center of the NP has the highest sodium signal. The AF region of the IVD has significantly lower sodium concentration than the NP, and it is only visible in sodium images with short TEs (Figure 5-2, top row). It is also observed that the sodium signal decays less rapidly across the images acquired at short TEs, and it drops significantly between the short TE and the long TE images. This pattern of signal intensity change with respect to TE is quantitatively demonstrated in Figure 5-3, which shows a logarithmic plot of the same IVD's NP sodium signal at each TE.

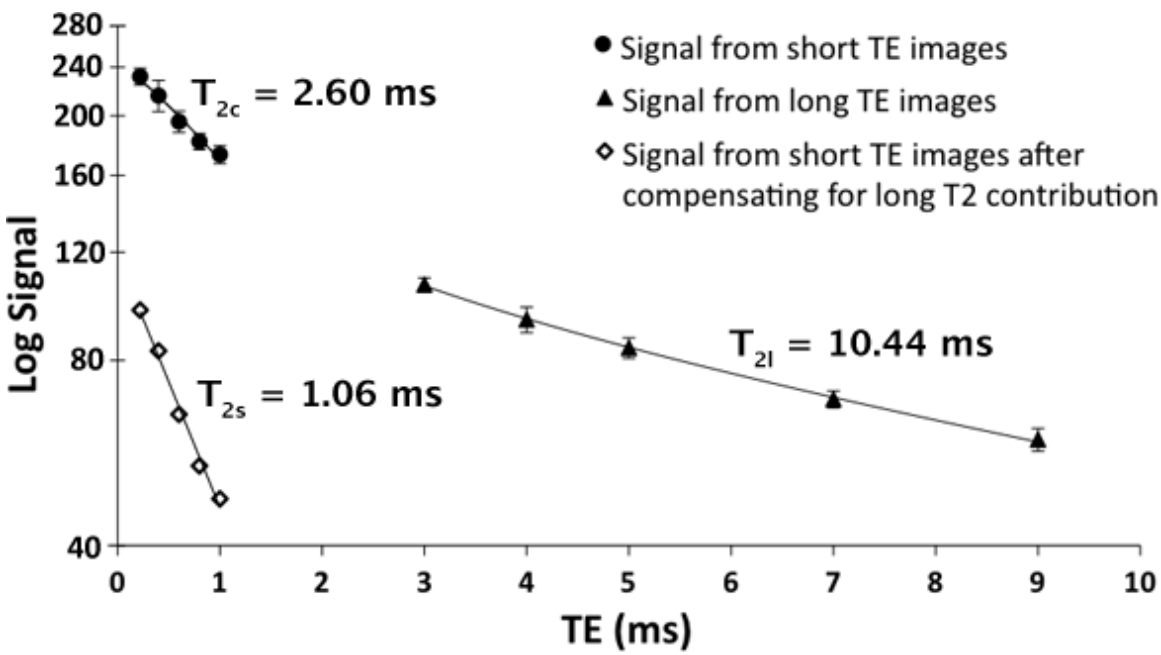

Figure 5-3. A logarithmic plot of the average IVD NP sodium signal at all TEs. The data points are grouped by short TEs (TE = 0.22, 0.4, 0.6, 0.8 and 1 ms) and by long TEs (TE = 3, 4, 5, 7 and 9 ms). The standard deviations of the IVD signals are shown as the error bars. The long and short T_2 relaxation time constants (T_{2s} and T_{2l}) and the combined (T_{2s} plus T_{2l}) relaxation time constant (T_{2c}) are displayed next to their corresponding exponential fits.

The data points are also grouped according to short TE and long TE. Exponential fitting of the long TE data points yielded a relaxation time constant of 10.44 ms, which corresponds to T_{2l}. Single exponential fitting of the short TE group data points yielded a relaxation time constant of 2.60 ms, which corresponds to T_{2c}. In addition, T_{2s} was determined to be 1.06 ms after compensating the signal intensity of the short TE data points for contribution from sodium signal undergoing T_{2l} relaxation.

The calculated sodium biexponential T_2 relaxation parameters (T_{2s}, T_{2l}, N_s and N_l) as well as the squared correlation coefficients for the exponential fits of sodium's T_{2s} component (R_s^2) and T_{2l} component (R_l^2) are shown in Table 5-1.

	T_{2l} (ms)	R_l	N_l	T_{2s} (ms)	R_s	N_s
Disc1	7.50	0.99	0.58	1.01	1.00	0.42
Disc2	10.88	0.98	0.52	1.11	0.98	0.48
Disc3	10.43	0.99	0.53	1.25	0.99	0.47
Average	*9.60*	*0.99*	*0.54*	*1.12*	*0.99*	*0.46*

Table 5-1. A table of the three IVD samples' NP ROI biexponential relaxation parameters and the squared correlation coefficients of the exponential fits for the T_{2l} and T_{2s} relaxations. The average relaxation parameter values of the three IVD samples are reported in the table as well.

From all three IVD samples, T_{2l} is approximately ten-fold longer than T_{2s}, and the N_s and N_l values are roughly equal with N_l being consistently slightly greater than N_s. Both R_s^2 and R_l^2 are > 0.95,

which suggests that the exponential fits that yielded these relaxation parameters are accurate.

The color axial IVD T_{2l} and T_{2s} maps are overlaid on top of the corresponding TE = 220 µs grayscale sodium image (Figure 5-4).

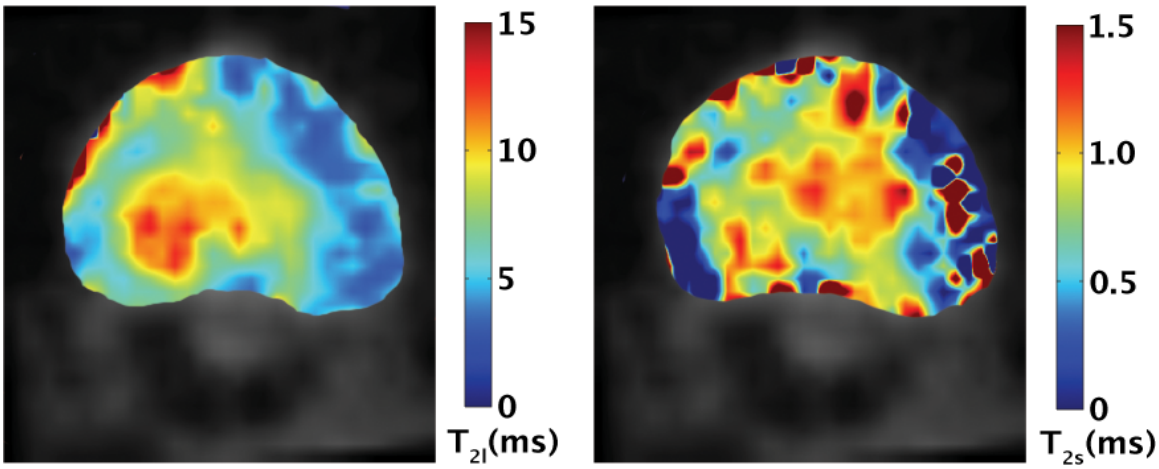

Figure 5-4. The segmented mid-axial IVD T_{2l} and T_{2s} color maps overlaid on the corresponding grayscale TE = 220 µs sodium image. The anterior side of the IVD faces up. Note the scales of the T_{2l} and T_{2s} maps are different due to the approximately ten-fold difference between the T_{2l} and T_{2s} relaxation time constants.

The color scales of the T_{2l} and T_{2s} maps are shown to the right of the overlaid maps. Due to the ten fold difference in T_{2l} and T_{2s} values, their color scales were adjusted accordingly. In the T_{2l} color map, the T_{2l} value is the highest in the center of the IVD NP region at around 11 ms, which decreases to around 5 ms in the periphery of the IVD occupied by the AF. The T_{2s} color map exhibits similar trend of high T_{2s} value in the NP center and low T_{2s} value in the surrounding AF. However, there are punctuate spots of high T_{2s} values in the AF region of the IVD.

In Figure 5-5, the same IVD's axial N_1 and N_s color maps are overlaid on top of the corresponding TE = 220 µs grayscale sodium image.

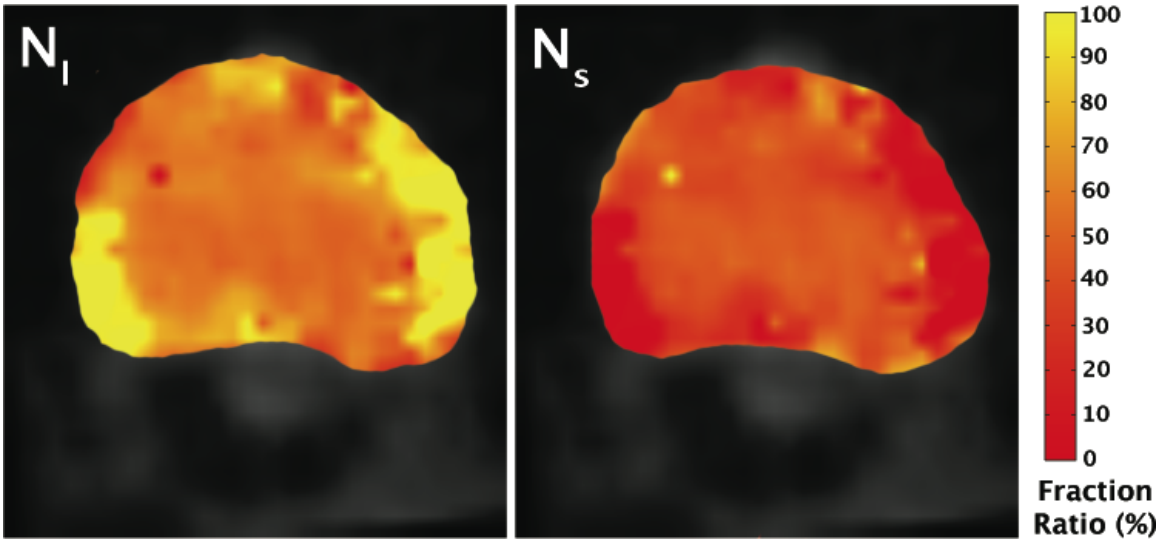

Figure 5-5. A representative IVD's axial N_1 and N_s color maps overlaid on the grayscale TE = 220 µs sodium image. The anterior side of the IVD faces up.

Their color scale has been scaled from 0 to 100%. In the N_1 color map, the NP regions shows a N_1 value of ~55%, while the AF region shows a N_1 of ~80%. The opposite trend is observed in the N_s color map, with the NP region at ~45% and the AF region at around ~20%.

The PSF-broadening due to sodium T_{2s} and T_{21} relaxations was investigated by computer simulation using the average T_{2s}, T_{21}, N_s and N_1 values. The resulting PSFs are shown in Figure 5-6.

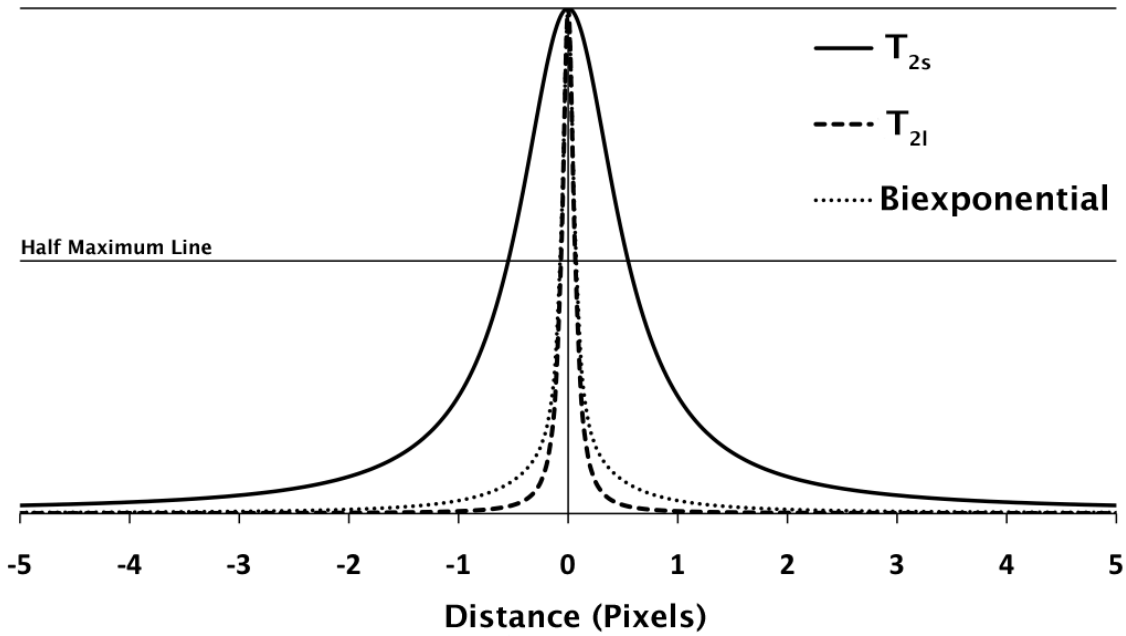

Figure 5-6. The PSFs of sodium's T_{2s}, T_{2l}, and biexponential relaxations simulated using the NP sodium relaxation parameters averaged across all three IVD samples. Each PSF is normalized to have a peak amplitude of unity, and the x-axis is in the unit of pixels. Therefore, each PSF's width, as intersected by the half maximum line, represents the FWHM. The PSF FWHM values computed from T_{2s}, T_{2l}, and biexponential relaxations are 1.09, 0.13 and 0.15 pixels, respectively.

This simulation was carried out with an acquisition BW of 250 Hz/Pixel. Figure 5-6 shows that sodium T_{2s} relaxation results in a FWHM of 1.09 pixel, T_{2l} relaxation results in a FWHM of 0.13 pixel, and biexponential relaxation results in a FWHM of 0.15 pixel. While the 0.15 pixel FWHM due to biexponential relaxation is between the 0.13 pixels FWHM due to T_{2l} and the 1.09 pixels FWHM due to T_{2s}, it is significantly closer to the PSF FWHM due to T_{2l} relaxation.

Simulation of PSF-broadening due to IVD NP sodium T_{2s}, T_{2l} and biexponential relaxation was also carried out using BW = 25, 50,

150, 250 and 400 Hz/Pixel. The resulting PSFs are shown in Figure 5-7.

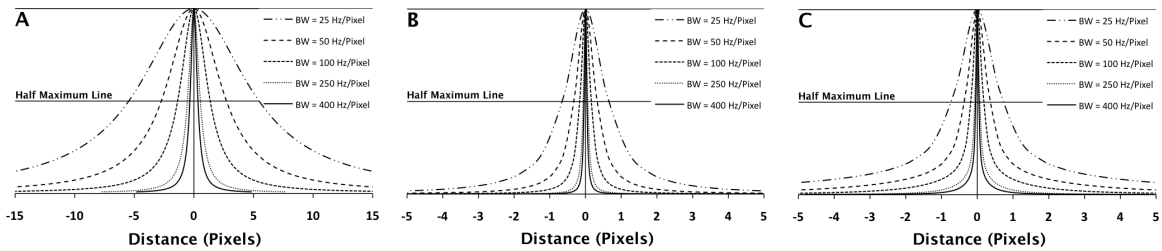

Figure 5-7. Simulated PSFs with BW = 25, 50, 100, 250 and 400 Hz/Pixels for (A). T_{2s}, (B). T_{2l} and (C). biexponential relaxations. Each PSF is normalized to have a peak amplitude of unity, and the x-axis is in the unit of pixels.

The FWHM measurements of all PSFs are summarized in Table 5-2.

	BW = 25 Hz/Px	BW = 50 Hz/Px	BW = 100 Hz/Px	BW = 250 Hz/Px	BW = 400 Hz/Px
T_{2s} FWHM:	***10.94***	***5.47***	***2.74***	***1.09***	***0.68***
T_{2l} FWHM:	***1.34***	***0.67***	***0.34***	***0.13***	***0.08***
Biexponential FWHM:	***1.53***	***0.76***	***0.38***	***0.15***	***0.10***

Table 5-2. A table of the PSF FWHM measures of IVD sodium's T_{2s}, T_{2l} and biexponential relaxation at BW = 25~400 Hz/Pixel.

The FWHM of the PSF due to biexponential relaxation, which corresponds to the blurring along the readout direction in typical sodium UTE image with short TE, exceeded a pixel only at the lowest BW of 25 Hz/Pixel. In comparison, the PSF due to T_{2s} alone exceeded a pixel at BW = 250 Hz/Pixel.

5.5 Discussion

In this study, we used a 7 T whole-body MRI scanner to carry out sodium MRI of bovine IVD samples using a radial UTE pulse sequence. The high B_o field of 7 T allowed us to achieve adequate image SNR efficiency and spatial resolution, which allowed for subsequent spatial mapping of sodium's biexponential T_2 relaxation. Five TEs (3, 4, 5, 7 and 9 ms) were chosen so the resulting sodium images would have negligible contribution from sodium signal undergoing rapid T_{2s} relaxation. Therefore, sodium T_{21} relaxation was solved as a single exponential function. The other five TEs (0.22, 0.4, 0.6, 0.8 and 1 ms) were chosen so their images would have a combination of both T_{2s} and T_{21} relaxation. IVD sodium's biexponential T_2 relaxation can be qualitatively observed in Figure 5-2's axial IVD sodium images acquired at all ten TEs. The five images acquired at short TEs have significantly greater signal intensity compared to the images acquired at long TEs. This pattern is quantitatively illustrated in the logarithmic plot of average NP sodium signal in Figure 5-3. In Figure 5-3, the images acquired at long and short TEs have significantly different slopes from their single-exponential fit. Their T_2 relaxation time constants are different by approximately a factor of four. This is because the T_2 relaxation time constant of long TE images is essentially T_{21}, assuming a negligible signal contribution from the rapid T_{2s} relaxation. In comparison, the sodium images acquired at short

TEs experienced a combination of both T_{2s} and T_{21} relaxations. Sodium signal undergoing T_{2s} relaxation has to be isolated from the short TE images by compensating the image intensity with the calculated T_{21} relaxation. The compensated signal is also shown in Figure 5-3, and it yielded a T_{2s} of 1.06 ms, which is less than half of T_{2c} and approximately one tenth of T_{21}. The significantly different T_{2s} and T_{21} relaxation time constants here further support that sodium in IVD exhibit biexponential T_2 relaxation, which confirms the finding from pervious studies on kidney(Cope 1970), heart(Burstein and Fossel 1987) and muscle(Cope 1970, Shporer and Civan 1974, Berendsen and Edzes 1973).

The T_{2s} and T_{21} color maps in Figure 5-4 suggest that both T_{2s} and T_{21} relaxation time constants are the highest in the PG-rich NP. The T_{21} map exhibits superior contrast between the AF and the NP region when compared to the T_{2s} map, which has punctuate spots of elevated T_{2s} values in the AF region. These spots of high T_{2s} values could be due to the inherent lower AF sodium signal intensity, which may make the calculation of T_{2s} relaxation time constant prone to error. The N_1 and N_s color maps also demonstrate compartmentalization of IVD's AF and NP compartments. The N_s of the NP is ~45%, while the N_s of the AF is only ~20%. The difference in IVD NP and AF N_s values might be due to the PG concentration difference. PG aggrecans account for approximately 50% and 20% of the wet weight of the NP and the AF, respectively(Urban and Roberts 2003). The positively charged Na^+

are attracted by the negatively-charged GAG side chains of the NP aggrecans. This electrostatic attraction between the slow-moving PG aggrecans and sodium nuclei likely increase their correlation time and subsequently enhance sodium's quadrupolar interaction with the electric field gradient, resulting in a larger fraction of Na^+ spins undergoing T_{2s} relaxation in the NP. This electrostatic attraction between GAG and Na^+ parallels the hydrogen bond between protons and collagen, which results in the increased rotational correlation time of bound protons in proton MRI. However, since Na^+ cannot form hydrogen bond with collagen, electrostatic interaction with negatively charged GAG dominates.

Sodium's rapid T_{2s} and T_{21} relaxation not only present a challenge in achieving adequate SNR, they also affect the spatial resolution of sodium images since T_{2s} and T_{21} relaxation broadens the PSF along the frequency readout direction. PSF-broadening results in image blurring, and it can be significant in sodium MRI due to the short TE typically employed. Meanwhile, PSF-broadening is dependent on acquisition time and therefore signal acquisition BW. A high BW of 250 Hz/Pixel was chosen for this study in order to minimizing the PSF-broadening at low TEs. However, the BW of 250 Hz/Pixel may be lowered to increase the SNR while maintaining acceptable blurring. According to Figure 5-6, at BW = 250 Hz/Pixel, the PSF due to T_{2s} relaxation has a FWHM of 1.09 pixels, which would not have resulted in significant image blurring in the frequency readout direction. Moreover, the

PSF from biexponential relaxation results in a FWHM of only 0.15 pixels, which is very close to the FWHM of the PSF of T_{21}. The PSF-broadening due to biexponential relaxation is the apparent PSF-broadening when the sodium image is acquired with the aforementioned TE of 220 µs. The PSF simulation shown in Figure 5-6 suggests that the apparent PSF-broadening is in fact very close to that due to T_{21} relaxation. Therefore, acquiring the sodium signal undergoing T_{2s} relaxation during UTE imaging does not seem to significantly increase PSF-broadening in the frequency readout direction. Next, PSF-broadening due to biexponential relaxation is simulated at several BW in order to find the BW that will yield the highest SNR while the PSF-broadening remains below a pixel. Table 5-2 indicates that the BW can be lowered to 50 Hz/Pixel while keeping the PSF-broadening due to biexponential relaxation under a pixel. Therefore a BW of around 50 Hz/Pixel should be used for future sodium MRI of IVD at 7 T, since it would increase the image SNR without excessive blurring.

5.6 Summary

This study demonstrated a technique that enables spatial mapping of IVD sodium's T_{2s}, T_{21}, N_s and N_1 biexponential relaxation components at 7 T. To the best of our knowledge, this study represents the first attempt to elucidate and to spatially

quantify sodium's biexponential T_2 relaxation model in intact IVD samples. The spatial mapping of IVD sodium's biexponential relaxation components has two profound ramifications in this study. The first ramification is IVD sodium MRI protocol optimization. Sodium MRI has inherently low SNR, therefore the signal acquisition BW is often lowered to compensate for the low SNR. However, a lower BW increases the acquisition time and may contribute significantly to blurring in the frequency readout direction as a result of T_2 relaxation weighting. This trade off between SNR and blurring calls for the optimization of acquisition BW, which was accomplished in this study via PSF simulation using measured IVD T_{2s}, T_{21}, N_s and N_1 values. The second ramification in this sodium biexponential T_2 relaxation spatial mapping technique lies in the potential of it being used to study IVD degeneration and other pathological processes. The bimolecular changes associated with these pathologies may alter the macromolecular environment of IVD's sodium nuclei, which could alter T_{2s} and T_{21} separately or altogether. It has been shown that IVD total sodium content decreases with degeneration(Wang et al. 2010). However, there could be an even more significant or an earlier change in the relative fractions of sodium nuclei undergoing T_{2s} and T_{21} relaxation. This subtle change can potentially be detected by the N_s and N_1 maps generated in this study.

Chapter 6: *in vivo* Sodium MRI of Intervertebral Discs at 7 T

6.1 Synopsis

Sodium MRI has already been validated as a technique for non-invasive [Na^+], [PG] and FCD quantification in Chapter 2, using *ex vivo* bovine IVD samples. This study intends to establish the correlation between IVD [Na^+] and degeneration *in vivo* on a 7 T MRI scanner. The BW optimization result from Chapter 5 served to optimize the pulse sequence protocol for the sodium MRI procedure of this study. Moreover, the *in vivo* IVD [Na^+] data in this study was also compared with MTR and $T_{1\rho}$ data acquired at a 1.5 T MRI scanner, in order to shed additional light on the detailed mechanism of IVD degeneration.

6.2 Introduction

Chapter 2 has already demonstrated sodium MRI's role in quantifying IVD [PG] content. Moreover, Chapter 3 introduced a mathematical model that can be used to calculate IVD osmotic pressure from sodium MR images. Despite sodium MRI's apparent utilities in diagnosing IVD degeneration, its inherent low SNR has hindered its role in *in vivo* applications. Previous *in vivo* sodium MRI studies relied on large voxel sizes with a thick slice

thickness typically at around 12 mm(Wang et al. 2010, Insko et al. 2002). The large voxel size increases SNR as well as the likelihood of partial volume, which lowers the accuracy of further quantitative analysis of the sodium MR image. Ultra-high field MRI scanner such as the 7 T MRI scanner used in this study can significantly improve the SNR of sodium MRI, resulting in both reduced scanning time and smaller voxel size. In this study, we acquired *in vivo* sodium MR images of human lumbar spine *in vivo* using a custom-built RF surface coil. The sodium images were corrected for both T_2* relaxation as well as B_1 inhomogeneity before IVD NP [Na^+] values were calculated. The calculated IVD NP [Na^+] values were then compared to the Pfirrmann grades. To the best of our knowledge, there has not been a previous study that attempted to correlate IVD degeneration with NP [Na^+] calculated from *in vivo* sodium MRI. In addition, Chapter 4 has already established MT MRI as a tool for monitoring IVD collagen density with respect to IVD degeneration, and Chapter 3 has established a correlation between $T_{1\rho}$ MRI and IVD osmotic pressure. Therefore, the calculated IVD NP [Na^+] values in this study were also compared to MTR and $T_{1\rho}$ values, which were acquired on a 1.5 T MRI scanner. MTR, $T_{1\rho}$ and [Na^+] together may reveal a more detailed picture of the not yet completely understood mechanism of IVD degeneration.

6.3 Methods

6.3.1 Human Subject Recruitment

Six human volunteers (mean age = 38 years) were recruited for this study in accordance with the regulations of the Institutional Review Board (IRB) at our institution. Each subject provided a written consent prior to imaging. After consent was obtained, the subjects were instructed to lay supine on a 7 T clinical MRI scanner (Siemens Medical Solutions, Erlangen, Germany). A custom-engineered single-loop surface RF coil (diameter = 22 cm) tuned to 78.6 MHz was inserted underneath the subject's lumbar region. A 5 cm thick foam insulation padding was placed between the subject and the surface coil. A series of 400 mM saline phantoms were imbedded inside the foam padding to mark the outer boundary of the surface RF coil in order to aid localization.

6.3.2 Sodium MRI Protocol

Prior to the acquisition of the sodium MR images needed for the subsequent analysis, a low-resolution sagittal sodium MR image was obtained to ensure that the subject's lumbar region falls within the sensitive region of the RF surface coil. Next, the signal acquisition was carried out using a gradient echo (GRE) pulse sequence with the following sequence parameters: TR/TE =

320/8.77 ms, FOV = 400 x 400 mm, matrix = 128 x 64, slice thickness = 5 mm, number of slices = 32, NEX = 8, pulse duration = 2 ms, BW = 50 Hz/Pixel, transmit voltage = 200 V. The asymmetric echo and partial Fourier filter options were also selected to further decrease the TE. The acquisition time was 24 minutes and 35 seconds. The high transmit voltage of 200 V was chosen to maximize tissue penetration, since the IVDs are located approximately 10 cm from the dorsal skin surface. The BW parameter was chosen to maximize SNR. As discussed in Chapter 5, a BW of 50 Hz/Pixel results in a PSF broadening of less than 1 pixel with a T_2 ~10 ms. Meanwhile, the SNR increases significantly with the lower BW. However, lower BW also increases the signal acquisition time, which increases the minimum TE and decreases the signal. Therefore, a simulation was carried out according to Equation 6-1, in order to determine the BW at which the IVDs would yield the highest SNR with acceptable blurring.

$$SNR \propto \frac{e^{-TE/T_2}}{\sqrt{BW}} \qquad \text{Equation 6-1}$$

In Equation 6-1, TE is calculated using Equation 6-2.

$$TE = 0.5 \cdot \text{Pulse Duration} + 40\mu s + \frac{0.5}{\text{BW}} \qquad \text{Equation 6-2}$$

The 40 μs in Equation 6-2 represents the downtime as the MRI scanner switches from transmit to receive mode. The result of the simulation is shown in Figure 6-1.

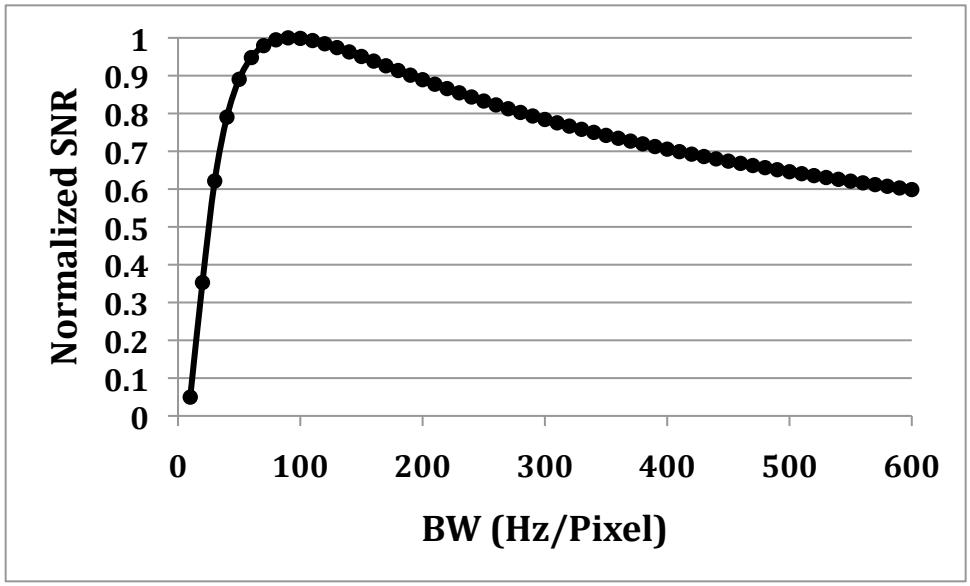

Figure 6-1. Simulated normalized SNR with respect to the BW. Simulation was carried out using a T_2 of 10.84 ms, which is the average IVD T_2 calculated in the following section.

The simulation suggests that the normalized SNR reaches a maximum at a BW of approximately 90 Hz/Pixel. The optimized BW of 50 Hz/Pixel concluded from Chapter 5 was used in the sodium MRI protocol of this study. However, the normalized SNR at a BW of 50 Hz/Pixel is still approximately 90% of the peak SNR according to Figure 6-1.

6.3.3 T_2 Relaxation Correction

The difference between the T_2 relaxation rates of the IVDs and the spinal cord requires T_2 correction, if the spinal cord is to be used as an internal calibration point (150 mM) for the calculation of [Na^+]. A 28-year-old asymptomatic male subject was recruited for this study according to the IRB regulations. A

written consent was obtained prior to the scan. A GRE-based multiecho pulse sequence was used to acquire the T_2-weighted images. The imaging parameters were as follows: TR/TEs = 350/2.2, 4.41, 6.62, 8.83, 11.04 and 13.25 ms, FOV = 400 x 400 mm, matrix = 64x64, number of slices = 32, slice thickness= 16 mm, BW = 500 Hz/Pixel, NEX = 2. The total imaging time was 26 minutes and 53 seconds.

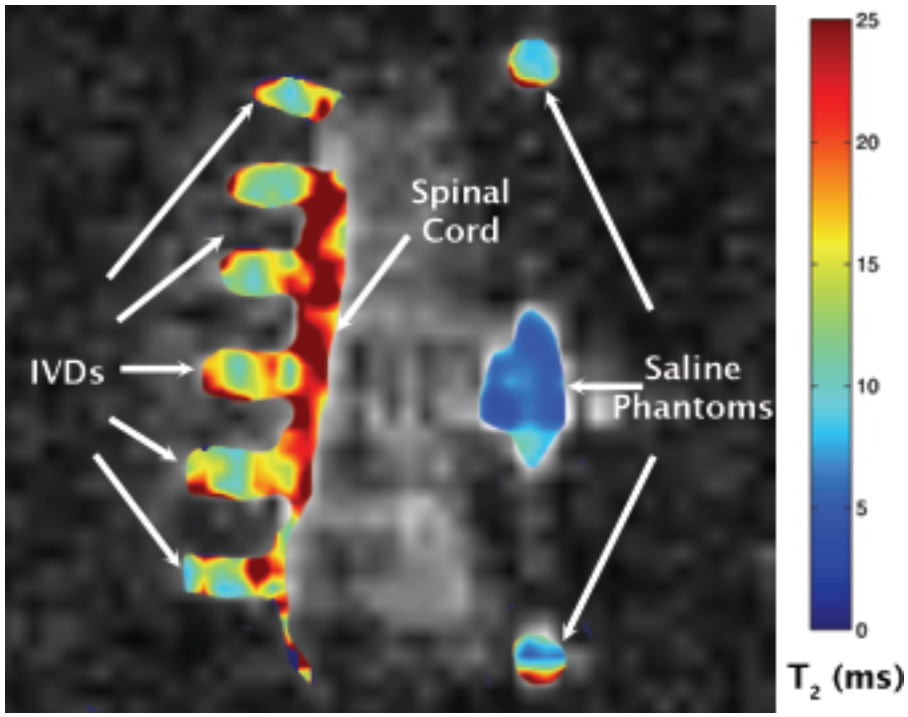

Figure 6-2. The sagittal T_2 map overlaid on top of the grayscale sodium MR image acquired at TE = 2.2 ms. The IVDs, spinal cord, and saline phantoms are labeled accordingly. Note the significantly higher T_2 relaxation time constant in the spinal cord region, due to the presence of CSF.

From the T_2 map in Figure 6-2, a single observer (CW) chose a 4 mm ROI in the center of each IVD, as well as four 4 mm ROIs along the spinal cord. The IVD ROIs and spinal cord ROIs were

separately averaged, yielding an average T_2 of 10.84±1.24 ms for the IVD and an average T_2 of 31.07±2.04 ms for the spinal cord.

6.3.4 B_1 Inhomogeneity Correction

The B_1 field of a single loop surface RF coil decreases along a normal axis pointing away from the coil plane. Since B_1 field strength is directly related to flip angle, the B_1 inhomogeneity needs to be corrected before the IVD signal can be compared to the CSF signal for [Na^+] calibration. In order to determine the B_1 field, we acquired four sodium MR images of a 28-year-old subject at four different excitation pulse durations. Pulse duration is related to flip angle according to Equation 6-3.

$$\text{Flip Angle} = \gamma \cdot B_1 \cdot \text{Pulse Duration} \qquad \text{Equation 6-3}$$

Therefore, the four images acquired with different pulse duration have different flip angles. A single observer (CW) chose a single 4 mm diameter ROI in one representative IVD NP from each of the images. The mean signal values of the four ROIs were then mapped to a sine function using a custom algorithm developed under MATLAB programming platform (Mathworks, Natick, MA). The ROI signal values and the resulting sine fit are plotted in Figure 6-3.

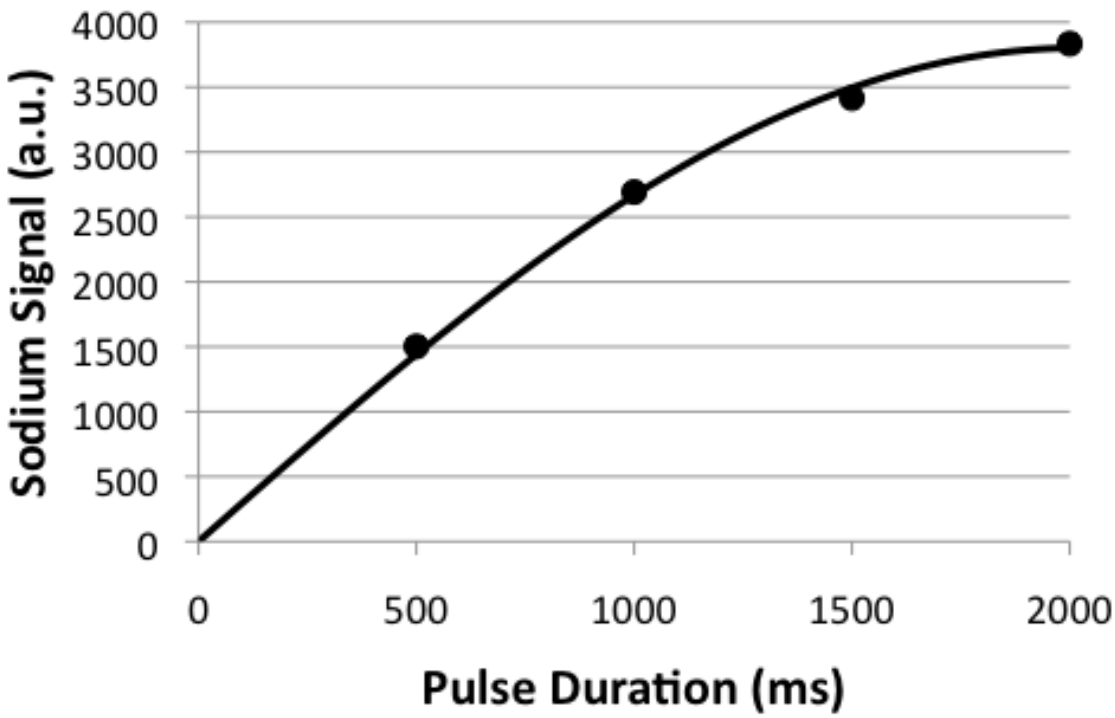

Figure 6-3. Plot of sodium signal from a 4 mm ROI in the center of a typical IVD NP at four increasing pulse durations. The solid circular dot represents the IVD NP ROI values, while the solid line shows the result of the sine fit of the four ROI values.

The sine fit in Figure 6-3 resulted in an expression (Equation 6-4) that relates pulse duration in µs to the amplitude of the sine fit.

$$S = 254.67 \bullet \sin(0.0013 \bullet \text{pulse duration}) \qquad \text{Equation 6-4}$$

From Equation 6-4, the flip angle was calculated using the actual sodium MRI protocol's pulse duration of 2000 µs. Pixel-by-pixel application of the sine fitting procedure and the flip angle calculation resulted in a spatial map of flip angles, shown in Figure 6-4.

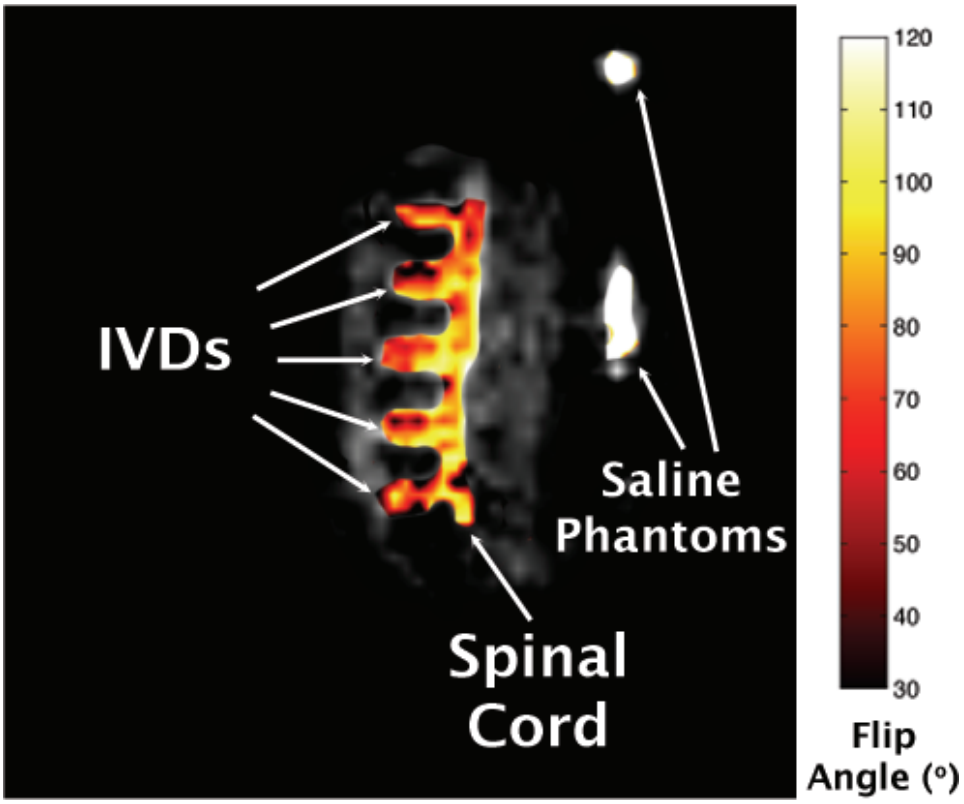

Figure 6-4. An overlay of the segmented sagittal flip angle map of a 28-year-old subject on top of the corresponding gray anatomical sodium image. The IVDs, spinal cord, and saline phantoms are labeled accordingly.

From Figure 6-4, the average flip angles in the IVDs and the spinal cord were computed by letting a single observer (CW) choose four 4 mm diameter circular ROIs in the IVDs as well as in the spinal cord, yielding an average flip angle of 64.62° for the IVDs and 85.19° for the spinal cord. These average flip angle values for the IVDs and the spinal cord were used for subsequent B_1 inhomogeneity correction.

Since B_1 inhomogeneity affects both the transmit and the receive profiles, B_1 correction has to account for both the transmit and the receive B_1 profile according to Equation 6-5.

$$S_{corrected} \propto \frac{S_{raw}}{\sin(\alpha)\cdot \alpha} \qquad \text{Equation 6-5}$$

In Equation 6-5, the uncorrected signal (S_{raw}) is divided by both the flip angle (α) as well as the sine of α. The division by sine of α corrects for the transmit B_1 inhomogeneity. Meanwhile, the division by α corrects for the receive B_1 inhomogeneity, since α is directly related to B_1 according to Equation 6-6.

$$\alpha = \gamma \cdot B_1 \cdot \tau \qquad \text{Equation 6-6}$$

In Equation 6-6, the gyromagnetic ratio (γ) and the pulse duration (τ) are both constant, which results in a linear relationship between α and B_1.

6.3.5 Computing [Na^+]

A single observer (CW) chose a 4 mm circular ROI in the center of each IVD NP for three consecutive sagittal slices. The IVD NP ROI values were averaged. For each IVD, a single 4 mm circular ROI in the spinal cord at approximately the same vertical height as the IVD was also chosen from a single sagittal slice. The average IVD NP and spinal cord values were separately corrected for both T_2 relaxation and B_1 inhomogeneity as discussed earlier. Since the spinal cord CSF [Na^+] is typically constant at 150 mM, the IVD NP [Na^+] was then calculated according to Equation 6-7.

$$\left[Na^+\right]_{NP} = 150mM \bullet \frac{S_{NP}}{S_{CSF}} \qquad \text{Equation 6-7}$$

In Equation 6-7, IVD NP $[Na^+]$ ($[Na^+]_{NP}$) was calculated as the product of 150 mM with the ratio of the NP signal (S_{NP}) and the CSF signal (S_{CSF}).

6.3.6 Pfirrmann Grading

Sagittal T_2-weigthed MR images of the subjects were acquired on a Siemens 1.5 T MRI scanner (Erlangen, Germany), using a Siemens spine-array RF coil and standard Turbo-Spin-Echo (TSE) pulse sequence. The pulse sequence parameters were as follows: TE/TR = 109/4000 ms, FOV = 28 x 28 cm, matrix size = 256 x 256, slice thickness = 4 mm, BW = 190 Hz/Pixel, echo train length = 25, signal average = 2. One observer (CW) assigned Pfirrmann grades to each IVD according to the 5-point scale (Figure 6-5) described by Pfirrmann *et al.*(Pfirrmann et al. 2001).

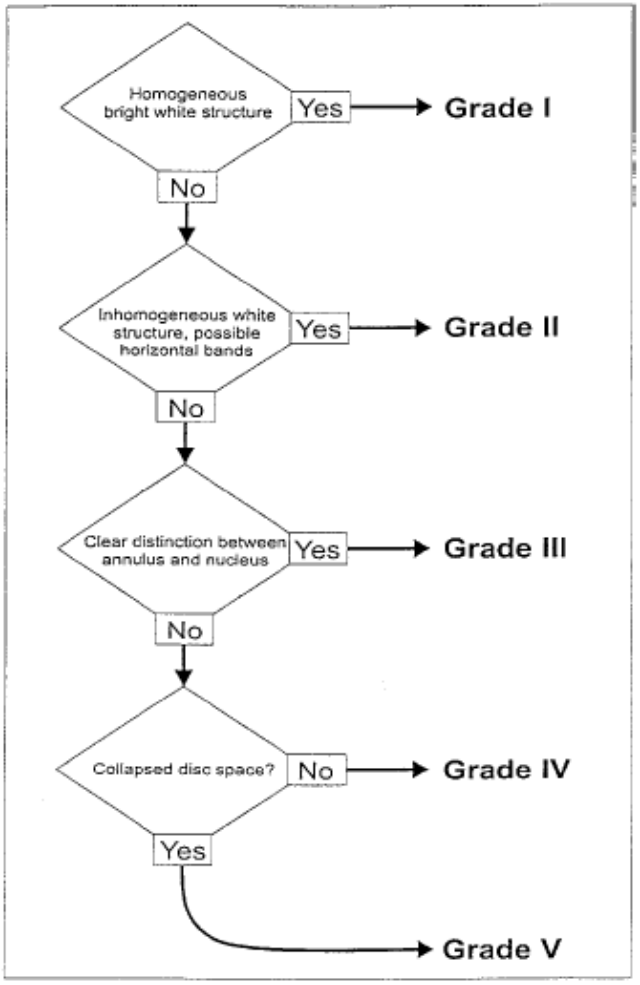

Figure 6-5. Grading scheme for assessing lumbar IVD degeneration developed by Pfirrmann *et al.*(Pfirrmann et al. 2001)

6.3.7 Self-Coregistered Lumbar IVD MTR and $T_{1\rho}$ Mapping

Three subjects (mean age = 42 years) who underwent sodium MRI at 7 T also underwent self-coregistered MT and $T_{1\rho}$ MRI on a Siemens 1.5 T MRI scanner (Erlangen, Germany). MT MRI was carried out using the previously mentioned MT TSE pulse sequence with the following parameters: TE/TR = 7.5/2000 ms, FOV = 25 x 25 cm, matrix size = 256 x 256, slice thickness = 5 mm, BW = 296 Hz/Pixel, echo train length = 15, averaging = 3. The off-

resonance saturation pulse was applied at 6.4 kHz down field of the free water proton resonance frequency, at a B_1 amplitude of 200 Hz. The off-resonance saturation pulse was applied in a pulsed fashion, with a duration of 300 ms for a TR of 2000 ms. A sagittal MTR map was acquired in 3 minutes and 44 seconds. $T_{1\rho}$ MRI was carried out using a custom spin-lock prepared TSE pulse sequence. The FOV and resolution parameters were identical to those of the MT TSE sequence. The imaging parameters were as follows: TE/TR = 13/3000 ms, slice thickness = 5 mm, turbo factor = 7, averaging = 2. $T_{1\rho}$-weighted MR images at five spin-locking times (TSL = 10, 20, 40, 60 ms) were collected, at a spin-lock amplitude of 400 Hz, for a total imaging time of 14 minutes and 56 seconds.

6.3.8 Statistical Analysis

Two-tailed bivariate correlation analysis of the IVD NP MTR, $[Na^+]$, $T_{1\rho}$ and Pfirrmann grade was performed using SPSS Statistics 18 software (SPSS, Chicago, USA). Pearson correlation coefficient and Spearman's rank correlation coefficient were computed to determine if there are linear relationships between Pfirrmann grade and IVD NP MTR, $[Na^+]$ and $T_{1\rho}$ values.

6.4 Results

The sodium MR images acquired in this study typically had a SNR of 35, with an image acquisition time below 30 minutes. Due to the relatively small slice thickness (5 mm), multiple consecutive sagittal slices covering the IVD region were obtained as shown in Figure 6-6.

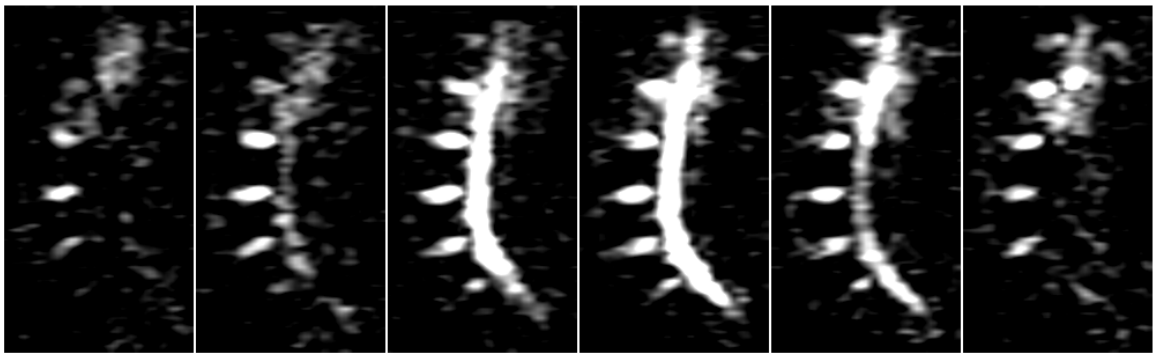

Figure 6-6. Six consecutive 5 mm sagittal slices of the sodium MR image of a 35-year-old subject's lumbar spine. Note the bright sodium signal coming from the subject's spinal cord.

In Figure 6-6, the five lumbar IVDs and the spinal cord can be clearly visualized across multiple sagittal slices. The spinal cord's left-to-right width is significantly less than that of the IVDs, therefore the spinal cord is only clearly visible in two slices.

The two-tailed bivariate correlation analysis between IVD Pfirrmann grades and [Na^+] values (N=27) yielded a Pearson correlation coefficient of -0.610 and a Spearman's rank correlation coefficient of -0.634 at $p<0.01$. The linear

regression fit of the Pfirrmann grades and the [Na^+] values is graphically shown in Figure 6-7.

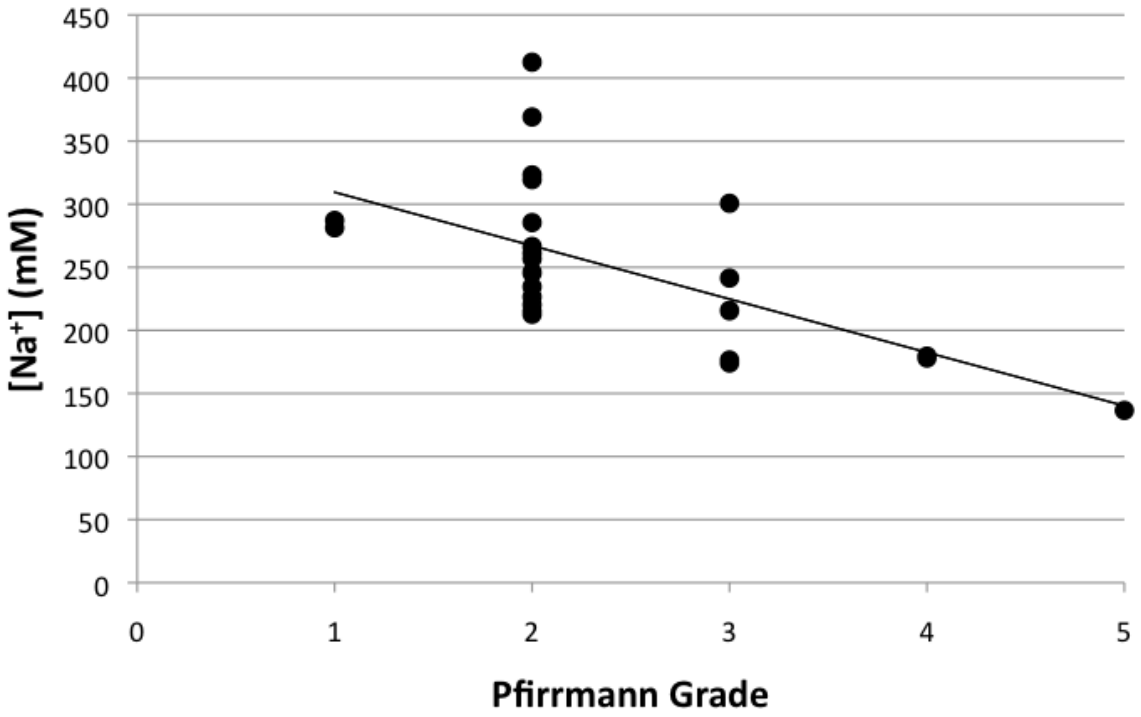

Figure 6-7. Plot of IVD Pfirrmann grades vs. the IVD [Na^+] values obtained from the *in vivo* sodium MR images. The solid line represents the linear regression fit of the data pairs, which yielded a moderate but significant correlation coefficient of -0.610 with $p<0.01$.

The three subjects who underwent MT and $T_{1\rho}$ MRI in addition to sodium MRI at the 7 T MRI scanner yielded a total of 14 IVDs for comparing MTR, $T_{1\rho}$, [Na^+] and Pfirrmann grade. The overlaid MTR and $T_{1\rho}$ maps of one subject are shown below in Figure 6-8 along with the corresponding sodium MR image acquired at 7 T.

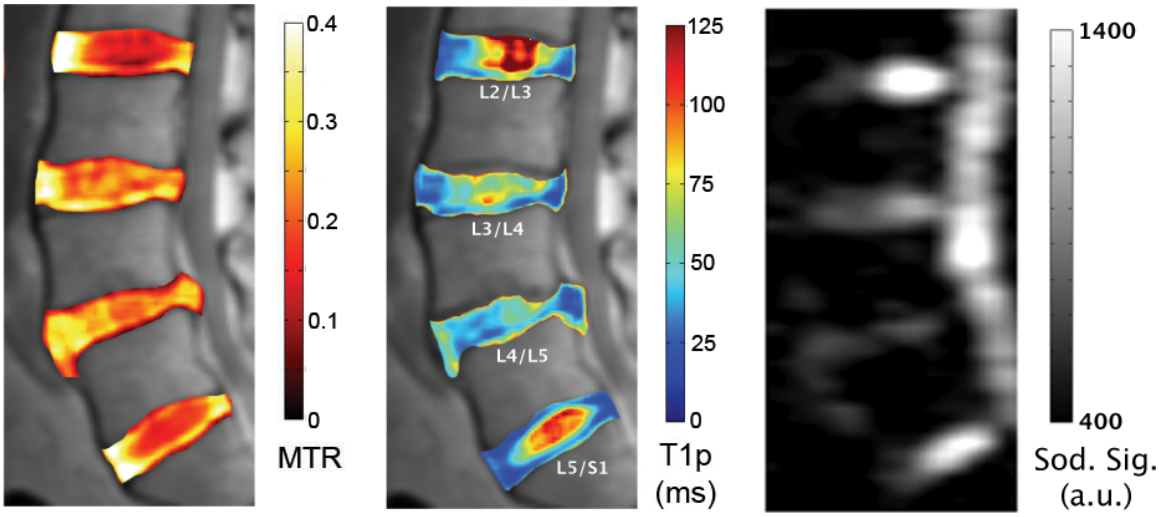

Figure 6-8. The self-coregistered sagittal lumbar MTR and $T_{1\rho}$ maps of a 54-year-old subject overlaid on top of the grayscale anatomical image. The sodium MR image of the same subject is shown on the right.

The lumbar IVDs shown in Figure 6-8 represent a wide range of degenerative grades. The L5/S1 IVD has a Pfirrmann grade of two; the L4/L5 IVD has a grade of four; the L3/L4 IVD has a grade of three; the L2/L3 IVD has a grade of two. The low Pfirrmann grade IVDs (L5/S1 and L2/L3) has low MTR in the NP, along with high $T_{1\rho}$ and high sodium signal. In contrast, the L4/L5 IVD with high Pfirrmann grade, suggesting an advanced degree of degeneration, has high MTR in its NP with low $T_{1\rho}$ and weak sodium signal.

The Pearson correlation coefficients between MTR, $T_{1\rho}$, $[Na^+]$ and Pfirrmann grade are illustrated below in Table 6-1. The Spearman's rank correlation coefficients are shown in Table 6-2.

		[Na+]	T1p	MTR	Pfirrmann
[Na+]	Pearson Correlation	1	.672**	-.533*	-.678**
	Sig. (2-tailed)		.008	.049	.008
	N	14	14	14	14
T1p	Pearson Correlation	.672**	1	-.687**	-.666**
	Sig. (2-tailed)	.008		.007	.009
	N	14	14	14	14
MTR	Pearson Correlation	-.533*	-.687**	1	.774**
	Sig. (2-tailed)	.049	.007		.001
	N	14	14	14	14
Pfirrmann	Pearson Correlation	-.678**	-.666**	.774**	1
	Sig. (2-tailed)	.008	.009	.001	
	N	14	14	14	14

**. Correlation is significant at the 0.01 level (2-tailed).

*. Correlation is significant at the 0.05 level (2-tailed).

Table 6-1. Table of Pearson correlation coefficients between all possible combination pairs of IVD NP MTR, $T_{1\rho}$, $[Na^+]$ and Pfirrmann grades.

			[Na+]	T1p	MTR	Pfirrmann
Spearman's rho	[Na+]	Correlation Coefficient	1.000	.697**	-.701**	-.831**
		Sig. (2-tailed)	.	.006	.005	.000
		N	14	14	14	14
	T1p	Correlation Coefficient	.697**	1.000	-.569*	-.593*
		Sig. (2-tailed)	.006	.	.034	.025
		N	14	14	14	14
	MTR	Correlation Coefficient	-.701**	-.569*	1.000	.746**
		Sig. (2-tailed)	.005	.034	.	.002
		N	14	14	14	14
	Pfirrmann	Correlation Coefficient	-.831**	-.593*	.746**	1.000
		Sig. (2-tailed)	.000	.025	.002	.
		N	14	14	14	14

**. Correlation is significant at the 0.01 level (2-tailed).

*. Correlation is significant at the 0.05 level (2-tailed).

Table 6-2. Table of Spearman's rank correlation coefficients between all possible combination pairs of IVD NP MTR, $T_{1\rho}$, $[Na^+]$ and Pfirrmann grades.

Both the Pearson and the Spearman's rank correlation coefficients indicate the existence of significant linear relationships

between Pfirrmann grade and MTR, $T_{1\rho}$ and [Na^+]. MTR exhibits a positive linear correlation with Pfirrmann grade, while both $T_{1\rho}$ and [Na^+] exhibit a negative linear relationship with Pfirrmann grade. MTR, $T_{1\rho}$ and [Na^+] are also linearly correlated to each other, with the correlation between $T_{1\rho}$ and MTR being the strongest. In each case, the linear correlation is significant with at least $p<0.05$.

6.5 Discussion

The *in vivo* sodium MR images acquired in this study achieved an average SNR of approximately 35 for a total scanning time of less than 30 minutes, which is adequate for *in vivo* [Na^+] quantification purposes. The 5 mm slice thickness resulted in approximately seven sagittal slices covering the spinal column, which allowed us to choose the three middle sagittal slices including both the IVDs and the spinal cord for subsequent ROI analysis. The moderately significant Pearson (-0.610 at $p<0.01$) and Spearman's rank (-0.634 at $p<0.01$) correlation coefficients of the Pfirrmann grade and [Na^+] data pairs suggest that IVD [Na^+] decreases with IVD degeneration. This observation corroborates the earlier finding in Chapter 2, where [Na^+] calculated from sodium MRI was shown to correlate with IVD NP [PG] – a biomolecular indicator of the early stage of IVD degeneration. The lack of a stronger correlation between Pfirrmann grade and

[Na^+] measured using sodium MRI is likely due to the fact that Pfirrmann grade rely on a set of morphological criteria for assigning grade, which is not a continuous variable along the timescale of IVD degeneration. However, the Pfirrmann grade does follow the overall trend of IVD degeneration. The cross-correlation of MTR, $T_{1\rho}$ and [Na^+] with Pfirrmann grade revealed several features of IVD degeneration. IVD NP MTR has been shown to indicate NP relative collagen density in Chapter 4. The increasing MTR with decreasing [Na^+] for higher Pfirrmann grade suggests that the IVD NP collagen density increases with decreasing [Na^+] and [PG]. Therefore, the extracellular matrix of the NP contains greater density of collagen than PG in degenerated IVDs. In addition, the decrease in NP [Na^+] with higher Pfirrmann grade is also correlated with decreasing $T_{1\rho}$, which has been shown to be sensitive to both the *ex vivo* IVD NP [PG](Johannessen et al. 2006), as well as the osmotic pressure (Chapter 3). Thus the decrease in NP [Na^+] in degenerated IVDs occurs along with decreased IVD osmotic pressure. Therefore, considering the changes in MTR, $T_{1\rho}$ and [Na^+] with respect to IVD degeneration, a degenerated IVD should be more fibrotic, contains less PG and has decreased osmotic pressure. The collagen, PG and osmotic pressure characteristics of IVD degeneration have been described previously by various studies in *ex vivo* settings(Haefeli et al. 2006, Johannessen et al. 2006, Urban and McMullin 1988). In contrast, this study represents the first attempt to simultaneously observe and quantify these degenerative

changes *in vivo* using non-invasive MRI techniques. Aging-related IVD degenerative changes are similar to the symptoms of degenerative disc disease (DDD), thus it is difficult to differentiate between IVD degeneration due to aging and IVD degeneration due to pathological processes(Boos et al. 2002). It is not yet clear at the moment whether aging and DDD are unique processes or an identical process occurring over different timescales. A longitudinal study involving a large patient pool with age-matched controls is required to investigate this topic. However, by establishing that *in vivo* MT MRI, $T_{1\rho}$ MRI and sodium MRI can be used to quantify multiple biochemical characteristics of the IVD non-invasively, we open up the possibility to conduct longitudinal studies on human subjects as they undergo IVD degeneration.

6.6 Summary

This study successfully quantified IVD NP [Na^+] *in vivo* on a 7 T MRI scanner, and demonstrated in an *in vivo* setting that the IVD NP [Na^+] decreases with degeneration. The preliminary *in vivo* data on the cross correlation of MTR, $T_{1\rho}$ relaxation time constant and [Na^+] proved the clinical viability of these MRI techniques, which offer future IVD degeneration research the means to quantify a set of IVD tissue biomolecular properties non-invasively in a longitudinal study. Therefore, the combination of

MT MRI, $T_{1\rho}$ MRI and sodium MRI may provide scientists and clinicians with the diagnostic tool to improve our understanding of IVD degeneration, which could benefit future treatment and prognosis of IVD degeneration.

Chapter 7: Dissertation Summary

In this dissertation research project, we investigated three MRI techniques' specificities for IVD biochemical composition. MT MRI, $T_{1\rho}$ MRI and sodium MRI were first separately validated of their specificities for IVD biomolecular components. In doing so, we concluded that MT MRI is sensitive to IVD collagen content, $T_{1\rho}$ MRI is indicative of IVD osmotic pressure, and sodium MRI is sensitive to IVD's PG content.

Following the technique validation experiments, we optimized MT MRI, $T_{1\rho}$ MRI and sodium MRI protocols in order to apply them to human subjects *in vivo*. Due to the inherently low SNR efficiency of sodium MRI, we engineered a custom RF surface coil for sodium MRI of human lumbar spine on a 7 T MRI scanner. Cross-correlation of the MT MRI, $T_{1\rho}$ MRI and sodium MRI data with the corresponding Pfirrmann grade revealed that the relative collagen density of IVDs increases with degeneration, the IVD osmotic pressure decreases with degeneration, and the IVD PG content decreases with degeneration.

By establishing that *in vivo* MT MRI, $T_{1\rho}$ MRI and sodium MRI can be used to quantify multiple IVD biomolecular characteristics non-invasively, we open up the possibility to conduct longitudinal studies on human subjects as they undergo IVD degeneration. Currently the detailed mechanism of IVD degeneration is poorly

understood. In addition, there is significant debate regarding whether IVD degeneration and DDD involve two separate degeneration mechanisms or a single degeneration mechanism occurring over different timescales. The combination of MT MRI, $T_{1\rho}$ MRI and sodium MRI provides scientists and clinicians with the diagnostic tool to improve our understanding of IVD degeneration, which would ultimately benefit future treatment and prognosis of IVD degeneration.

BIBLIOGRAPHY

Akella, S. V., R. R. Regatte, A. J. Gougoutas, A. Borthakur, E. M. Shapiro, J. B. Kneeland, J. S. Leigh & R. Reddy (2001) Proteoglycan-induced changes in T1rho-relaxation of articular cartilage at 4T. *Magn Reson Med,* 46, 419-23.

Anderson, M. W. (2004) Lumbar discography: an update. *Semin Roentgenol,* 39, 52-67.

Antoniou, J., T. Steffen, F. Nelson, N. Winterbottom, A. P. Hollander, R. A. Poole, M. Aebi & M. Alini (1996) The human lumbar intervertebral disc: evidence for changes in the biosynthesis and denaturation of the extracellular matrix with growth, maturation, ageing, and degeneration. *J Clin Invest,* 98, 996-1003.

Auerbach, J. D., W. Johannessen, A. Borthakur, A. J. Wheaton, C. A. Dolinskas, R. A. Balderston, R. Reddy & D. M. Elliott (2006) In vivo quantification of human lumbar disc degeneration using T(1rho)-weighted magnetic resonance imaging. *Eur Spine J,* 15 Suppl 15, 338-44.

Beadle, O. A. 1931. *The intervertebral discs; observations on their normal and morbid anatomy in relation to certain spinal deformities*. London,: H. M. Stationery off.

Berendsen, H. J. & H. T. Edzes (1973) The observation and general interpretation of sodium magnetic resonance in biological material. *Ann N Y Acad Sci,* 204, 459-85.

Bianco, P., L. W. Fisher, M. F. Young, J. D. Termine & P. G. Robey (1990) Expression and localization of the two small proteoglycans biglycan and decorin in developing human skeletal and non-skeletal tissues. *J Histochem Cytochem,* 38, 1549-63.

Boos, N., D. Dreier, E. Hilfiker, V. Schade, R. Kreis, J. Hora, M. Aebi & C. Boesch (1997) Tissue characterization of symptomatic and asymptomatic disc herniations by quantitative magnetic resonance imaging. *J Orthop Res,* 15, 141-9.

Boos, N., S. Weissbach, H. Rohrbach, C. Weiler, K. F. Spratt & A. G. Nerlich (2002) Classification of age-related changes in lumbar intervertebral discs: 2002 Volvo Award in basic science. *Spine (Phila Pa 1976),* 27, 2631-44.

Borthakur, A., I. Hancu, F. E. Boada, G. X. Shen, E. M. Shapiro & R. Reddy (1999) In vivo triple quantum filtered twisted projection sodium MRI of human articular cartilage. *J Magn Reson,* 141, 286-90.

Borthakur, A., E. Mellon, S. Niyogi, W. Witschey, J. B. Kneeland & R. Reddy (2006) Sodium and T1rho MRI for molecular and diagnostic imaging of articular cartilage. *NMR Biomed,* 19, 781-821.

Borthakur, A., E. M. Shapiro, S. V. Akella, A. Gougoutas, J. B. Kneeland & R. Reddy (2002) Quantifying sodium in the human wrist in vivo by using MR imaging. *Radiology,* 224, 598-602.

Borthakur, A., E. M. Shapiro, J. Beers, S. Kudchodkar, J. B. Kneeland & R. Reddy (2000) Sensitivity of MRI to proteoglycan depletion in cartilage: comparison of sodium and proton MRI. *Osteoarthritis & Cartilage,* 8, 288-293.

Borthakur, A., A. J. Wheaton, A. J. Gougoutas, S. V. Akella, R. R. Regatte, S. R. Charagundla & R. Reddy (2004) In vivo measurement of T1rho dispersion in the human brain at 1.5 tesla. *J Magn Reson Imaging,* 19, 403-9.

Bottomley, P. A., C. J. Hardy, R. E. Argersinger & G. Allen-Moore (1987) A review of 1H nuclear magnetic resonance relaxation in pathology: are T1 and T2 diagnostic? *Med Phys,* 14, 1-37.

Burstein, D. & E. T. Fossel (1987) Intracellular sodium and lithium NMR relaxation times in the perfused frog heart. *Magn Reson Med,* 4, 261-73.

Carey, T. S., A. Evans, N. Hadler, W. Kalsbeek, C. McLaughlin & J. Fryer (1995) Care-seeking among individuals with chronic low back pain. *Spine (Phila Pa 1976),* 20, 312-7.

Cassar-Pullicino, V. N. (1998) MRI of the ageing and herniating intervertebral disc. *Eur J Radiol,* 27, 214-28.

Ceckler, T. L., K. Karino, P. F. Kador & R. S. Balaban (1991) Magnetic-Resonance-Imaging of the Rabbit Eye - Improved Anatomical Detail Using Magnetization Transfer Contrast. *Investigative Ophthalmology & Visual Science,* 32, 3109-3113.

Ceckler, T. L., S. D. Wolff, V. Yip, S. A. simon & R. S. Balaban (1992) Dynamic and Chemical Factors Affecting Water Proton Relaxation by Macromolecules. *Journal of Magnetic Resonance,* 98, 637-45.

Charagundla, S. R., A. Borthakur, J. S. Leigh & R. Reddy (2003) Artifacts in T-1 rho-weighted imaging: correction with a self-compensating spin-locking pulse. *Journal of Magnetic Resonance,* 162, 113-121.

Charagundla, S. R., A. H. Stolpen, J. S. Leigh & R. Reddy (1998) Off-resonance proton $T_{1\rho}$ dispersion imaging of ^{17}O-enriched tissue phantoms. *Magn Reson Med,* 39, 588-95.

Clayson, S. J., I. M. Newman, D. F. Debevec, R. W. Anger, H. V. Skowlund & F. Kottke (1962) Evaluation of mobility of hip and lumbar vertebrae of normal young women. *Arch Phys Med Rehabil,* 43, 1-8.

Comper, W. D. 1996a. *Extracellular Matrix: Molecular Components and Interactions*. Amsterdam, Netherland: Harwood Academic Publishers.

---. 1996b. *Extracellular Matrix: Tissue Function*. Amsterdam, Netherland: Harwood Academic Publishers.

Cope, F. W. (1970) Spin-echo nuclear magnetic resonance evidence for complexing of sodium ions in muscle, brain, and kidney. *Biophys J,* 10, 843-58.

Coventry, M. B., Ghormley, R.K. and Kernohan, J.W. (1945) The intervertebral disc: Its microscopic anatomy and pathology; anatomy, development and physiology. *J Bone Jt Surg,* 27, 105-112.

Cowper, S. E., H. S. Robin, S. M. Steinberg, L. D. Su, S. Gupta & P. E. LeBoit (2000) Scleromyxoedema-like cutaneous diseases in renal-dialysis patients. *Lancet,* 356, 1000-1.

Davidson, E. A. & B. Woodhall (1959) Biochemical alterations in herniated intervertebral disks. *J Biol Chem,* 234, 2951-4.

De Palma, A. F. & R. H. Rothman. 1970. *The intervertebral disc*. Philadelphia,: W. R. Saunders Co.

Dixon, W. T., J. N. Oshinski, J. D. Trudeau, B. C. Arnold & R. I. Pettigrew (1996) Myocardial suppression *in vivo* by spin locking with composite pulses. *Magn Reson Med,* 36, 90-4.

Duvvuri, U., S. R. Charagundla, S. B. Kudchodkar, J. H. Kaufman, J. B. Kneeland, R. Rizi, J. S. Leigh & R. Reddy (2001) Human knee: in vivo T1(rho)-weighted MR imaging at 1.5 T--preliminary experience. *Radiology,* 220, 822-6.

Edzes, H. T. & E. T. Samulski (1977) Cross relaxation and spin diffusion in the proton NMR or hydrated collagen. *Nature,* 265, 521-3.

Eng, J., T. L. Ceckler & R. S. Balaban (1991) QUANTITATIVE H-1 MAGNETIZATION TRANSFER IMAGING INVIVO. *Magnetic Resonance in Medicine,* 17, 304-314.

Errico, T. J. (2005) Lumbar disc arthroplasty. *Clin Orthop Relat Res*, 106-17.

Eyre, D. R., Y. Matsui & J. J. Wu (2002a) Collagen polymorphisms of the intervertebral disc. *Biochem Soc Trans,* 30, 844-8.

Eyre, D. R. & H. Muir (1976) Types I and II collagens in intervertebral disc. Interchanging radial distributions in annulus fibrosus. *Biochem J,* 157, 267-70.

--- (1977) Quantitative analysis of types I and II collagens in human intervertebral discs at various ages. *Biochim Biophys Acta,* 492, 29-42.

Eyre, D. R., J. J. Wu, R. J. Fernandes, T. A. Pietka & M. A. Weis (2002b) Recent developments in cartilage research: matrix biology of the collagen II/IX/XI heterofibril network. *Biochem Soc Trans,* 30, 893-9.

Ferlic, D. (1962) The range of motion of the "normal" cervical spine. *Bull Johns Hopkins Hosp,* 110, 59-65.

Fishbein, K. W., Y. A. Gluzband, M. Kaku, H. Ambia-Sobhan, S. A. Shapses, M. Yamauchi & R. G. Spencer (2007) Effects of formalin fixation and collagen cross-linking on T2 and magnetization transfer in bovine nasal cartilage. *Magn Reson Med,* 57, 1000-11.

Freburger, J. K., G. M. Holmes, R. P. Agans, A. M. Jackman, J. D. Darter, A. S. Wallace, L. D. Castel, W. D. Kalsbeek & T. S. Carey (2009) The rising prevalence of chronic low back pain. *Arch Intern Med,* 169, 251-8.

Ghosh, P. 1988. *The Biology of the intervertebral disc*. Boca Raton, FL: CRC Press.

Granot, J. (1988) Sodium imaging of human body organs and extremities in vivo. *Radiology,* 167, 547-50.

Grohn, O. H. J., M. I. Kettunen, H. I. Makela, M. Penttonen, A. Pitkanen, J. A. Lukkarinen & R. A. Kauppinen (2000) Early detection of irreversible cerebral ischemia in the rat using dispersion of the magnetic resonance imaging relaxation time, T1rho. *J Cereb Blood Flow Metab,* 20, 1457-66.

Gruber, H. E., J. A. Ingram & E. N. Hanley, Jr. (2002) Tenascin in the human intervertebral disc: alterations with aging and disc degeneration. *Biotech Histochem,* 77, 37-41.

Grynpas, M. D., D. R. Eyre & D. A. Kirschner (1980) Collagen type II differs from type I in native molecular packing. *Biochim Biophys Acta,* 626, 346-55.

Gunzburg, R., M. Szpalski & G. Andersson. 2004. *Degenerative disc disease*. Philadelphia: Lippincott Williams & Wilkins.

Haacke, E. M. 1999. *Magnetic resonance imaging : physical principles and sequence design*. New York: Wiley.

Haefeli, M., F. Kalberer, D. Saegesser, A. G. Nerlich, N. Boos & G. Paesold (2006) The course of macroscopic degeneration in the human lumbar intervertebral disc. *Spine,* 31, 1522-1531.

Harel, A., U. Eliav, S. Akselrod & G. Navon (2008) Magnetization transfer based contrast for imaging denatured collagen. *J Magn Reson Imaging,* 27, 1155-63.

Henkelman, R. M., G. J. Stanisz & S. J. Graham (2001) Magnetization transfer in MRI: a review. *Nmr in Biomedicine,* 14, 57-64.

Hillenbrand, H. B., L. C. Becker, R. Kharrazian, K. Hu, C. E. Rochitte, R. J. Kim, E. L. Chen, G. Ertl, R. H. Hruban & J. A. Lima (2005) 23Na MRI combined with contrast-enhanced 1H MRI provides in vivo characterization of infarct healing. *Magn Reson Med,* 53, 843-50.

Hollander, A. P., T. F. Heathfield, J. J. Liu, I. Pidoux, P. J. Roughley, J. S. Mort & A. R. Poole (1996) Enhanced denaturation of the alpha (II) chains of type-II collagen in normal adult human intervertebral discs compared with femoral articular cartilage. *J Orthop Res,* 14, 61-6.

Hubbard, P. (1970) Nonexponential Nuclear Magnetic Relaxation by Quadrupole Interactions. *J CHEM PHYS,* 53, 985-987.

Inkinen, R. I., M. J. Lammi, S. Lehmonen, K. Puustjarvi, E. Kaapa & M. I. Tammi (1998) Relative increase of biglycan and decorin and altered chondroitin sulfate epitopes in the degenerating human intervertebral disc. *J Rheumatol,* 25, 506-14.

Inoue, H. (1981) Three-dimensional architecture of lumbar intervertebral discs. *Spine,* 6, 139-46.

Insko, E. K., D. B. Clayton & M. A. Elliott (2002) In vivo sodium MR imaging of the intervertebral disk at 4 T. *Acad Radiol,* 9, 800-4.

Janus, N., V. Launay-Vacher, S. Karie, O. Clement, E. Ledneva, C. Frances, G. Choukroun & G. Deray Prevalence of nephrogenic systemic fibrosis in renal insufficiency patients: results of the FINEST study. *Eur J Radiol,* 73, 357-9.

Jayson, M. I. V. 1976. *The Lumbar spine and back pain*. London: Sector Publishing Ltd. for Pitman Medical.

Johannessen, W., J. D. Auerbach, A. J. Wheaton, A. Kurji, A. Borthakur, R. Reddy & D. M. Elliott (2006) Assessment of human disc degeneration and proteoglycan content using T1rho-weighted magnetic resonance imaging. *Spine (Phila Pa 1976),* 31, 1253-7.

Johnstone, B., M. Markopoulos, P. Neame & B. Caterson (1993) Identification and characterization of glycanated and non-glycanated forms of biglycan and decorin in the human intervertebral disc. *Biochem J,* 292 (Pt 3), 661-6.

Katz, J. N. (2006) Lumbar disc disorders and low-back pain: socioeconomic factors and consequences. *J Bone Joint Surg Am,* 88 Suppl 2, 21-4.

Kelsey, J. L., P. B. Githens, A. A. White, 3rd, T. R. Holford, S. D. Walter, T. O'Connor, A. M. Ostfeld, U. Weil, W. O. Southwick & J. A. Calogero (1984) An epidemiologic study of lifting and twisting on the job and risk for acute prolapsed lumbar intervertebral disc. *J Orthop Res,* 2, 61-6.

Khanna, A. J., J. J. Carbone, K. M. Kebaish, D. B. Cohen, L. H. Riley, 3rd, B. A. Wasserman & J. P. Kostuik (2002) Magnetic resonance imaging of the cervical spine. Current techniques and spectrum of disease. *J Bone Joint Surg Am,* 84-A Suppl 2, 70-80.

Kim, D. K., T. L. Ceckler, V. C. Hascall, A. Calabro & R. S. Balaban (1993) Analysis of water-macromolecule proton magnetization transfer in articular cartilage. *Magn Reson Med,* 29, 211-5.

Korecki, C. L., J. J. Costi & J. C. Iatridis (2008) Needle puncture injury affects intervertebral disc mechanics and biology in an organ culture model. *Spine (Phila Pa 1976),* 33, 235-41.

Lamminen, A. E., J. I. Tanttu, R. E. Sepponen, H. Pihko & O. A. Korhola (1993) T1rho dispersion imaging of diseased muscle tissue. *British Journal of Radiology,* 66, 783-7.

Laurent, D., J. Wasvary, J. Yin, M. Rudin, T. C. Pellas & E. O'Byrne (2001) Quantitative and qualitative assessment of articular cartilage in the goat knee with magnetization transfer imaging. *Magn Reson Imaging,* 19, 1279-86.

Lesperance, L. M., M. L. Gray & D. Burstein (1992) Determination of fixed charge density in cartilage using nuclear magnetic resonance. *J Orthop Res,* 10, 1-13.

Levitt, M. H. 2008. *Spin dynamics : basics of nuclear magnetic resonance*. Chichester, England ; Hoboken, NJ: John Wiley & Sons.

Li, X., C. Benjamin Ma, T. M. Link, D. D. Castillo, G. Blumenkrantz, J. Lozano, J. Carballido-Gamio, M. Ries & S. Majumdar (2007) In vivo T(1rho) and T(2) mapping of articular cartilage in osteoarthritis of the knee using 3 T MRI. *Osteoarthritis Cartilage,* 15, 789-97.

Mallen, A. (1962) The collagen and ground substance of human intervertebral discs at different ages. *Acta Chem. Scand.,* 16, 705.

Marchand, F. & A. M. Ahmed (1990) Investigation of the laminate structure of lumbar disc anulus fibrosus. *Spine,* 15, 402-10.

Markkola, A. T., H. J. Aronen, T. Paavonen, E. Hopsu, L. M. Sipila, J. I. Tanttu & R. E. Sepponen (1997) T1rho dispersion imaging of head and neck tumors: a comparison to spin lock and magnetization transfer techniques. *J Magn Reson Imaging,* 7, 873-9.

Maroudas, A. 1990. *Methods in cartilage research*. London: Academic Press.

Maroudas, A., R. A. Stockwell, A. Nachemson & J. Urban (1975) Factors involved in the nutrition of the human lumbar intervertebral disc: cellularity and diffusion of glucose in vitro. *J Anat,* 120, 113-30.

Mathur-De Vre, R. (1984) Biomedical implications of the relaxation behaviour of water related to NMR imaging. *Br J Radiol,* 57, 955-76.

Melhem, E. R., M. L. Benson, N. J. Beauchamp & R. R. Lee (1996) Cervical spondylosis: three-dimensional gradient-echo MR with magnetization transfer. *AJNR Am J Neuroradiol,* 17, 705-11.

Melhem, E. R., R. J. Bert & S. G. Faddoul (2000) Cervical spondylosis: contrast-enhanced magnetization transfer prepulsed 3D turbo field echo MR imaging. *J Magn Reson Imaging,* 11, 294-8.

Melhem, E. R., S. D. Caruthers & H. Jara (1998) Cervical spine: Three-dimensional MR imaging with magnetization transfer prepulsed turbo field echo techniques. *Radiology,* 207, 815-821.

Menezes, N. M., M. L. Gray, J. R. Hartke & D. Burstein (2004) T2 and T1rho MRI in articular cartilage systems. *Magn Reson Med,* 51, 503-9.

Mikawa, Y., H. Hamagami, J. Shikata & T. Yamamuro (1986) Elastin in the human intervertebral disk. A histological and biochemical study comparing it with elastin in the human yellow ligament. *Arch Orthop Trauma Surg,* 105, 343-9.

Mlynarik, V., S. Trattnig, M. Huber, A. Zembsch & H. Imhof (1999) The role of relaxation times in monitoring proteoglycan depletion in articular cartilage. *J Magn Reson Imaging,* 10, 497-502.

Morgan, S. & A. Saifuddin (1999) MRI of the lumbar intervertebral disc. *Clin Radiol,* 54, 703-23.

Murayama, K. (1972) [Biochemical studies on the age-related variations of the human intervertebral disc]. *Nippon Seikeigeka Gakkai Zasshi,* 46, 81-104.

Nachemson, A. & G. Elfström. 1970. *Intravital dynamic pressure measurements in lumbar discs. A study of common movements, maneuvers and exercises*. Stockholm,: Almqvist & Wiksell.

Naylor, A. (1962) The biophysical and biochemical aspects of intervertebral disc herniation and degeneration. *Ann R Coll Surg Engl,* 31, 91-114.

Nielles-Vallespin, S., M. A. Weber, M. Bock, A. Bongers, P. Speier, S. E. Combs, J. Wohrle, F. Lehmann-Horn, M. Essig & L. R. Schad (2007) 3D radial projection technique with ultrashort echo times for sodium MRI: clinical applications in human brain and skeletal muscle. *Magn Reson Med,* 57, 74-81.

Niinimaki, J. L., O. Parviainen, J. Ruohonen, R. Ojala, M. Kurunlahti, J. Karppinen, O. Tervonen & M. T. Nieminen (2006) In vivo quantification of delayed gadolinium enhancement in the nucleus pulposus of human intervertebral disc. *Journal of Magnetic Resonance Imaging,* 24, 796-800.

Noggle, J. H. & R. E. Schirmer. 1971. *The nuclear Overhauser effect; chemical applications*. New York,: Academic Press.

Oegema, T. R., Jr., S. L. Johnson, D. J. Aguiar & J. W. Ogilvie (2000) Fibronectin and its fragments increase with degeneration in the human intervertebral disc. *Spine (Phila Pa 1976),* 25, 2742-7.

Paajanen, H., M. Komu, I. Lehto, M. Laato & H. Haapasalo (1994) MAGNETIZATION-TRANSFER IMAGING OF LUMBAR DISC DEGENERATION - CORRELATION OF RELAXATION PARAMETERS WITH BIOCHEMISTRY. *Spine,* 19, 2833-2837.

Pekar, J. & J. S. Leigh (1986) DETECTION OF BIEXPONENTIAL RELAXATION IN NA-23 FACILITATED BY DOUBLE-QUANTUM FILTERING. *Journal of Magnetic Resonance,* 69, 582-584.

Perman, W. H., P. A. Turski, L. W. Houston, G. H. Glover & C. E. Hayes (1986) Methodology of in vivo human sodium MR imaging at 1.5 T. *Radiology,* 160, 811-20.

Pfirrmann, C. W., A. Metzdorf, M. Zanetti, J. Hodler & N. Boos (2001) Magnetic resonance classification of lumbar intervertebral disc degeneration. *Spine,* 26, 1873-8.

Pilet, B., R. Salgado, T. Van Havenbergh & P. M. Parizel (2009) Development of acute schmorl nodes after discography. *J Comput Assist Tomogr,* 33, 597-600.

Poptani, H., U. Duvvuri, C. G. Miller, A. Mancuso, S. Charagundla, N. W. Fraser, J. D. Glickson, J. S. Leigh & R. Reddy (2001) T1rho imaging of murine brain tumors at 4 T. *Acad Radiol,* 8, 42-7.

Ra, J. B., S. K. Hilal, C. H. Oh & I. K. Mun (1988) In vivo magnetic resonance imaging of sodium in the human body. *Magn Reson Med,* 7, 11-22.

Raj, P. P. (2008) Intervertebral disc: anatomy-physiology-pathophysiology-treatment. *Pain Pract,* 8, 18-44.

Regatte, R. R., S. V. Akella, A. Borthakur, J. B. Kneeland & R. Reddy (2002) Proteoglycan depletion-induced changes in transverse relaxation maps of cartilage: comparison of T2 and T1rho. *Acad Radiol,* 9, 1388-94.

Roberts, S., M. A. Bains, A. Kwan, J. Menage & S. M. Eisenstein (1998) Type X collagen in the human invertebral disc: an indication of repair or remodelling? *Histochem J,* 30, 89-95.

Roberts, S., J. Menage, V. Duance, S. Wotton & S. Ayad (1991) 1991 Volvo Award in basic sciences. Collagen types around the cells of the intervertebral disc and cartilage end plate: an immunolocalization study. *Spine (Phila Pa 1976),* 16, 1030-8.

Roberts, S., J. Menage & J. P. Urban (1989) Biochemical and structural properties of the cartilage end-plate and its relation to the intervertebral disc. *Spine,* 14, 166-74.

Rubin, D. I. (2007) Epidemiology and risk factors for spine pain. *Neurologic Clinics,* 25, 353-+.

Saifuddin, A., R. Mitchell & B. A. Taylor (1999) Extradural inflammation associated with annular tears: demonstration with gadolinium-enhanced lumbar spine MRI. *Eur Spine J,* 8, 34-9.

Santyr, G. E., R. M. Henkelman & M. J. Bronskill (1989) Spin locking for magnetic resonance imaging with application to human breast. *Magn Reson Med,* 12, 25-37.

Schlesinger, P. T. (1955) Incarceration of the first sacral nerve in a lateral bony recess of the spinal canal as a cause of sciatica. *J Bone Joint Surg Am,* 37-A, 115-24.

Scott, J. E., T. R. Bosworth, A. M. Cribb & J. R. Taylor (1994) The chemical morphology of age-related changes in human intervertebral disc glycosaminoglycans from cervical, thoracic and lumbar nucleus pulposus and annulus fibrosus. *J Anat,* 184 (Pt 1), 73-82.

Shapiro, E. M., A. Borthakur, R. Dandora, A. Kriss, J. S. Leigh & R. Reddy (2000) Sodium visibility and quantitation in intact bovine articular cartilage using high field (23)Na MRI and MRS. *J Magn Reson,* 142, 24-31.

Shapiro, E. M., A. Borthakur, A. Gougoutas & R. Reddy (2002) 23Na MRI accurately measures fixed charge density in articular cartilage. *Magn Reson Med,* 47, 284-91.

Shporer, M. & M. M. Civan (1974) Effects of temperature and field strength on the NMR relaxation times of 23 Na in frog striated muscle. *Biochim Biophys Acta,* 354, 291-304.

Sivan, S., Y. Merkher, E. Wachtel, S. Ehrlich & A. Maroudas (2006) Correlation of swelling pressure and intrafibrillar water in young and aged human intervertebral discs. *J Orthop Res,* 24, 1292-8.

Stobbe, R. & C. Beaulieu (2005) In vivo sodium magnetic resonance imaging of the human brain using soft inversion recovery fluid attenuation. *Magn Reson Med,* 54, 1305-10.

Sztrolovics, R., J. Grover, G. Cs-Szabo, S. L. Shi, Y. Zhang, J. S. Mort & P. J. Roughley (2002) The characterization of versican and its message in human articular cartilage and intervertebral disc. *J Orthop Res,* 20, 257-66.

Thompson, J. P., R. H. Pearce, M. T. Schechter, M. E. Adams, I. K. Tsang & P. B. Bishop (1990) Preliminary evaluation of a scheme for grading the gross morphology of the human intervertebral disc. *Spine (Phila Pa 1976),* 15, 411-5.

Torchia, D. A., M. A. Hasson & V. C. Hascall (1977) Investigation of molecular motion of proteoglycans in cartilage by 13C magnetic resonance. *J Biol Chem,* 252, 3617-25.

Urban, J. P., A. Maroudas, M. T. Bayliss & J. Dillon (1979) Swelling pressures of proteoglycans at the concentrations found in cartilaginous tissues. *Biorheology,* 16, 447-64.

Urban, J. P. & J. F. McMullin (1988) Swelling pressure of the lumbar intervertebral discs: influence of age, spinal level, composition, and degeneration. *Spine,* 13, 179-87.

Urban, J. P. & S. Roberts (2003) Degeneration of the intervertebral disc. *Arthritis Res Ther,* 5, 120-30.

Urban, J. P. & C. P. Winlove (2007) Pathophysiology of the intervertebral disc and the challenges for MRI. *J Magn Reson Imaging,* 25, 419-32.

Vaga, S., M. T. Raimondi, E. G. Caiani, F. Costa, C. Giordano, F. Perona, A. Zerbi & M. Fornari (2008) Quantitative assessment of intervertebral disc glycosaminoglycan distribution by gadolinium-enhanced MRI in orthopedic patients. *Magn Reson Med,* 59, 85-95.

van Tulder, M., B. Koes & C. Bombardier (2002) Low back pain. *Best Pract Res Clin Rheumatol,* 16, 761-75.

W, I. J. & A. Burdorf (2004) Patterns of care for low back pain in a working population. *Spine (Phila Pa 1976),* 29, 1362-8.

Wang, C., J. D. Auerbach, W. R. Witschey, R. A. Balderston, R. Reddy & A. Borthakur (2007) Advances in Magnetic Resonance Imaging for the assessment of degenerative disc disease of the lumbar spine. *Semin Spine Surg,* 19, 65-71.

Wang, C., E. McArdle, M. Fenty, W. Witschey, M. Elliott, M. Sochor, R. Reddy & A. Borthakur (2010) Validation of sodium magnetic resonance imaging of intervertebral disc. *Spine (Phila Pa 1976),* 35, 505-10.

Watanabe, A., L. M. Benneker, C. Boesch, T. Watanabe, T. Obata & S. E. Anderson (2007) Classification of intervertebral disk degeneration with axial T2 mapping. *AJR Am J Roentgenol,* 189, 936-42.

Wehrli, F. W., D. Shaw & J. B. Kneeland. 1988. *Biomedical magnetic resonance imaging : principles, methodology, and applications*. New York, N.Y.: VCH.

Wheaton, A. J., A. Borthakur, G. R. Dodge, J. B. Kneeland, H. R. Schumacher & R. Reddy (2004) Sodium magnetic resonance imaging of proteoglycan depletion in an in vivo model of osteoarthritis. *Acad Radiol,* 11, 21-8.

Wheaton, A. J., G. R. Dodge, D. M. Elliott, S. B. Nicoll & R. Reddy (2005) Quantification of cartilage biomechanical and biochemical properties via T1rho magnetic resonance imaging. *Magn Reson Med,* 54, 1087-93.

Wolff, S. D. & R. S. Balaban (1989) Magnetization transfer contrast (MTC) and tissue water proton relaxation in vivo. *Magn Reson Med,* 10, 135-44.

Wotton, S. F., V. C. Duance & P. R. Fryer (1988) Type IX collagen: a possible function in articular cartilage. *FEBS Lett,* 234, 79-82.

Yoshioka, H., H. Nishimura, T. Masuda, K. Nakajima, H. Onaya & Y. Itai (1994) Magnetization transfer contrast imaging of the cervical spine at 0.3 T. *J Comput Assist Tomogr,* 18, 947-53.

Yoshioka, H., H. Onaya, Y. Itai, H. Nishimura, A. Matsumura, T. Tsunoda, S. Kandatsu, M. Koga, K. Yoshikawa, H. Kato & H. Tsujii (1997) Comparison between magnetization transfer contrast and fast spin-echo MR imaging of degenerative disease of the cervical spine at 0.3 T. *Magnetic Resonance Imaging,* 15, 37-45.

Yu, J., P. C. Winlove, S. Roberts & J. P. Urban (2002) Elastic fibre organization in the intervertebral discs of the bovine tail. *J Anat,* 201, 465-75.